FINGERPADS WITH ADAPTIVE SURFACE PROPERTIES FOR ROBOTIC GRIPPING

by

Katherine Allison

A thesis submitted in conformity with the requirements
for the degree of Master of Applied Science

Department of Mechanical and Industrial Engineering
University of Toronto

Fingerpads with Adaptive Surface Properties for Robotic Gripping

Katherine Allison
Master of Applied Science

Department of Mechanical and Industrial Engineering
University of Toronto
2024

Abstract

Recent advances in materials science have created surfaces with controllable adhesion, friction, and compliance. These "adaptive surfaces" enable a versatile control paradigm in robotic gripping, where control over contact properties improves performance across widely varying target surfaces. Using actively adaptive grip surfaces, friction can be increased to grip securely and then decreased to gently release or manipulate in-hand. Existing adaptive surface designs show good friction control; however, most require specialized fabrication processes and are impractical for gripping. This thesis presents a practical and inexpensive multi-level adaptive fingerpad design that is easily adapted to existing grippers. Actuating the fingerpad deflects its contact surface in structured active regions, tuning friction by combining microscale effects from microtopography with mesoscale effects from surface morphology changes and macroscale effects from grip articulation. The fingerpad's friction-tuning capabilities are characterized through shear force testing and additional features are demonstrated including macroscale interlocking behaviour and pressure-based object detection.

Acknowledgements

First and foremost, I would like to thank my supervisors Prof. Benjamin Hatton and Prof. Jonathan Kelly for the opportunity to work on such an interesting and interdisciplinary project. I have greatly enjoyed being able to expand my knowledge and skillset over the course of my Master's degree, and I am grateful to have had input, feedback, and perspective from experts in two very different fields.

I had the privilege of being supported by many talented, generous, and compassionate people during my thesis work. The staff of the Myhal Centre Fabrication Facility have been endlessly patient and have helped me to figure out design and fabrication problems at every step of the way—without the support of Max, Lihin, Lorena, Tanziba, Colin, Willy, Mason, and Christian, none of the prototypes shown in these thesis could have been made. I am deeply grateful to Prof. Philip Asare for both giving me the incredible opportunity to be the Prototyping Lead for ESC204 and helping me to get through the difficult first half of my project. In the latter half of my degree, Philip and Prof. Morgan Hooper have both helped me to develop the mechatronics skills necessary to build my test equipment and offered invaluable advice on design, communication, and the graduate school experience in general. Prof. Mark Kortschot has been an excellent mentor to me and has given me useful advice on research productivity, technical communication, and a variety of other topics that will continue to serve me well in the future. I am also thankful for timely advice from Prof. Markus Bussman in the last stages of my thesis and for the support of Prof. Arthur Chan in carrying more than his share of our course workload so that I could finish my degree.

The members of the Bio-Inspired Materials and Design Lab and the STARS Lab have made my research work more rewarding and the last several years significantly more fun. I am grateful for the laughs, moral support, and positivity that my labmates and my fellow students in the Robotics Institute have given me throughout my degree. The members of the STARS LAB "Manipulation Assembly" meetings have helped me greatly in identifying the most impactful parts of my work. I am particularly indebted to Philippe Nadeau, who through painstaking review helped me to write a significantly more readable, impactful, and persuasive paper. Most of all, I am grateful to Mia Thomas for her insight, humour, commiseration, and friendship.

My friends and family have been a lifeline for me over the past few years, and I cannot thank them enough. I am grateful to Hanna Zhang, Chinmayee Gidwani, and Celina Yang for their endless support and frequent feedback, to Kevin Xu for taking my mind off of research, and to too many others to count for bringing joy in difficult times. I am also grateful for the support of my family, who have celebrated all of my milestones with me and helped me through all of my tribulations, and who have taken the time to give me feedback and support at every step. I am thankful for the family dogs, Mollie and Daisy, who tried unsuccessfully to eat various of my prototypes and made up for it by acting as patient rubber ducks. Above all, I am grateful to Devin Gibson, who has supported me without fail, read every word of this thesis, and listened to me talk about bioadhesion and robotic grippers daily for years.

Contents

List of Tables

List of Figures

Chapter 1

Introduction

Human gripping is remarkably effective, versatile, and adaptable. Our hands can securely grasp objects with diverse shapes, sizes, and stiffnesses—ranging from a fragile egg to a soft pillow to a rigid hammer. This exceptional generalized grasping capability is facilitated by an intricate biomechanical structure involving multiple fingers that each have several degrees of freedom, microstructured ridges that form friction-enhancing fingerprints, an adjustable palm configuration, extensive sensory networks, and soft tissue that allows some limited compliance to gripped objects [1]–[3]. When objects must be manipulated in-hand, human grasping uses a complex feedback loop to sense friction against the skin and adapt grip forces and contact positions accordingly. Using this fine-tuned friction control, the human hand can adaptively adjust its grasp to a degree that robotics has yet to emulate.

As with human grasping, successful robotic manipulation relies on control over friction at the grip interface. Despite a great deal of investment in the field, artificial gripping techniques cannot match the versatility, grace, and dexterity of human hands. While the use of underactuated or compliant gripping approaches can help to improve grip security and increase the range of viable target objects, gripper performance is still lacking, particularly in terms of dynamic adaptability.

The gap between biological and robotic gripping performance is especially stark when grasping soft or fragile objects, a problem that has motivated the development of soft grippers. For most rigid grippers, stable grasps rely on force closure, in which contacts must be formed with sufficiently high friction forces to resist object wrenches [4]. While friction can be increased using normal grip forces (i.e., squeezing harder), high normal forces exerted by stiff surfaces may damage delicate objects [1], [5]. In contrast, human hands can safely handle delicate objects due to their excellent force control and moderate compliance. Despite their comparatively crude force control, soft grippers can grasp gently due to their high compliance, which both distributes grip pressure and increases friction by increasing contact area [5]–[8].

The challenge of securely grasping with reduced normal force has motivated interdisciplinary work combining design principles from materials science and robotics. Gripping surfaces can easily be modified at design time to increase their effective coefficient of friction (e.g., by adding surface texture [3], [9]). However, increased friction is not always desirable—for example, high friction reduces the dexterity of soft grippers by inhibiting sliding [10]–[12]. Instead, gripping dexterously demands a degree of control over both friction enhancement and friction reduction. For versatile

manipulation, the ability to actively tune friction is an attractive possibility. Grip surfaces with active friction tuning could use a higher-friction state to maintain a stable grasp and a lower-friction state when delicately placing an object or performing in-hand manipulation tasks. Friction tuning has the potential to enable manipulation that is both controlled and precise, allowing for efficient handling and delicate adjustment.

Recent research has turned to other areas of nature to draw inspiration, leading to a variety of adaptive surfaces that mimic the natural ability of certain animals to tune their contact conditions for improved locomotion and manipulation. For instance, adaptive friction surfaces often mimic the ability of snakes to tilt their scales, and adaptive adhesive surfaces often mimic the ability of geckos to stick to surfaces repeatably and adaptively [13]–[15]. In materials science, the structural adaptations found in biology have been studied and mimicked using bio-inspired patterned materials with specialized micro- and nanotopography that enable control and enhancement of friction, adhesion, and compliance [16]. When used in grippers, these materials can modulate friction for object manipulation, improve the security of grip by increasing friction or adhesion, reduce damage to gripped objects by increasing compliance, and enable adaptive responses to changing grip conditions.

While many works in the literature have created surfaces that can efficiently tune contact properties, these surfaces are often expensive and laborious to manufacture, making them impractical for typical robotic gripping applications. Moreover, the simpler or more easily manufactured surface designs that *have* found use in gripping typically only use reactive adaptation or investigate only a single common shape of microtopography. In contrast, the designs explored in this work use active surface deflection to change the morphology of a grip surface covered in different types of microtopography. Grip conditions are thus controlled at three lengthscales, combining microscale effects from surface topography, mesoscale effects from surface morphology, and macroscale effects from gripper articulation.

This thesis introduces an active friction-tuning mechanism that is implemented with common prototyping materials and digital fabrication techniques. The friction-tuning mechanism incorporates an embedded pneumatic channel that is used to deflect an array of active regions on a thin, flexible, microtopography-covered grip surface. When the mechanism is used in adaptive gripper fingerpads, friction can be tuned by modifying contact between the gripper and an object using controlled surface deflection. This adaptive surface design, unlike most other designs in the literature, does not rely on moulded components or specialized equipment; rather, its fabrication process leverages digitally fabricated and off-the-shelf components that minimize the hands-on fabrication workload and permit straightforward repair and customization.

In this work, friction-tuning adaptive fingerpads are installed in a commercially available robotic gripper. The adaptive behaviour of the fingerpads is characterized by measuring the shear (friction) force experienced by gripped objects subjected to applied shear load. The shear force results show that friction at the grip interface varies with the actuation state of the adaptive fingerpads, indicating that this mechanism can be used to reliably tune friction. Moreover, in certain cases, actuating the adaptive fingerpads enables both pressure-based object detection and interlocking and enveloping interactions, demonstrating that the adaptive surface design is useful as both a sensor and an actuator.

Friction-tuning adaptive fingerpads could have several useful applications in robotic manipulation. For instance, the mechanism introduced in this thesis could be applied to control of in-hand
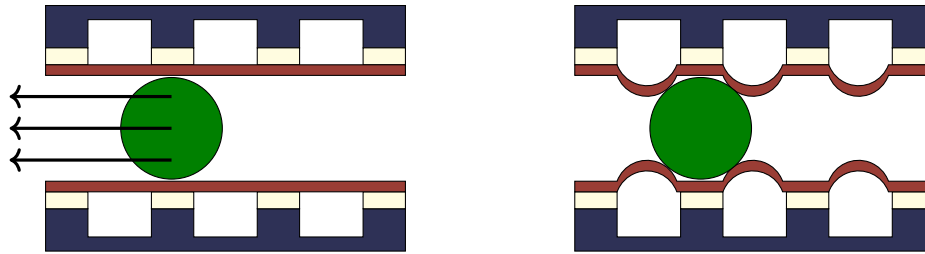
(a) Actively adaptive fingerpads could be actuated from a neutral state (left) to an inflated state (right) to *arrest* sliding, or actuated from an inflated state to a neutral state to *promote* sliding.
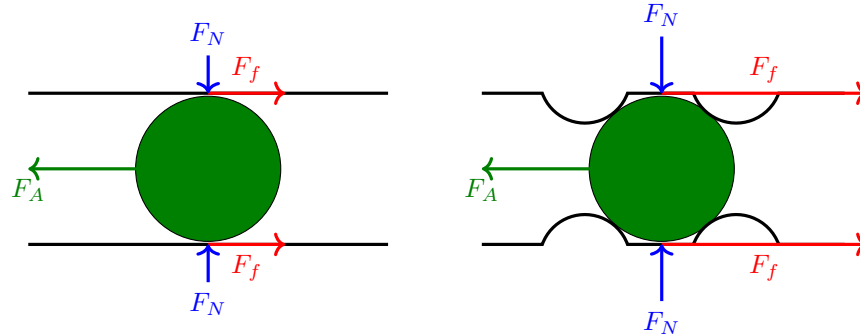
(b) When adaptive fingerpads are inflated, the normal forces acting on a gripped object increase slightly and the shear forces increase moderately, especially if enveloping occurs (as in this conceptual example showing a small, round target object). Increased shear grip forces increase friction, potentially decreasing or even arresting object sliding.

Figure 1.1: Conceptual diagram of one potential application of adaptive fingerpads: control over in-hand object sliding.

object sliding. The shear force testing conducted in Chapter 7 demonstrates that inflating adaptive fingerpads meaningfully modulates their frictional properties. If a gripped object is subjected to an applied force and begins to slide out of the grasp, the adaptive fingerpads could be inflated to rapidly increase grip friction, enhancing the frictional forces acting against object sliding and thereby reducing or arresting sliding (as shown conceptually in Figure 1.1). This concept could also be applied in reverse: if an object must be released gently (e.g., for object handovers), the object can be gripped with initially inflated fingerpads. The fingerpads can then be deflated to their neutral state, reducing grip friction and promoting object sliding. Similarly, in-hand manipulation or extrinsic manipulation tasks could be facilitated by friction tuning. Adaptive fingerpads enable active control of grip friction, allowing contact conditions at the grip interface to be modulated for more secure grip and more dexterous manipulation.

Chapter 2

Thesis Objectives

The main objective of this thesis is to design and characterize a practical multi-level adaptive grip surface that can actively tune friction at the grip interface. This work addresses the following research questions:

RQ1 How does multi-level active surface adaptation influence shear grip strength and shear friction?

Hypothesis: Surface deflection toward a gripped object (inflation) will increase grip friction.

Hypothesis: Surface deflection away from a gripped object (deflation) will decrease grip friction.

Hypothesis: Adding microtopography to grip surfaces will increase grip friction.[1]

Hypothesis: An active microtopography-covered surface will experience higher grip friction than either an active flat surface or a neutral microtopography-covered surface; i.e., multi-level adaptation will have synergistic effects.[2]

RQ2 How does the order of operations when using multi-level surface adaptation in a gripping process impact grip friction?

Hypothesis: Since the gripper used in this work stops closing its fingers when object contact is detected, "prior" inflation of the adaptive grip surface pre-gripping (such that initial contact between an object and the grip surface occurs only in the raised active regions) will result in decreased contact area and decreased friction, whereas "live" inflation of the surface post-gripping will result in increased contact area and increased friction.

RQ3 Can we leverage knowledge of the pressure in the pneumatic chamber to draw conclusions about changing grip conditions?

Hypothesis: When the adaptive grip surface is inflated prior to gripping, the pressure in the pneumatic chamber will increase when an object is gripped.

RQ4 Can we use grip surface adaptation to facilitate macroscale grip interactions like interlocking and enveloping?[3]

Hypothesis: When gripping small objects, more enveloping/interlocking interactions will be present when the adaptive grip surface is inflated than when it is neutral.

Hypothesis: When the adaptive grip surface is deflated while gripping objects with protrusions at a lengthscale similar to the active region lengthscale, interlocking will occur.

---

[1]See Section 3.2.3 (*Artificial Adaptive Surfaces*, pg. 14) for discussion of microtopography in surface adaptation.
[2]See Section 3.3.2 (*Advantages of Multi-Level Adaptation*, pg. 24) for a note on synergy in multi-level adaptation.
[3]See Section 3.3.1 (*Adaptive Compliance in Robotic Gripping*, pg. 22) for a note on interlocking and enveloping.

Chapter 3

Background and Literature Review

This chapter presents general background on robotic grippers and adaptive surfaces in Section 3.1 and Section 3.2 respectively. Section 3.3 summarizes adaptive surface grip designs in the literature and motivates the adaptive surface design proposed in this thesis.

3.1 Robotic Grippers

This section provides a brief overview of robotic gripping with a focus on soft robotics.

3.1.1 Robotic Manipulation

Manipulation is the main way in which most robots can interact with objects in their environment, and is therefore a crucial area of study. Although manipulation has been the focus of extensive development efforts for many years, it remains a major open problem in robotics [17], [18]—manipulation is a difficult task, particularly when the objects that must be manipulated vary in size, shape, or texture. Manipulation is a broad problem space that encompasses a variety of robot tasks, including grasping (picking up and holding an object) as well as in-hand manipulation (moving an object relative to the initial grasp) [4], [19]. This work focuses on *gripping*, the mechanical task of maintaining a grasp.

Robotic manipulation is now common in industry, but primarily in applications where grasping tasks are highly specialized. Industrial gripper designs tend to perform well on a narrow range of target objects and on repetitive, predictable tasks like machining or assembly [1]. For instance, robotic manipulation is underutilized in agriculture, where many target objects (e.g., fruits) are difficult to handle because of their fragility and size and shape variance [20]. Similarly, lack of gripper versatility severely hinders the development of general-purpose robots (e.g., service robots [19], [21]), which must handle assorted everyday objects and thus cannot rely on specialized grip approaches.

Versatility limitations pose a major design problem for robotic grippers. Gripping is challenging: objects can be dropped if the grip is insufficiently secure or damaged if the grip is insufficiently safe. Since secure and safe grip strategies differ depending on object shape, size, and composition, creating a truly versatile gripper is difficult. For instance, a gripper that can hold a fragile object delicately may not be strong enough to lift a heavy object securely.

Grip configurations fall into two categories: force closure (applying force at specific contact points to counteract object wrenches) and form closure (enveloping or wrapping around the object so that object wrenches cannot move it) [4]. Simple examples of form and force closure are shown in Figure 3.1. Force closure can fail when the object slips from between the force application points, but form closure typically only fails when the position of the fingers is moved such that the object ceases to be enclosed/wrapped. Form closure is thus more secure than force closure; however, form closure is not always possible [4], [22].
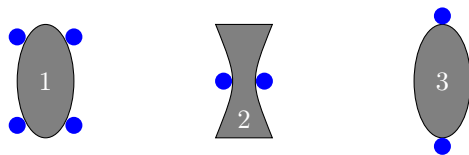
Figure 3.1: Simple examples of form and force closure in planar grasps with contact points drawn as blue dots. Grasps 1 and 2 have form closure while grasp 3 does not. *Based on Fig. 28.8 from Prattichizzo and Trinkle [4] and adapted with permission.*

Force closure is achieved by creating strong frictional contacts, an approach that reduces the complexity of the required contact patterns but increases the risk posed to objects. When attempting force closure on fragile or deformable objects, conventional robotic grippers may overestimate or underestimate the forces required, reducing the safety and security of gripping compared to human performance on similar tasks [1], [5], [23]. Excessive grip forces risk overloading or shocking fragile objects, while insufficient grip forces increase the risk that objects can slip [20]. Tactile sensors can help to mitigate this issue with accurate contact force feedback, but tactile sensing is still not commonly used in industry [18], [24], [25].

The design space for grippers is highly varied and includes both rigid grippers and soft grippers. Most industrial manipulators use rigid parallel-jaw grippers [26], [27]; (semi-)soft vacuum grippers and rigid fingered grippers are increasing in popularity but still less common [18]. Rigid grippers typically use impactive gripping (i.e., squeezing the sides of a gripped object) to achieve force closure [1]. Some rigid gripper designs attempt to reduce the risk of damaging delicate objects using underactuated mechanisms (which have fewer actuators than degrees of freedom, producing adaptive behaviours like those shown in Figure 3.2b) and/or compliant joints (shown conceptually in Figure 3.2a), both of which permit passive morphological adaptation to the shape of gripped objects [18], [19]. However, impacts from unyielding rigid grip surfaces can still damage gripped objects [1]. Grippers can be designed with structural compliance (e.g., as in Figure 3.2c) so that their rigid surfaces can flex or bend, but structurally compliant designs can be complex and may still not be sufficiently compliant to be safe for fragile objects. For this reason, many recent works that focus specifically on manipulation of fragile objects (e.g., for agricultural tasks [18], [20], [28]–[30]) use inherently compliant materials to fabricate grippers with soft surfaces.

3.1.2 Soft Grippers

Soft grippers are grippers that have inherent compliance due to the use of soft materials (such as elastomers) or compliance-increasing geometry [31], [34]–[36]. The actual degree of soft material usage varies; while many soft grippers use elastomeric materials throughout, hybrid rigid-soft grippers are becoming increasingly popular [37], [38]. Some approaches may also augment rigid grippers

(a) Conceptual depictions of compliant materials used in different gripper regions. *Adapted from Chang et al. [31] under* CC BY 4.0.

(b) Underactuated gripping: unobstructed closing leads to a parallel grasp (left) whereas object contact leads to an enveloping grasp (right). *Copyright 2014 Sage Publications. Adapted from Ciocarlie et al. [32] by permission of Sage Publications.*

(c) A structurally compliant gripper in its undeformed state (shown here in translucent black) overlaying its deformed state (solid black). *Copyright 2020 ASME. Figure and caption adapted from Milojević et al. [33] with permission.*

Figure 3.2: Different approaches to shape adaptation in gripping: (a) adding components made of compliant materials, (b) underactuated gripping, and (c) structural compliance.

by adding a few soft elements in key locations. Many soft grippers include embedded elements like actuators or sensors, which may be rigid but are more often flexible [17], [34], [37]. The most common actuation methods in soft robotics are pressure-driven (pneumatic or fluidic) actuation and tendon-driven actuation [17]. Pneumatically actuated soft grippers include the classic PneuNet design, which consists of an array of inflatable chambers embedded into an elastomeric gripper finger that bends when the chambers are inflated [38], [39].

Grippers made of soft, compliant materials can improve grip safety and security [1], [17]. The inherent compliance of soft grippers allows them to easily conform to the shape of a gripped object. The risk of damage to a gripped object is thus reduced both because grip contact area is increased (especially on curved or oddly shaped objects) and because the compliant gripper surface will yield through compression if an object is gripped too tightly [1], [5], [18], [29], [40], [41].

However, these performance benefits come at the cost of grip strength and speed. Soft grippers tend to have a lower load capacity, which limits versatility with respect to target object mass [29], [41], [42]. Actuation of pressure-driven grippers can also be slow and inefficient because of their intrinsic compliance and flow inertia [1]. This sluggish performance precludes soft grippers from being used in high-speed industrial applications.

Soft grippers have both advantages and disadvantages in terms of control complexity. Their high compliance complicates modelling and state estimation, meaning that conventional control methods do not apply [1], [5], [17], [41]. However, soft materials also benefit from *morphological computation*, where design morphology can lead directly to desirable behaviours through environmental interactions— meaning that certain control aspects are encoded within the body's natural response to the environment and need not be explicitly modelled or controlled [38], [43], [44].

Gripping methods can be classified into four different types [29], [45]. The most common method is impactive gripping, in which objects are squeezed or pinched to apply normal loads and create frictional contacts. In ingressive gripping, object surfaces are penetrated (e.g., with hooks or spines). In contigutive gripping, grippers use adhesion (typically modulated by shear loading) to create strong frictional contacts [29]. By contrast, astrictive gripping (e.g., suction) uses attractive forces and may not require object contact at all.

Grippers, including soft grippers, can also be classified as either anthropomorphic (i.e., fingered, resembling the human hand) or non-anthropomorphic [1], [19]. Anthropomorphic grippers have many kinematic degrees of freedom, increasing both dexterity and complexity [1], [18]. Non-anthropomorphic grippers (like the gripper shown in Figure 3.3b) include simplified fingered and parallel-jaw grippers as well as grippers that depart from the impactive grip strategy entirely. For instance, biomimetic non-anthropomorphic soft grippers span a fascinating array of gripping strategies ranging from body-level mechanisms (e.g., enveloping, wrapping) to surface-level mechanisms (e.g., adhesion, suction) [1].

(a) Multifingered gripper demonstrating different types of impactive grasps. *Figure and caption adapted from Ruotolo et al. [11] with permission from AAAS.*

(b) Grasping modes of a multimodal gripper. b: Expansion. c: Expansion-driven suction. *Copyright 2021, IEEE. Figure and caption adapted from Hao et al. [46] with permission.*

Figure 3.3: Example grippers that are comparatively (a) *more* and (b) *less* anthropomorphic.

It can be beneficial to combine gripping mechanisms—for example, Hao et al. made a non-anthropomorphic soft gripper (shown in Figure 3.3b) that used a combination of enveloping, adhesion, suction, and inflation to grip, enabling a variety of different grip modalities and configurations [46]. Soft grippers benefit from broadly useful material properties (compliant surfaces, large contact areas that produce large shear forces, and enhanced frictional forces that reduce the need for large applied normal forces) that can be leveraged for different gripping modes and hence facilitate multimodal design [1].

Many soft gripper designs attempt to improve gripping of soft and fragile objects by reducing normal grip force [1], [5]. This approach typically involves replacing, augmenting, or supporting impactive gripping; the goal is to reduce grip pressure while still maintaining high contact friction to prevent object sliding. This process requires modification of gripper material properties, often using adaptive surfaces, and therefore depends on a good understanding of the contact mechanics involved in gripping.

3.2 Adaptive Surfaces

For the purposes of this work, an adaptive surface is a surface whose contact properties can be modified controllably, repeatably, and (for active surfaces) dynamically. The terms used in the literature to describe this type of surface are not consistent; alternative words used in place of "adaptive" include "tunable", "switchable", "switching", and "controllable".

3.2.1 Types of Adaptive Surfaces

Adaptive surface designs vary widely, but can generally be classified based on the surface property that they modify and the scope of the adaptation relative to the surface substrate.

Typical Modified Properties

Adaptive surfaces modify properties that affect interactions with contacting objects: namely, adhesion, friction, and compliance.[1]

Friction is the force that acts against relative movement between surfaces in the shear direction [47]. For flat non-adhering surfaces, friction can generally be described using the Amonton-Coulomb law and the static (μ_s) and dynamic (μ_d) coefficients of friction between two surfaces [16], [48]. When two rough surfaces are in contact with no relative motion (sliding), the Amonton-Coulomb law states that the surfaces will not slide under the influence of an applied force F_a so long as the applied force is less than the product of the static friction coefficient and the normal force F_n:

$$F_a < \mu_s F_n \tag{3.1}$$

When the two rough surfaces begin to slide, the Amonton-Coulomb law states that the applied force F_a required to maintain constant-velocity sliding is equal to the product of the dynamic friction coefficient and the normal force:

$$F_a = \mu_d F_n \tag{3.2}$$

The Amonton-Coulomb law does not accurately describe the behaviour of adhering surfaces (including elastomeric materials), nor does it apply directly to patterned surfaces [16]. It also does not explain stick-slip behaviour (an unpredictable phenomenon for which the friction force and sliding velocity are periodic as in Figure 3.4), nor does it account for the influence of sliding history on peak static friction (where static friction magnitude increases as a contact ages) [49]–[51].

Adhesion is the force that acts against surface separation in the normal direction [47]. A working definition of adhesion, given by Jagota and Hui, is that adhesion is "stick[ing] well enough to a surface" [16]. A more technical definition is that adhesion is a process that joins solid bodies together using bonds (usually chemical or physical) that form at the interface when the bodies are brought into close contact. In adaptive adhesives, these connections could be the result of covalent or ionic (chemical) bonds; however, many adaptive adhesives use physical bonds formed as a result of either van der Waals interactions ("dry" adhesion) or capillary forces ("wet" adhesion) [15], [52]. Mechanical connections between surfaces (e.g., interlocking connections) are sometimes also included in the definition of adhesion [52].

---

[1]A more general definition could include materials that modify other properties (colour, optical clarity, etc.), but this work focuses on adaptive surfaces for gripping and so limits the definition to focus on contact properties.
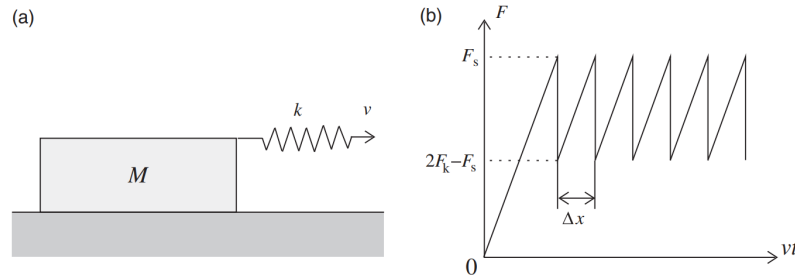
Figure 3.4: (a) A block of mass m pulled by a spring over a flat substrate. (b) Time dependence of the spring force in the quasi-static limit $v \to 0$, where F_s is static friction and F_k is kinetic friction. Stick-slip behaviour is visible as oscillations in shear force. *Copyright 2015, Cambridge University Press. Figure and caption adapted from Gnecco and Meyer [49] with permission.*
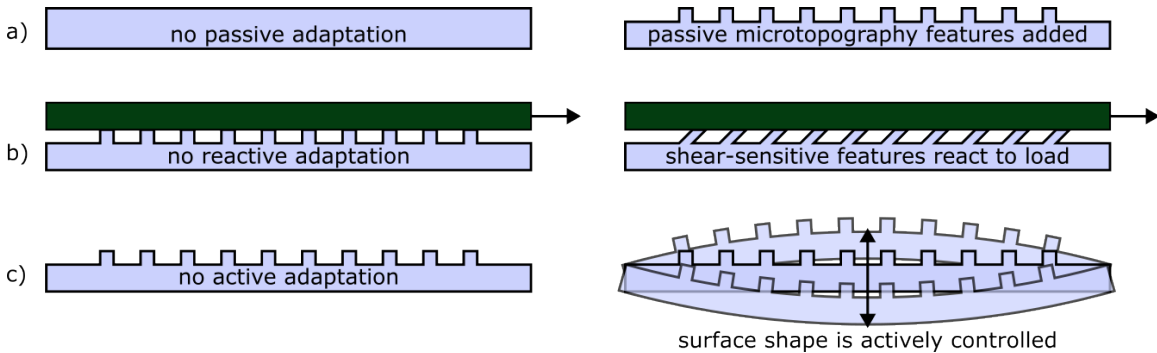
Figure 3.5: Three different levels of surface adaptation: a) passive, b) reactive, c) active.

Compliance is the "give" in a surface; a highly compliant surface is displaced easily with low force. A compliant surface may be composed of a compliant material (i.e., the bulk material itself has a low elastic modulus) or have a compliant structure (i.e., the bulk material may have a high elastic modulus, but the structure of the surface allows bending and buckling). A surface that has a compliant structure but is not made up of a compliant material is said to have a low *effective elastic modulus* [53].

Scope of Surface Adaptation

Depending on the approach and application, the level of control used in an adaptive grip surface design may range from the addition of passive features to reactive behaviour to full active control. These three levels of surface adaptation are depicted conceptually in Figure 3.5.

Passive adaptation is driven by materials science and incorporates specific material choices and/or modifications (e.g., microfeatures) to facilitate specific grip conditions. For instance, adding soft elastic elements to increase compliance could be considered passive adaptation, as the elastic elements' surfaces can passively conform to the shape of a gripped object [5].

Reactive adaptation couples surface adaptation to grip motion or forces such that the act of gripping drives adaptation. Examples include directional adhesives that couple adhesion modulation to grip closure [24] as well as materials with strain-controlled roughness [54].

Active adaptation uses external actuators to modify grip surface properties through surface motion or changes in morphology. For instance, pneumatic actuation can be employed to inflate

channels under a surface, creating reversible surface roughness changes [55]. Active behaviour is decoupled from grip actions and controlled by an independent actuator; as a result, active control is the most customizable option. Adding active behaviours enables hierarchical control approaches, where surface control and grip control can operate at different levels and lengthscales.

3.2.2   Contact Mechanics

Contact mechanics is a complex field that involves drastically different effects at different length-scales. However, since surface adaptation in this work operates at the millimetre lengthscale, the high-level concepts presented in this section are sufficient to inform discussion of adaptive surface behaviour and characteristics.

Rough Contacts

Common material surfaces are not smooth on an atomic scale; rather, they have asperities (individual features of roughness, usually represented as bumps or arbitrarily shaped protrusions) at some lengthscale. The contact between two solid surfaces is mainly contact between their asperities, and the *actual* contact area is small in comparison to the *apparent* contact area [53], [56].
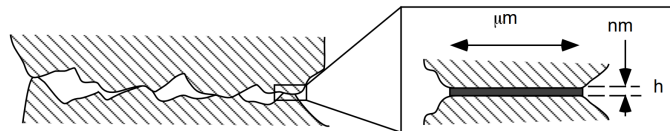
Figure 3.6: Multicontact interface, where microcontacts between asperities make up the actual contact area. The inset shows a single microcontact with the contact junction shaded. *Figure and caption adapted from Baumberger and Caroli [50] with permission from Taylor & Francis.*

Viscoelastic Contacts

The elastomeric materials used in soft robotics have low elastic modulus values and typically exhibit viscoelastic behaviour. A viscoelastic material has a time-dependent modulus $E(t)$ [57]. When stress is applied to the material, strain increases rapidly and almost immediately (elastically), but then increases at an exponentially decreasing rate (viscously). Since viscoelastic flow takes time, the contact area between a viscoelastic material and a target surface will increase (up to a limit) if the timescale for contact formation increases [58].

Adhesive Contacts

Adhesive contacts are formed by chemical and/or physical bonds[2] that hold two contacting surfaces together. Adhesive strength can be measured as the stress required to separate two adhered surfaces. Under the assumption that adhesive behaviour is uniform across an adhered area, the pull-off force can then be computed using this strength and the adhered area [16].

---

[2]Mechanical bonds are not included in the contact mechanics definition of adhesion. Comparatively macroscale connections (like interlocking geometry) are not in themselves adhesive contacts; rather, they rely on adhesive and frictional interactions at individual contact points at a much smaller lengthscale.

Interplay between Adhesion, Friction, and Compliance

The adaptive surfaces discussed in this work are non-negligibly rough, may be viscoelastic, and vary in their adhesive properties. The relationship between their adhesion, friction, and compliance is hard to specify because these contact properties influence one another significantly. For instance, compliance heavily impacts adhesion because compliant materials can more easily deform to increase adhesive contact area—for viscoelastic materials, this also means that adhesive connections will generally grow stronger as the compliant materials slowly fill in defects at the interface [59].

Similarly, adhesion and friction are interrelated. Increasing roughness can both increase friction and decrease adhesive contact area—for instance, tape sticks more easily to glass than concrete. Rougher surfaces require adhesive bonds to form over a larger distance, weakening physical bonding and necessitating higher levels of elastic strain to improve contact area [56], [60]. Adding to the complexity of analyzing contact properties, depending on the analysis context, friction might be considered merely a component of adhesion (or vice versa) rather than a separate phenomenon.

3.2.3   Artificial Adaptive Surfaces

Modifying adhesion, friction, and/or compliance changes the nature of a contact. The design of adaptive surfaces is motivated by the challenge of modifying these properties controllably and reliably. To achieve this, many adaptive surface designers take inspiration from the excellent adaptive surfaces found in nature. For instance, biomimicry has led to a variety of artificial adaptive surface designs inspired by gecko adhesion (micropillar surfaces), snakeskin friction (anisotropic textures), and insect claws and spines (microspines). This section discusses biomimicry for adaptive surfaces, categorization of adaptive surfaces, and microtopography design.

Role of Biomimicry

Many animals have adaptive contact surfaces that facilitate locomotion or grasping. For instance, friction can be increased during locomotion using claws at the ends of toes/tarsi, arrays of sharp microspines, or rough, textured friction pads [61], [62]. Even flying animals like birds can benefit from friction adaptation; for instance, birds use their high-friction, compliant toepads and sharp claws to perch securely and to grasp prey [63]. Claws are thought to help animals attach to surface asperities through interlocking, where the claw hooks against an asperity and applies a shear force [61]. Claw geometry and substrate roughness influence the resultant attachment force [61], [64], [65].

While friction from claws/microspines/friction pads helps an animal to climb an inclined/vertical surface by resisting forces that are *parallel* to the surface, adhesion helps resist forces that are *perpendicular* to the surface, allowing an animal with sufficiently strong adaptive adhesion to climb even overhanging surfaces [47], [66], [67]. Although the specific morphology and lengthscales of adhesive organs vary greatly, the most widespread mechanism for terrestrial bio-adhesion is *shear-induced (directional) adhesion* [62]. Shear-induced adhesion enables rapid dynamic attachment with each stride: shearing an adhesive pad by pulling down towards the body increases adhesion, while shearing the pad by pushing up away from the body decreases adhesion [15], [62].

The most famous example of shear-induced adaptive adhesion is the fibrillar adhesive system of the gecko. Gecko toepads are covered in small, thin, keratin-based fibrils that form structurally compliant hierarchical branching structures with an effective elastic modulus that is much lower than
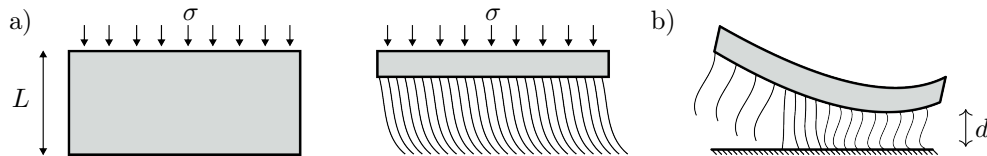
Figure 3.7: Two advantageous features of fibrillar adhesion. a) If an elastic block is replaced with a dense array of fibrils constructed from the same material, its effective modulus is less than its bulk modulus ($E_{\text{eff}} \ll E$), so the fibril array will be able to deform by a greater distance than the original block. b) Since long, curved fibrils must first straighten before separating from a contacting surface, the interface must separate by a distance greater than the substrate-contact surface separation d. This increases the energy required to propagate a crack through the adhesive interface. *Adapted from Figs. 1 and 3 from Persson [68] with permission from AIP Publishing.*

the bulk elastic modulus of keratin [16], [57], [66], [68]. The adaptive adhesion of geckos relies on the anisotropy in their adhesive structures [15], [16], [62]. Fibrils are non-adhesive in their default state because their tips tilt away from contact surfaces. When sheared, the structurally compliant fibrils bend and their tips become parallel to the contact surface, enabling van der Waals interactions. Gecko adhesion also benefits from inelastic events: as the gecko adhesive surface is moved away from a target surface, the curved fibrils first straighten and elongate (as in Figure 3.7) before being pulled off, increasing the separation distance required to break the adhesive connection [68].

Biomimetic adaptive surfaces are often designed based on animals in environmental conditions that are analogous to the desired operating conditions of the artificial surface [69]. For instance, for adaptive adhesives, octopus-like vacuum suction is used in underwater conditions [70], tree frog-like microfeature arrays with grooves for fluid flow are used in damp conditions [71], and gecko-like anisotropic micropillar arrays are used in dry conditions [15], [16].

Adaptive surfaces are not exclusively biomimetic—other common strategies like active electromagnetic, fluidic, or smart surface control are not found in biology. However, the popularity of biomimetic approaches is enduring and is likely to continue to grow, especially in robotics applications of adaptive surfaces. In fact, Science Robotics has included "Biohybrid and Bioinspired Robotics" in its list of ten Grand Challenges [72].

Categorization of Adaptive Surfaces

Adaptive surfaces are primarily defined by the property that they modify. However, there is overlap: adaptive adhesives can also typically adapt friction, but not all adaptive friction surfaces are effective adhesives. Similarly, many adaptive compliance designs also modify adhesion and/or friction. This work differentiates adaptive adhesion and adaptive friction surfaces as follows:

- adaptive adhesion surfaces primarily aim to increase the force required to separate an object from the surface in the perpendicular (normal) direction
- adaptive friction surfaces primarily aim to increase the force required to move an object relative to the surface in the parallel direction

This is based on recommendations from Arzt et al. that differentiate adhesion testing and friction testing for functional surfaces [53]. For the purposes of this work, adaptive surfaces are classified as adaptive compliance surfaces only if they do not meet the criteria for adaptive adhesion or adaptive friction surfaces.
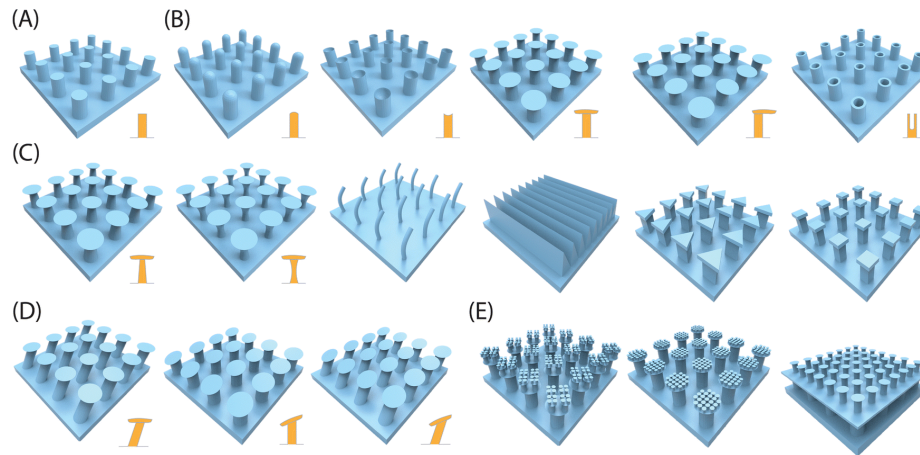
Figure 3.8: Models of dry adhesive microtopography structures. (A) Vertically aligned micro- and nanofibres. (B) Tips with different shapes. (C) Fibrils with different shapes. (D) Anisotropic structures, including sloping fibrils, sloping tips, and a combination of both. (E) Hierarchical structures. *Figure and caption adapted from Li et al. [73] under CC BY 3.0*
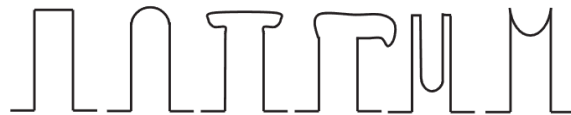
Figure 3.9: A variety of different tip shapes that are used for bioinspired micropillars. *Copyright 2007, IEEE. Adapted from del Campo et al. [75] with permission.*

Surface Microtopography

Surfaces with microtopography have patterned features engraved into or added onto a base substrate. Microtopography can be used to drastically change the properties of a surface [53] and is often used in adaptive materials, either to add passive adaptive effects or in concert with reactive/active adaptation. As with "adaptive" surfaces, the terminology used in the literature for surface microtopography is inconsistent. Alternatives for "microtopography" include "microfeature", "microtexture", and "micropattern" (as well as derivatives with different prefixes, e.g., "nanotopography").

Microtopography surfaces include gecko-inspired micropillar arrays, which have useful adhesion properties because of contact splitting and load sharing [16], [41] and are now widely used in dry adhesive research and product design [53], [74]. The micropillar array is the most common microtopography form factor in adaptive surfaces, although designs vary widely—some micropillar design variations are depicted in Figure 3.8. Tip shapes for micropillars and other microtopography features are also well-studied, and various reviews provide an overview of different common tip shapes (some of which are shown in Figure 3.9) [16], [73], [75]. Some designs use hierarchical structures to stack microtopography on top of larger structures, with the goal of creating structural compliance like that found in the hierarchical gecko adhesive system and thereby increasing adhesion-controlled friction [76], [77].

Both custom and commercial microfeatured surfaces are now found in research across many fields and information about manufacturing microtopography surfaces is now readily available [53], [56], [78], [79]. The materials used to construct microtopography surfaces vary from soft elastomers to

hard carbon fibre nanotubes [77]. Microtopography features could be constructed using the same material as the base substrate, or features could be constructed of one material/a composition of different materials and added to a base substrate composed of another material.

Manufacturing techniques for microtopography also vary. Approaches include both bottom-up techniques (e.g., drawing of polymer hairs or growing CNTs with chemical vapour deposition) and top-down techniques (e.g., template moulding) [15], [77], [80]. Manufacturing at large scale remains a challenge, since most of these fabrication techniques are time-consuming and can have very low yield [15]. Some progress has been made in larger-scale manufacturing techniques for microtopography (e.g., roll-to-roll fabrication) [53], [56], [81], but these techniques still generally use highly specialized tools, are not standardized, have poor controllability, and/or are not suitable for all types of microtopography [77]. Some recent work has used 3D printing, a strategy that enables fabrication of varying types of microtopography quickly, with common prototyping equipment, and at a reasonable cost (although with limited resolution at small scales) [71], [82]–[84].

Several additional considerations need to be taken into account when testing the surface properties of microtopography surfaces, particularly those made from soft/elastomeric materials. For microtopography surfaces, friction experiments are generally performed under displacement-controlled circumstances—so the normal load on the surface may change but the displacement between the test apparatus and the adhesive sample is held constant [16]. The reason for this is to avoid buckling—microfeatures tend to fail and detach through either bending or buckling when shear load is applied under constant normal load. However, some testing approaches do control force rather than displacement—Assenbergh et al., for example, use springs to self-align their test apparatus contact surface [85], and force control is more applicable to surfaces with active control where the surface shape may change during testing. The frictional behaviour of soft microtopography features also depends on the history of sliding, meaning that frictional properties may differ after slip conditions have occurred [16]. Feature shape also impacts response to testing procedures; e.g., Moyle et al. found that ridge-shaped microtopography showed enhanced adhesion when tested with a rolling wheel but not when tested using indentation [86]. In general, care needs to be taken when developing and testing microtopography surfaces to ensure that their unique properties are accurately characterized and effectively optimized.

Surface Microtopography for Friction

Microtopography surfaces for *general* applications are typically evaluated using normal load. For *gripping* applications, however, we are more concerned about shear load, since the primary concern is that an object will slip from the gripper's grasp.

While most surface microtopography designs for shear loading aim to increase friction, a few designs instead aim to decrease friction. For instance, microtopography can be used to reduce wear in mechanical components (e.g., piston rings) by decreasing a surface's effective coefficient of friction [87], [88]. Microtopography can even be used to create surfaces with negative friction (i.e., surfaces for which friction decreases with increasing normal load) [89].

Studies of microtopography-based surface adaptation for gripping most often use fibrillar arrays of microwedges [92] or similar structures with tapered pillars or tips [52], [93]. Various works show that anisotropic microtopography creates surfaces with anisotropic frictional behaviour—e.g., Yu et al. use angled flaps [91] (shown in Figure 3.10b), Murphy et al. use angled micropillars with varying

(a) Block and post geometry. a: Schematics of attachment features consisting of an adhesive layer supported with an adherend with i) low (block) and ii) high (post) aspect ratios (t/h). t is thickness, h is height, and b is width. After attachment with a contact area $A = bh$, a shear force F is applied. b: Typical force plot during shear adhesion for a block and a post. The compliance, C, is the reciprocal of the slope. The interface fails at a critical force capacity F_C. *Copyright 2012, John Wiley and Sons. Figure and caption adapted from Bartlett et al. [90] with permission.*

(b) Angled flap geometry. a: Single angled long flap with arrows to show forces. b: Friction forces when sliding in the $\pm x$ and $\pm y$ directions. c: Adhesion forces when sliding in the $\pm x$ and $\pm y$ directions. *Copyright 2011, John Wiley and Sons. Figure and caption adapted from Yu et al. [91] with permission.*

Figure 3.10: Designs and test results from works examining shear load on microtopography features.

tip shapes [94], and Baum et al. use scale-like structures inspired by the anisotropic properties of snake skin [95]. Taking a similar design approach using tip asymmetry, Wang et al. use pillars with stepped tips to bias peeling behaviour [96], and Khaled and Sameoto add defects to one side of their micropillars to create a similar bias [97].

A few related works explore the impact of specific microtopography design parameters in the context of adhesion and friction under shear load. For instance, Bartlett et al. found that (short) block geometry (shown in Figure 3.10a) creates stronger adhesion-controlled friction than (tall) post geometry [90]. Similarly, Hao et al. found that long microridges increased friction more when they are oriented perpendicular to the motion of a contacting surface than when they are parallel [3], and Zhang et al. came to the same conclusion for microgrooves [98]. As with gecko-inspired micropillars, contact splitting improves the adaptability of friction-focused microtopography features to rough surfaces—e.g., short strips of flap features have higher static friction than long strips when tested

in the direction perpendicular to the flaps [99]. Overall, microtopography features that effectively increase friction are typically shorter and have a lower aspect ratio than microtopography features for normal adhesion (e.g., taking the form of short wedges, blocks, or flaps), can be tilted or slanted, and perform best when oriented perpendicular to the expected direction of shear load.

3.3 State of the Art: Adaptive Grip Surfaces

This section summarizes related works with designs that adapt adhesion, friction, or compliance and are relevant to gripping. Related works are divided into two parts. In the first part, Section 3.3.1 discusses surfaces that adapt at a *single* level (i.e., only passive adaptation, only reactive adaptation, or only active adaptation). In the second part, Section 3.3.2 motivates multi-level surface adaptation and discusses a selection of multi-level adaptive surfaces.

The adaptive grip surface that is presented in this thesis primarily modifies friction and uses pneumatic control to actuate its active surface; as such, related works involving friction-tuning surfaces or pneumatically actuated surfaces are particularly relevant.

3.3.1 Single-Level Surface Adaptation

This section introduces a selection of adaptive grip surfaces, dividing the related works into three categories by adapted property: adhesion, friction, and compliance.

Adaptive Adhesion in Robotic Gripping

When used in grippers, adaptive adhesives can: improve grip security by adhering to a gripped object, reduce damage to gripped objects by increasing the gripper surface compliance, and facilitate dynamic response to changing grip conditions by adapting adhesion strength. Adaptive adhesion generally uses one of six approaches: buckling/strain, environmental stimulus response, magnetic adhesion and electroadhesion, suction, penetration/interlocking, or shear-sensitive patterned surfaces. Of these approaches, penetration and shear-sensitive surfaces are the most relevant and will be briefly discussed.

Penetration approaches, inspired by biological claws and spines, use small, sharp objects to pierce the surface of a gripped object, creating an interlocking adhesive bond. Many climbing robots use microspines to scale rough surfaces, often using track mechanisms [100], spring-loaded mechanisms [64], [101], or self-weight [102], [103] to pull microspines against surface asperities. Some also actively control the positions of microspines or claws (e.g., using pneumatic [104] or magnetic [105] actuation).

Many adhesive gripper designs use (typically gecko-inspired) micropatterned surfaces to create shear-sensitive adhesion. Some such shear-sensitive adhesives use isotropic micropillars [106], [107] while others use angled micropillars inspired by the anisotropic structure of gecko fibrils [108], [109]. The Cutkotsky group has developed a straightforward micromachining process for the creation of *directional microwedges*: shear-sensitive gecko-inspired adhesives made up of arrays of tilted wedges (pictured in Figure 3.11) [92], [110]. Many gripper designs use these microwedges to implement adaptive adhesion in both rigid [24], [111] and soft [41] grippers. Microwedge dimensions and layout vary by application; for instance, one adhesive gripper arranged the microwedges in rows of chevrons to improve resilience to moments applied during industrial manipulation [24].
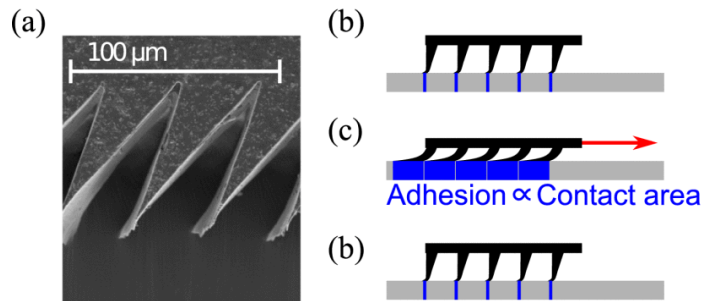
Figure 3.11: Dry adhesive with wedge-shaped microtopography. (a) Micrograph of material. (b) Tips self-engage with a surface when brought in contact. (c) When loaded in shear, the wedges lay over, and a large real contact area produces adhesion. (d) When the shear load is relaxed, the stored elastic energy in the wedges lifts them from the surface, allowing easy removal. *Copyright 2017, IEEE. Figure and caption reproduced from Hawkes et al. [110] with permission.*

Adaptive adhesive grippers often use the load applied by gravity on a gripped object to switch shear-sensitive adhesion *on*, and then use a peeling process to switch adhesion *off* (emulating the rolling gait used to detach gecko adhesive pads via peeling). This peeling is sometimes initiated *reactively*: if the direction of loading during gripping and releasing is known and consistent, adhesives can be designed to peel in response to loads that initiate grip release [14]. This peeling can also be initiated *actively*: release actuators can be used to lift or pull one side of the adaptive adhesive surface to help break the adhesive connection (e.g., using a belt drive [112]).

Adaptive Friction in Robotic Gripping and Locomotion

Adaptive friction surfaces have received far less attention than adaptive adhesive surfaces, partly because friction is sometimes considered a contributor to adhesion and friction adaptation is hence sometimes incorporated in adaptive adhesives. There are relatively few gripper designs that use adaptive friction; among robotics implementations, adaptive friction surfaces are most often used for locomotion. Adaptive friction surfaces are also often used in applications where friction *reduction* is desired, e.g., to reduce wear or decrease drag—in fact, the tribological behaviour of bioinspired adaptive friction surfaces has recently been reviewed with a focus on friction reduction [113]. In grippers, adaptive friction surfaces modulate the force required for an object to slide along the gripper surface and are typically used to increase friction for secure gripping.

This section presents relevant related works that use four different mechanisms for adaptive friction: snake-inspired anisotropic surfaces, surface wrinkling, mechanical surface retraction, and substrate deflection. Of these mechanisms, mechanical surface retraction and substrate deflection are the most relevant, as the adaptive grip surface proposed in this thesis uses substrate deflection as its friction-tuning mechanism. In addition to discussing adaptive friction surfaces for gripping, this section will also discuss a few related works on robot locomotion where relevant.

Anisotropic adaptive friction surfaces use asymmetric features or patterned multi-material combinations to create frictional effects that vary based on the direction of applied load. Many such surfaces are inspired by snake locomotion, which uses a combination of movable scales that tilt to adapt contact angle [114] (active adaptation) and microtopography with anisotropic friction properties (passive adaptation) [51], [95]. Since snakes experience larger friction forces when moving backward than when moving forward, their anisotropic skin allows them to leverage friction against
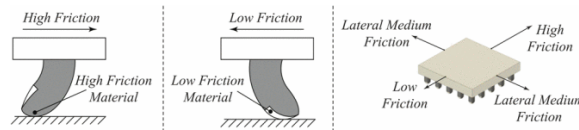
(a) Patterns of high- and low-friction material in contact surfaces for a crawling robot. *Copyright 2018, IEEE. Figure and caption adapted from Ta et al. [13] with permission.*
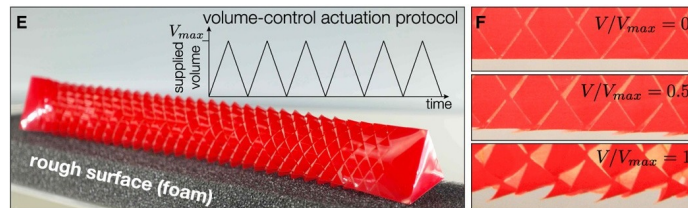
(b) Crawling robot with kirigami skin with a buckling-induced pop-up texture. *Figure and caption adapted from Rafsanjani et al. [121] with permission from AAAS.*

Figure 3.12: Examples of crawling robots that use frictional anisotropy at the contact surface.

the ground for efficient locomotion. Similarly, shark skin is covered with angled sawtooth-like denticles that show frictional anisotropy [115].

Robotic crawlers that augment skin with anisotropic microtopography have generally succeeded in showing frictional anisotropy and locomoting effectively [116], [117]. Crawling robots that use patterned multimaterial contact surfaces have had more varying results—some fail to move forward [118], whereas others (like the design that used the contact surfaces pictured in Figure 3.12a) can crawl effectively [13], [119]. Mei et al. [120] applied this concept at a larger lengthscale by incorporating rings of angled macroscale spikes at the head and tail of their robotic snake, where the spikes slid on their faces when pulled away from their tips (lower-friction) but penetrated into the contact surface when pulled toward their tips (higher-friction). Tramsen et al. [115] compared the effects of anisotropic sawtooth microtopography with different substrates. Interestingly, they found that rigid microtopography engaged in mainly mechanical interlocking and showed anisotropy on softer contact surfaces whereas soft microtopography engaged in mainly adhesion-mediated friction and showed anisotropy on harder contact surfaces [115]—this suggests that it may be beneficial to select the substrate for a microtopography surface based on the properties of target surfaces.

In the past few years, the use of kirigami (paper cutting) and origami (paper folding) skins for snake-like locomotion has become popular. Kirigami is a technique in which patterns of ordered cuts are made in a material in such a way that the cut sections bend out from the surface when the surface is strained in a specific direction relative to the cut pattern, turning a 2D sheet into a 3D texture. Robotic snake skin can be cut or folded to create controllable scale shapes (like those shown in Figure 3.12b) that enable frictional anisotropy during locomotion [121]–[123].

Controlled wrinkling can be used to change surface roughness. In some cases, surfaces are formed with permanent wrinkles that enable only passive adaptation [124]. In others, wrinkles appear or subside in response to triggers like mechanical strain, enabling active adaptation [125]–[127]. These surfaces usually increase friction in their wrinkled state, but wrinkles have also been found to *decrease* friction when they are much smaller than the asperities on the contact surface [126].

Some grippers with adaptive friction take the more mechanical approach of implementing a grip surface with retractable sections that can be pushed toward and/or pulled away from the grip

(a) Variable-friction finger. Elastic elements suspend the low-friction surface through the high-friction surface. *Copyright 2018, IEEE. Figure and caption adapted from Spiers et al. [128] with permission.*

(b) Gripper with origami-inspired variable-friction fingers. *Copyright 2020, IEEE. Figure and caption adapted from Lu et al. [10] with permission.*
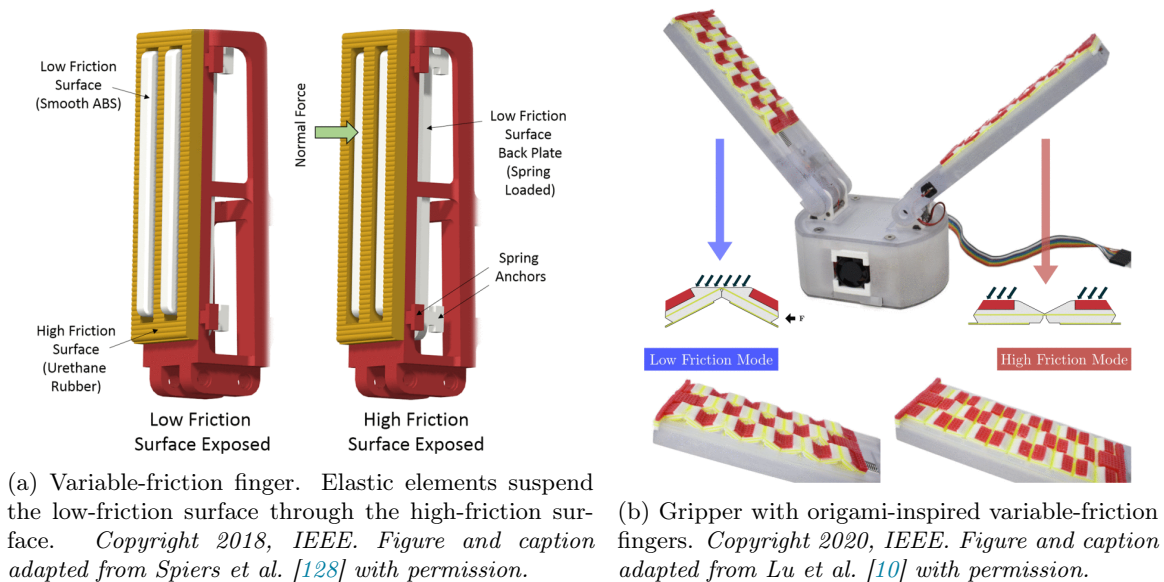
Figure 3.13: Two variable-friction grippers based on surface retraction.

interface. The main grip surface and the surface of the retractable sections typically differ in their frictional properties. For instance, Spiers et al. fitted a fixed high-friction gripper finger with a low-friction surface mounted on a spring (shown in Figure 3.13a) [128]. When an object was gripped lightly, the low-friction surface enabled easy object sliding and in-hand manipulation. When an object was gripped firmly, the spring compressed until the object contacted the high-friction surface, enabling secure gripping using reactive adaptation. Nojiri et al. used a similar dual-mode reactive approach but varied contact area rather than coefficient of friction [12]. Lu et al. extended this dual-mode approach to active adaptation by adding a separate actuator to control friction mode switching [10]. Their origami-inspired design, like that of Nojiri et al., folded to expose different surfaces (low-friction or high-friction) in different modes (as shown in Figure 3.13b). Active surface retraction can also be implemented with smart materials (e.g., Li et al. use a shape memory alloy wire [129]).

Substrate deflection moves regions of the grip surface to modify friction at the grip interface. In some implementations, substrate deflection is used to move rigid components to create different contact region shapes. For instance, Chavan-Dafie et al. made use of substrate deflection to create "shapeshifting" pneumatic fingers for manipulation of cylindrical objects, in which a hinged panel tilts into or out of the gripper finger under pneumatic pressure [130]. In other implementations, substrate deflection is used to bend a flexible membrane, often by using underlying pneumatic chambers to deflect the membrane using air pressure. For example, Trinh et al. designed a theoretical wrinkled finger in which a flexible membrane covered a series of pneumatic chambers, where the size and shape of the pneumatic chamber openings under the flexible membrane defined the size and shape of the wrinkles in the finger [131]. When the pressure in the chambers was higher than atmospheric pressure, the regions of the membrane that lay above pneumatic chambers swelled to form wrinkles. Interestingly, the majority of the membrane-based substrate deflection designs found in the literature appear to use only two pressure states (e.g., neutral and inflated, or inflated and deflated) rather than three (deflated, neutral, and inflated).

(a) Surface states (neutral and inflated).

(b) Surface incorporated into soft gripper.
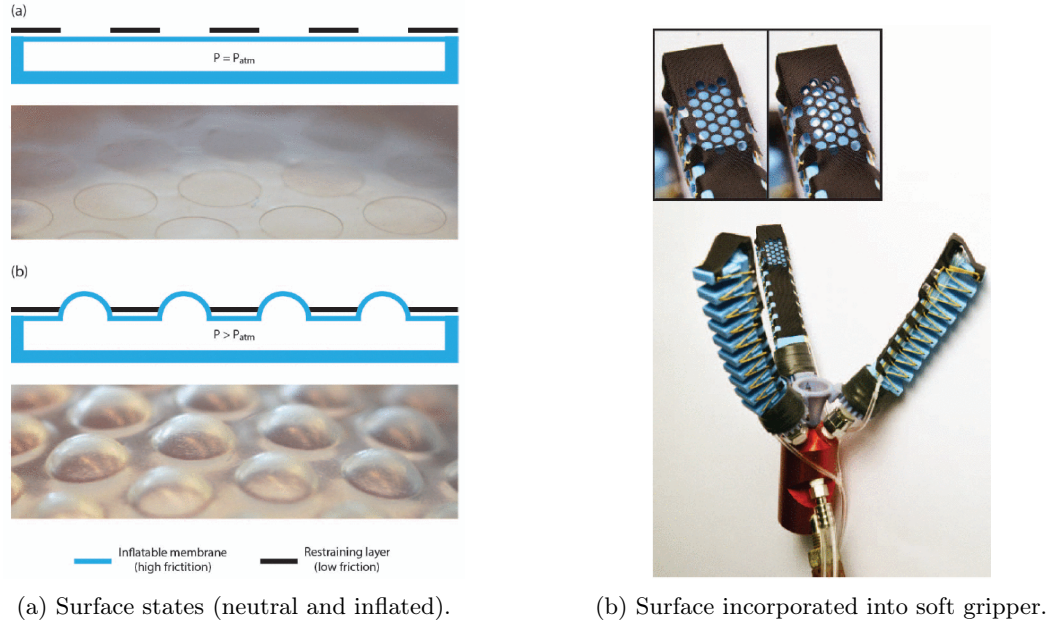
Figure 3.14: Tunable friction surface: (a) schematic and (b) implementation in a soft gripper. *Copyright 2017, IEEE. Figures reproduced from Becker et al. [55] with permission.*

A notable example from Becker et al. used flexible membrane deflection to create a soft adaptive friction surface in which they positioned a pneumatically actuated bladder (made from a flexible, high-friction material) under a thin constraint layer (made from a low-friction material) [55]. The constraint layer was patterned with an array of holes, which defined the surface actuation pattern. When the bladder underneath the constraint layer was inflated, its flexible surface pressed through the holes, forming an array of round bumps raised above the constraint layer. As a result, the surface had two states: a low-friction, neutral state defined by contact with the constraint layer and a high-friction, inflated state defined by contact with the raised bumps of the bladder material. This adaptive friction surface is shown alone and in a soft robotic gripper in Figure 3.14.

Adaptive Compliance in Robotic Gripping

Adaptive compliance is often incorporated into adaptive adhesion or friction surfaces, or is limited to the use of materials that passively deform to gripped objects (i.e., material or structural compliance). Those grippers that do reactively or actively adapt compliance generally use one of three approaches: structural compliance, belt tightening, or variable stiffness (the most relevant of these approaches).

Variable stiffness is the most common approach to active compliance adaptation and also the most diverse. Many variable-stiffness surfaces use stimulus-responsive materials like shape memory polymers [132]–[134] or thermoplastic polymers [135] to change the stiffness of gripper components. For instance, Yang et al. augmented a soft gripper with selective joint stiffening using shape memory polymer joints (Figure 3.15a) [136]. Other variable-stiffness surfaces use pneumatic control, which can: generate a vacuum for granular jamming [137] and layer jamming [138], unfold or collapse folding structures [139]–[141], peel adhesive surfaces [142], tighten membranes around a gripped object [143], [144], or inflate bladders to create a compliant contact surface [144], [145]. For instance,
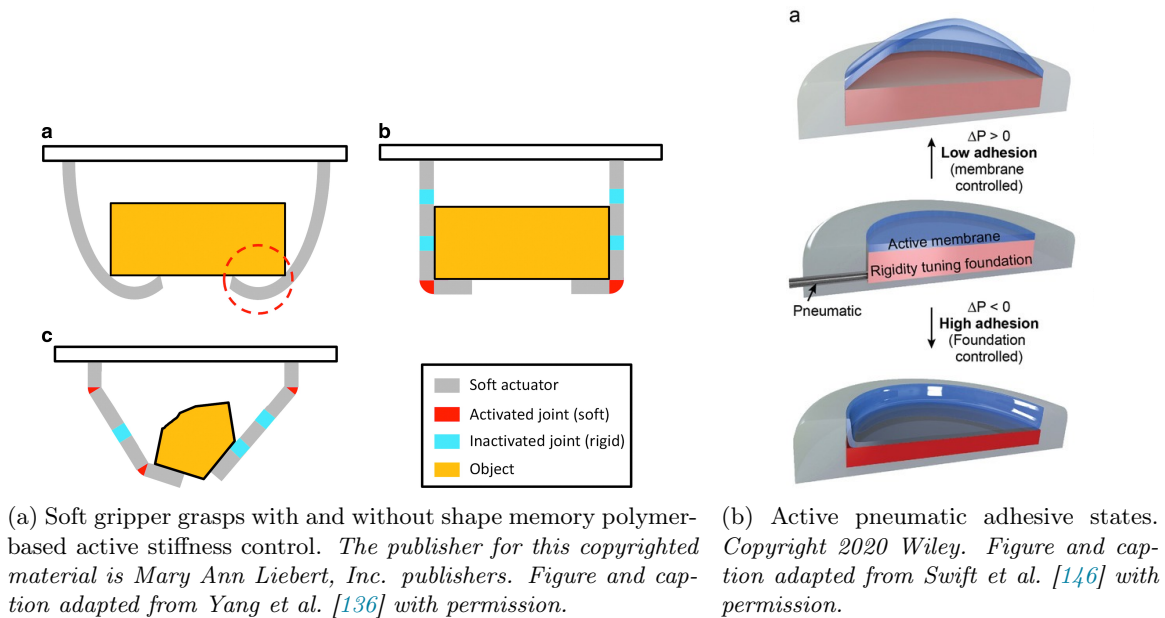
(a) Soft gripper grasps with and without shape memory polymer-based active stiffness control. *The publisher for this copyrighted material is Mary Ann Liebert, Inc. publishers. Figure and caption adapted from Yang et al. [136] with permission.*

(b) Active pneumatic adhesive states. *Copyright 2020 Wiley. Figure and caption adapted from Swift et al. [146] with permission.*

Figure 3.15: Schematics showing behaviour of grippers with variable stiffness actuated using two different mechanisms: shape memory polymer control and pneumatic control.

Swift et al. used pneumatic control of an active elastomeric membrane over a compressible foam foundation to create a system with three states (shown in Figure 3.15b): a high-compliance state that uses positive pressure to inflate the membrane, a neutral state, and a low-compliance state that uses negative pressure to compress the foundation [146].

The membrane inflation technique used to create the compliant contact surface shown at the top of Figure 3.15b is similar to the actuation approach proposed in this thesis, so this particular mechanism for variable stiffness merits further discussion. Inflatable membranes have long been used in soft robotics to envelop or wrap around objects, a macroscale form of surface adaptation that drastically increases contact area, sometimes even to the point of establishing form closure [4], [5], [29], [144], [147]. Some grippers augment rigid fingers with soft pneumatic fingerpads, but most such designs use only a single chamber on each finger [144], [145], [148], [149] or phalange [150], in which the entire fingerpad surface forms a single active region. Although these large active regions do increase compliance when inflated, they form large bubble shapes that can significantly laterally displace small objects near the sides of the pads. Using an array of multiple active regions instead of a single active region would both improve safety for small objects and provide contact splitting effects (which would allow adaptation to irregular object shapes with a different level of inflation at each active region location). In certain cases, when gripping objects of compatible shape and size, an array of inflatable active regions would also enable useful gripping interactions: as depicted in Figure 3.16, the active regions could deflate to interlock with convex features, or inflate to envelop convex objects or interlock with concave features. Despite the potential benefits of an array of inflatable active regions, there are very few works in the literature that take this approach. The most notable examples of arrayed active regions are the active inflatable fingertip put forward recently by He et al. [151], the theoretical wrinkled finger design mentioned in Section 3.3.1 [131], and some recent pneumatic sensor designs (e.g., from Gaudeni et al. [152]).

interlocking (convex)   partial enveloping   interlocking (concave)
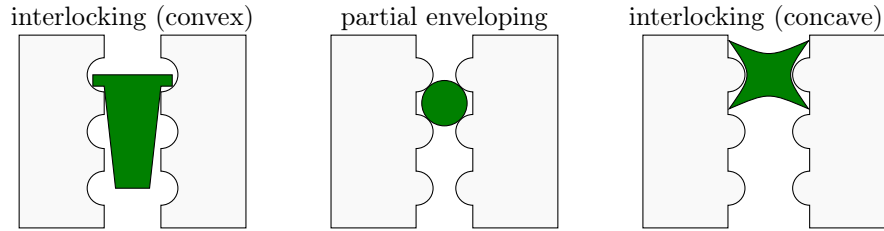
Figure 3.16: Different types of macroscale contact modification using the pneumatic membrane control approach to varying surface stiffness. A patterned active surface can interact with object protrusions or small convex objects (by enveloping or interlocking) or with object pockets or small concave objects (by interlocking). These interactions facilitate strong grasps under shear load.

3.3.2   Multi-Level Surface Adaptation

The related works presented thus far have mainly involved design and characterization of a *single* adaptive surface that adapts a *single* property (either adhesion, friction, or compliance). Recall from Section 3.2.1 that surface adaptation can take place at three levels of scope: passive, reactive, and active. Multi-level adaptation has adaptive surface elements at more than one level of scope. For instance, a multi-level adaptive surface might include both microtopography with passive effects and an independently controlled active substrate underneath the microtopography.

Advantages of Multi-Level Adaptation

Surfaces with multi-level surface adaptation offer a promising approach to adaptive grip control. On a practical level, the growing availability of commercial and industrial microtopography surfaces facilitates the incorporation of passive elements into existing reactive or active surface adaptation approaches. Access to a variety of different microtopography surfaces also enables a layered adaptive grip surface (like the one presented in this thesis) to swap its "skin" without changing the underlying active control phenomenon, facilitating grip surface customization based on target object properties. Beyond these practical considerations, there may be significant performance benefits: namely, multi-level adaptation facilitates multimodal gripping and may have synergistic effects.

Adaptive grip surfaces can enable different "modes" of gripping. Definitions of such modes vary across different gripper designs, but could include:

- modes targeting different object types (e.g., rough vs. smooth or flat vs. curved)
- modes involving different manipulation behaviours (e.g., grasping vs. in-hand manipulation)
- modes using different adaptive mechanisms (e.g., changing friction coefficient vs. contact area)
- modes that adapt different surface properties entirely (e.g., changing adhesion vs. friction)

Here, *multimodal gripping* is defined as gripping in which surface adaptation, grip behaviour, or their combined effect create distinct modes based on distinct desired grip conditions.

Multi-level surface adaptation with *active* adaptive elements is one way to enable multimodal gripping. Since control of the adaptive surface and control of the overall gripper articulation are independent, grasping modes can be defined using different combinations of surface control states and gripper control states. These independent control axes offer more options compared to a typical gripper without an adaptive surface or with only passive/reactive surface adaptation.
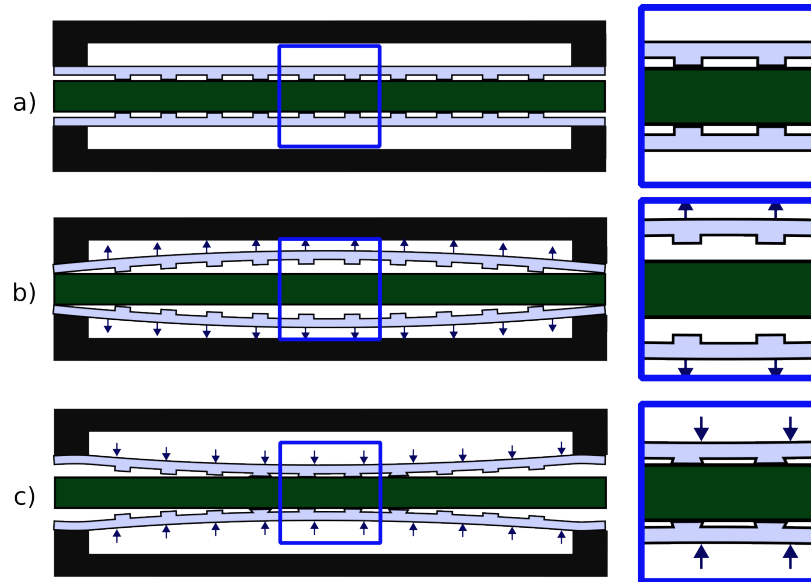
Figure 3.17: Schematic of different gripping modes. An object (dark green) is gripped using a flexible microtopography-covered grip surface (light blue) that is deflected under pressure from a subsurface pneumatic chamber (inside the black structure). a) In neutral mode, the substrate is at rest and microfeatures contact the surface evenly. b) In low-contact mode, the substrate withdraws and fewer microfeatures contact the surface, reducing contact area at the grip interface. c) In high-contact mode, by contrast, the substrate protrudes and applies normal pressure to the object surface. This pressure may deform microfeatures, interlock microfeatures with asperities on the object surface, or compress the substrate into the gaps between the features, potentially increasing contact area.

For example, the adaptive grip surface proposed in this thesis achieves multimodal gripping using pneumatic deflection of a flexible surface with micropatterned actuatable regions. This surface's multi-level adaptation combines passive effects from surface microtopography with active control of the actuatable substrate, giving the surface at least three gripping modes (depicted in Figure 3.17):

1. In neutral mode, the substrate is at rest and a gripped object mainly contacts microtopography.

2. In low-contact mode, the substrate recesses away from a gripped object. In this mode, contact effects from microtopography are significantly reduced, as the gripped object mainly contacts the fixed regions (which have no added microtopography).

3. In high-contact mode, the substrate protrudes to push against a gripped object. In this mode, interactions depend heavily on the specific object shape and topography: small objects may be enveloped by the inflated surface, rough objects may interlock with microtopography, smooth and rigid objects may cause microtopography to deform until the surface substrate contacts the gripped object (causing a global increase in contact area), and so on.

These modes produce very different effects, and using different modes in sequence during a grip process can provide still more control options (e.g., grip can be adjusted upon object slip detection by switching to a high-contact mode as depicted in Figure 1.1).

Parallels between multi-level adaptive surfaces and the hierarchical adaptive surfaces found in nature suggest that multi-level adaptation could have *synergistic* effects. For instance, Song et al. combined the (larger-scale) frictional effect of a claw with the (smaller-scale) dry adhesion of a fibrillar pad to create an adhesive connection that was stronger than the sum of the individual
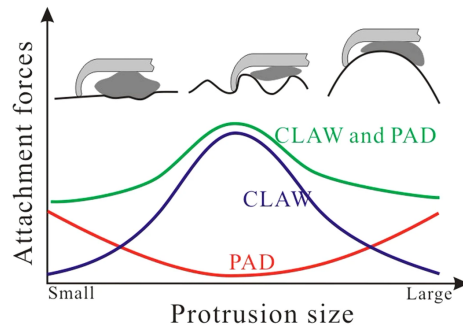
Figure 3.18: Schematic showing the effect of protrusion (asperity) size on the attachment forces of claws and adhesive pads. *Figure and caption adapted from Song et al. [61] under* CC BY 4.0.

adhesive strengths for these two features (shown in Figure 3.18) [61]. They suggest that this synergy stems from the combination of adhesive tactics at different lengthscales. Wang et al. described a similar effect in the remora suckerfish, where they found synergy in the combination of the suction effects of lamella soft tissue (which adhered well to smooth surfaces with smaller-scale asperities) and the frictional effects of rigid spinules (which adhered well to larger-scale asperities) [153].

This synergy between effects at multiple lengthscales could be mimicked in adaptive grip surface design. For instance, a design could aim to synergistically combine the microscale effect of a high-friction microtopography surface with the macroscale effect of actuating the surface substrate.

Multi-Level Adaptive Surfaces in Robotic Gripping

Many adaptive grip surface designs use multi-level adaptation, typically combining passive surface modification with either reactive effects or active surface control. The most common multi-level strategy, often found in designs that use shear-sensitive adhesion, is combining passive microtopography with reactive structures. For instance, Hawkes et al. use microwedge adhesives in a configuration that reactively shears the adhesives away from each other along an object surface, a response driven by the object's weight [154], [155].

Some designs use reactive adhesion to adapt *multiple* surface properties. As a representative example, Ruotolo et al. place microwedge adhesives on a structurally compliant rib structure (shown in Figure 3.19a), strengthening the shear-sensitive adhesive effect of the microwedges using the buckling of the flexible ribs as the gripper closes. A few surfaces adapt multiple properties using multiple active mechanisms (e.g., Xu et al. use active suction, treads covered in dry adhesives, and wheels covered in microspines [156]) although such designs are generally impractically complex.

Other designs adapt the same surface property at multiple levels. For instance, Alizadehyazdi et al. use microwedges for reactive adhesion, then further strengthen the connection using active electroadhesion [157]. The multimodal gripper designed by Hao et al. (and shown previously in Figure 3.3b) uses suction-based adhesion as well as impactive gripping supported by adhesive microwedge surfaces [46].

A less common strategy—and the strategy used in this thesis—is placing passive microtopography on an active substrate. This strategy is often used with active elements (e.g., belt drives [161] or pulley systems [162]) that apply shear load to microwedge adhesives or similar shear-sensitive surfaces. The vacuum-assisted variable-stiffness adhesive soft actuator shown in Figure 3.19c [159]
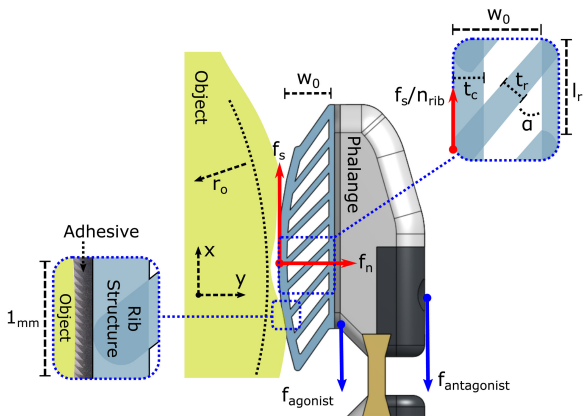
(a) Passive microtopography combined with reactive adaptation. Shear-sensitive features are engaged through load-induced buckling. *Figure and caption adapted from Ruotolo et al. [11] with permission from AAAS.*
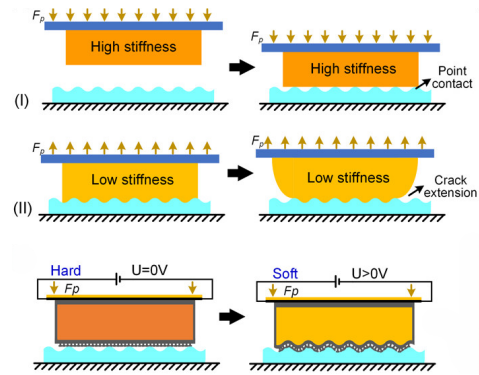
(b) Passive microtopography combined with active adaptation using a stimulus-responsive material. Top: Contacting surfaces with (I) high and (II) low stiffness. Bottom: Actively adapting stiffness. *Copyright 2020 American Chemical Society. Adapted from Li et al. [158] with permission.*
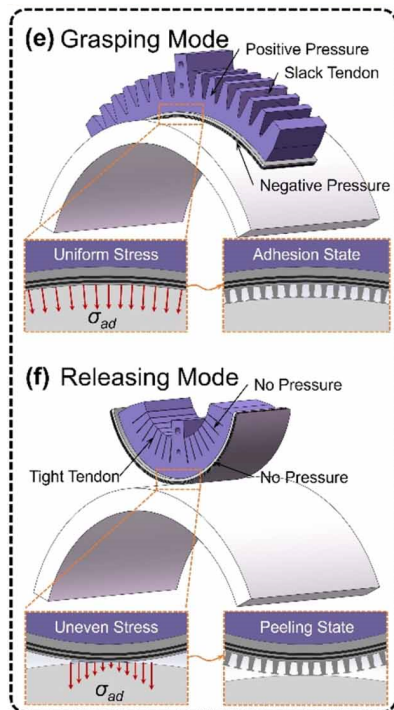
(c) Passive microtopography combined with active adaptation using vacuum-assisted stiffness changes. *Reprinted (adapted) with permission from Sun et al. [159]. Copyright 2023 IOP Publishing.*
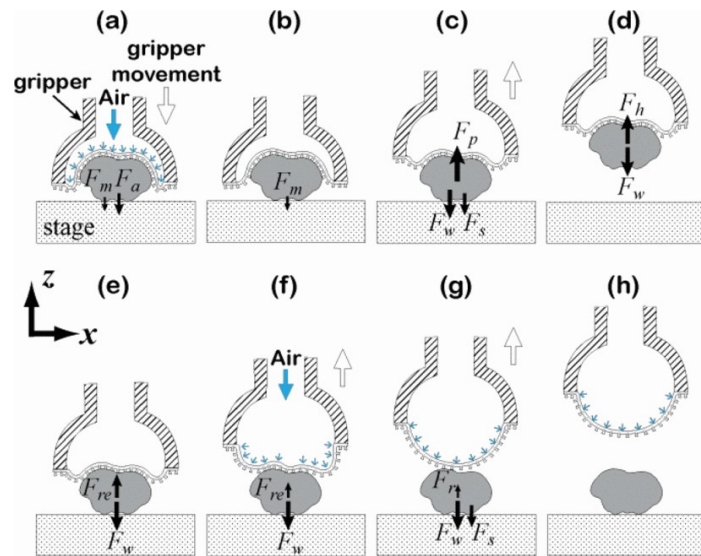
(d) Passive microtopography combined with active adaptation using pneumatic inflation. Pick-and-place process: (a) gripper conforms to part and applies a pneumatic preload, (b) the preload is relaxed and the part is (c) lifted and (d) transported. (e) To place, the part contacts the receiving surface, and (f) the membrane inflates (causing the grip surface to start to peel) as the gripper is lifted until (g) the surface fully peels away and (h) the part is released. *Copyright 2014, IEEE. Adapted from Song et al. [160] with permission.*

Figure 3.19: Various examples of multi-level surface adaptation.

(and the similar design put forward by Chen et al. [163]) presents a particularly interesting use of this strategy, in which an object is gripped by combining microtopography with a material that has a default adhesive state, extension of a pneumatic actuator, and vacuum-based stiffening. To release the gripped object, this gripper contracts the pneumatic actuator and inflates the stiffening chamber to peel the adhesive microtopography. Similarly, various designs from Song et al. inflate a microtopography-covered bladder to press adhesive micropillars against a surface and then deflate the bladder to peel the micropillars (as shown in Figure 3.19d) [160], [164]–[166]. Another common approach is the use of stimulus-responsive materials to conform the variable-stiffness medium under a microtopography-covered substrate to the shape of a gripped object (e.g., by using an electrothermal film to heat and soften thermoplastic polyurethane (as shown in Figure 3.19b) [158]. More generally, microtopography surfaces can be manipulated in a wide variety of ways using shape memory polymers (e.g., using light-responsive tilting of micropillars [167]).
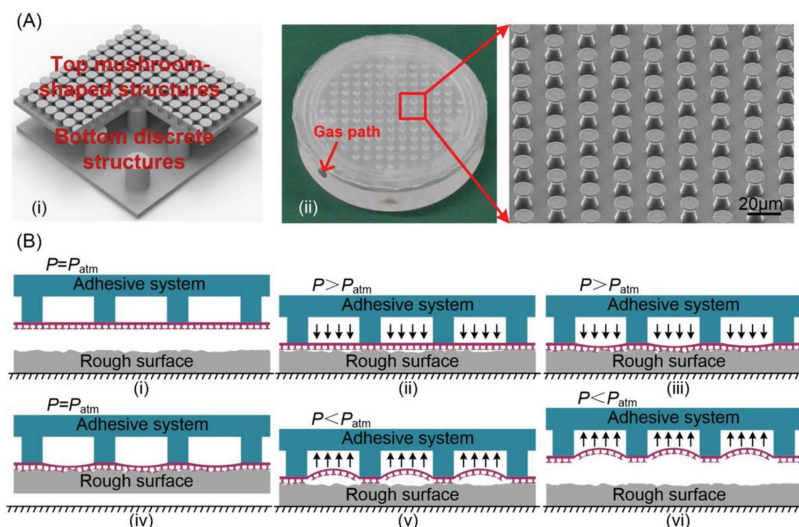
Figure 3.20: Tunable adhesive grip surface with active substrate under gecko-inspired microtopography. A: (i) Sketch and (ii) picture of hierarchical grip surface structure. B: Schematic showing process of attaching and detaching grip surface by varying channel pressure. *Copyright 2019 Wiley. Adapted from Tian et al. [168] with permission.*

The most similar design to that proposed in this thesis is the hierarchical microtopography-based pneumatic gripper designed by Tian et al. (shown in Figure 3.20) [168]. This gripper uses microtopography on an active pneumatically-deflected substrate with excellent adaptive adhesion performance. However, unlike the grip surface discussed in this thesis, the gripper designed by Tian et al. is designed and tested for normal forces alone rather than shear forces, uses adhesion alone to grip rather than tuning friction in support of impactive gripping, and requires a specialized microfabrication process.

3.4 Conclusion

There are now a wide variety of comprehensive reviews examining the impact of microtopography design parameters on adhesion and normal forces (e.g., [53], [56], [77], [169]). However, these adaptive surface design studies are not always applicable to gripping, as most such studies are published

outside of robotics and discuss the design of adaptive surfaces without a specific application. Furthermore, most studies focus on testing adaptive surfaces with normal loading and a target surface that is flat, smooth, and perfectly parallel to the adaptive surface—conditions that are not typical for most robotic gripping. As mentioned in Section 3.2.3, a few studies examine microtopography design for shear loading theoretically (e.g., block and post geometry [90] or film, block, and beam geometry [170]) and/or experimentally (e.g., dimple geometry [85], angled flaps [91], angled pillars [94]), but their conclusions are not necessarily applicable to grip surfaces. Even works that look at microtopography design for robotics specifically (e.g., [52], [171]) typically focus on discussion of fully soft grippers[3], which cannot be easily compared to rigid grippers or hybrid rigid-soft grippers, further limiting the applicability of existing studies.

Although adding surface topography is a common approach to surface adaptation (particularly when modulating adhesion [1], [5], [42], [172]), little attention has been paid to the effects of combining passive surface topography with an active, actuatable surface substrate. Multi-level surface adaptation more often combines surface topography design with *reactive* design features [11], [162] in order to simplify actuation. Of the designs that do combine surface topography with *active* behaviour, almost all appear to use either gecko-inspired micropillars or microwedges [1], [160]. There is thus little information available about the effects of combining other types of microtopography with active substrate control. This gap in the literature is exacerbated by the fact that many works that propose designs for multi-level adaptive grip surfaces only present the details of their final selected design and do not discuss design alternatives. The few works that do explain their design decisions provide very useful information for those looking to create multi-level adaptive grip surfaces — e.g., Mizushima et al. investigate the frictional behaviour of various microtopography types (vertical grooves, horizontal grooves, dot patterns, concentric grooves, and grids of grooves) when gripping in wet, dry, and oily conditions [9], and Liu et al. investigate the impact of varying microwedge size and spacing on grip surface adhesion [173].

The design presented in this thesis is novel in several ways. Unlike other approaches that use inflatable membranes (excepting [149] and [131], which do not fabricate adaptive grip surfaces, and [151], which does not deflate), it uses an array of multiple inflatable active regions to both promote contact splitting and enable investigation of the behaviour of different active region designs. Unlike most other designs that use pneumatic surface deflection (excepting [144] and [146], which are not friction-tuning devices), it uses three surface states (positive, neutral, and negative) rather than only two, and it examines the impact of changing the timing of gripping relative to surface actuation. Unlike most studies of multi-level adaptive grip surfaces, this work compares different microtopography designs, or compares surfaces with microtopography against unpatterned surfaces. Finally, unlike most adaptive surface designs, this design is robust, practical, and inexpensive. The next chapter discusses the design and fabrication of the adaptive grip surface.

---

[3]The recent review by Zhao et al. that discusses adaptive adhesives for rigid-soft grippers [74] is a notable exception.

Chapter 4

Device Design and Fabrication

In this work, assorted adaptive surface devices were designed to explore the impact of various design parameters on surface friction. This chapter summarizes the design and fabrication process.

4.1   Introduction

This section summarizes process objectives as well as the general device structure and behaviour.

4.1.1   Objectives

The design and fabrication process was guided by the following objectives:

- Design should facilitate rigourous comparison. Parameters of interest should be varied systematically so that new candidate surfaces can be compared against others.
- Devices should be fabricated precisely with repeatable results. To this end, digital fabrication methods should be used where possible to improve fabrication precision.
- Fabrication should minimize use of prohibitively expensive or highly specialized resources. Specifically, since these devices are intended to be used in robotic gripping, they should be affordable enough for general use and reasonably easy to repair or replace.

In line with these objectives, devices largely use common materials and digitally fabricated surfaces.

4.1.2   Device Structure

The adaptive surface devices use pneumatic control to locally deflect the grip surface (as depicted in Figure 4.1), thereby tuning friction at the grip interface. Each device consists of three layers:

1. A rigid *control* (base) layer with engraved channels that distributes air from a pneumatic input fitting to the device's internal chamber.
2. An adhesive *structural* (middle) layer that connects the base layer to the top layer with cutouts that define the active regions of the surface by constraining airflow.
3. A thin, flexible *contact* (top) layer that acts as the grip contact surface and is deflected in the active regions by pneumatic pressure in the chamber below.

(P_0)

neutral state $(P_N = P_0)$ deflated state $(P_D < P_0)$ inflated state $(P_I > P_0)$

| P_N | P_N | P_N | | P_D | P_D | P_D | | P_I | P_I | P_I |
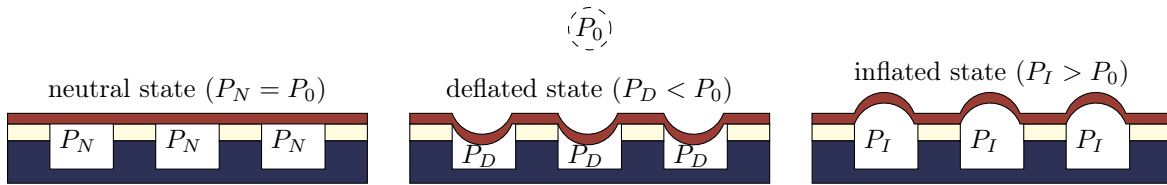
Figure 4.1: Schematic showing the behaviour of the top layer in each actuation state. In the neutral state (left), the top layer is flat. In the deflated state (centre), the top layer is retracted into the pneumatic chamber. In the inflated state (right), the top layer is pushed out from the chamber.

(a) Exploded view of flat device layers.   (b) Exploded view of fingerpad device layers.

(c) Cross-sectional view of model of flat device layers.
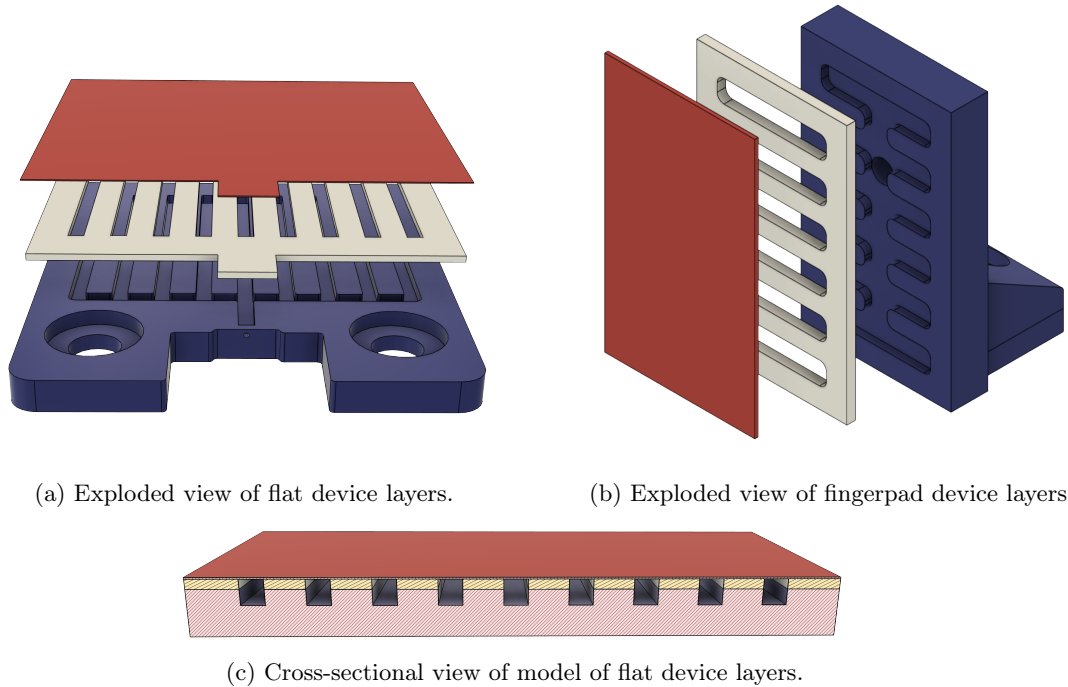
Figure 4.2: CAD models of adaptive surface device top (red), middle (beige), and base (blue) layers.

This layered device structure is based on that of the multilayered pneumatic smart surfaces created in [174][1]. Two form factors are used to fabricate these devices:

1. a wide form factor is used to make *flat* devices. These devices are simple to fabricate and test during surface characterization testing (Chapter 6) because their relatively large area and mounting holes facilitate attachment to the shear test platform.

2. a narrow form factor is used to make *fingerpad* devices. These devices replace the fingerpads of the gripper used during gripper testing (Chapter 7).

CAD (computer-aided design) models of the two form factors and their layers are shown in Figure 4.2. Although the two form factors differ in appearance, their fabrication processes are similar, and so the information presented in this chapter applies to both form factors unless otherwise specified. Candidate surface designs are initially implemented and tested as flat devices, and then those designs that prove effective are implemented as fingerpad devices.

---

[1]The cited thesis was written by a former student in the Bio-Inspired Materials and Design Laboratory.

4.1.3   High-Level Adaptation Behaviour

Surface adaptation is controlled by deflecting the active regions of a device's flexible top surface using the sub-surface pneumatic chamber. A device has three general actuation states, which are defined by the pressure inside the device's pneumatic chamber relative to atmospheric pressure (P_0):

1. In the *neutral* state, internal pressure $P_N = P_0$ and the top surface is flat across the active regions (coplanar with the contact plane) as pictured in Figure 4.3a.

2. In the *deflated* state, internal pressure $P_D < P_0$ and the top surface deflects down in the active regions (toward the pneumatic chamber, below the contact plane) as pictured in Figure 4.3b.

3. In the *inflated* state, internal pressure $P_I > P_0$ and the top surface deflects up in the active regions (away from the pneumatic chamber) as pictured in Figure 4.3c. In this state, since the active region surface is higher than the inactive region surface relative to the device base, the contact plane is defined by the protruding active regions.

These actuation states are represented in the schematic in Figure 4.1. The exact pressure levels applied for each actuation state vary depending on the elastic modulus of the top layer, the geometry of the active regions, and the desired changes in frictional properties.

(a) Neutral at 0 kPa.   (b) Deflated at -40 kPa.   (c) Inflated at 40 kPa.
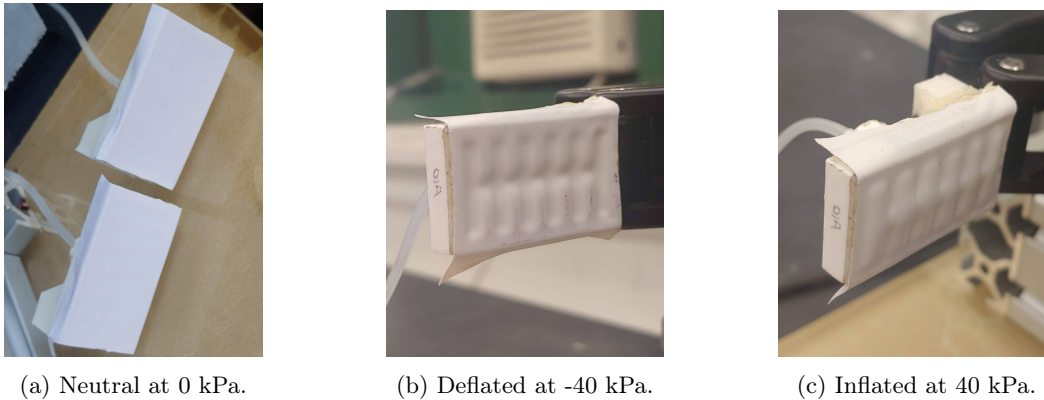
Figure 4.3: Pictures of adaptive fingerpad devices in different actuation states.

4.2   Device Design

This section summarizes the adaptive surface design process. Fabrication is discussed in Section 4.3.

4.2.1   Overview

Adaptive surfaces are designed for contact modulation. Accordingly, the focus of their design is on their top layer, which acts as the contact surface during gripping. The key design parameters (summarized in Figure 4.4) relate to the top layer substrate, the top layer microtopography (or lack thereof), and the middle layer cutouts that determine the active regions of the surface.

The surface adaptation behaviour is defined by the method of surface actuation, so the actuation method was one of the first major design decisions. Pneumatic control was selected as the actuation approach because of its simplicity and availability. Other fluid actuation methods (e.g., hydraulics)
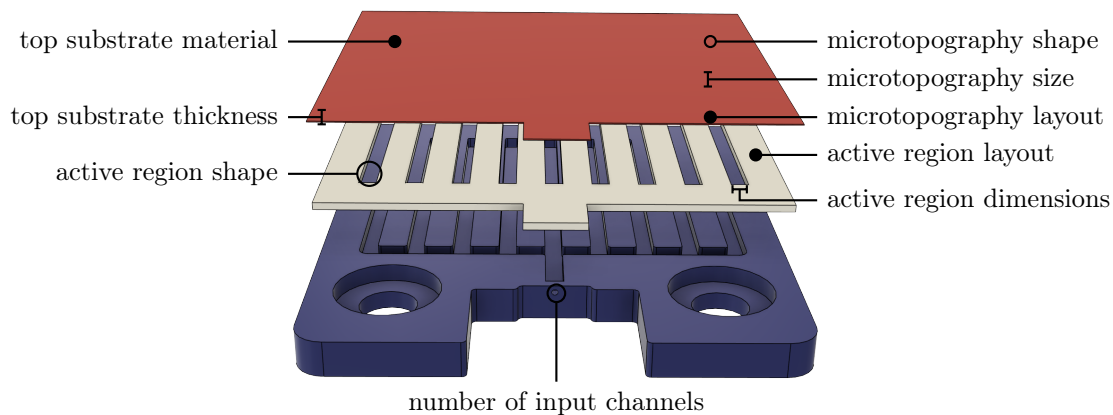
Figure 4.4: Key design parameters for specification of an adaptive surface.

could cause spills or other hazards if tubing or connections fail. Non-fluid-based approaches (like the use of shape memory materials or materials that respond to inputs like light and heat) require expensive and uncommon equipment or place constraints on the operating environment. In contrast, pneumatic control is used widely in industry in both rigid and soft robotics. Even for applications where existing pneumatic control is not available, the simple pneumatic control required for these devices can be set up relatively quickly and inexpensively. However, pneumatic control does have some drawbacks, namely, vulnerability to punctures/air leakage and poor energy efficiency. Choosing robust top surfaces helps to reduce the risk of punctures.

Keeping both practical considerations and the design and fabrication objectives (Section 4.1.1) in mind, other major design decisions followed this same approach of choosing the simplest and most readily available option wherever possible. For instance, both the middle and base layers of the device use common prototyping materials.

The overarching goal of designing the active contact (top) layer determines the design of the structural (middle) and control (base) layers. Consequently, the contact layer is always specified first, followed by the structural layer and then by the base layer.

4.2.2 Contact Layer

Both commercially available and custom surfaces are used as device contact (top) layers. The substrate materials (and their microtopography, where applicable) are described in Table 4.1. The microtopography surfaces used during surface characterization are pictured in Figure 4.5.

The contact surface substrate must be strong enough to resist tearing under shear load and flexible enough to deflect in response to relatively light pneumatic pressure. The substrate can also be extensible, although surface stretching can complicate analysis and reduces the repeatability of surface behaviour. The substrate materials tested in this work range in stiffness: the surfaces printed with elastic resin have low stiffness while the commercially available tapes and sandpaper have considerably higher stiffness. The substrate's thickness and stiffness determine its bending properties, which in turn determine the minimum lengthscale for active regions.

Table 4.1: Materials used or created for adaptive surface device contact layers. All dimensions are given in mm. MYFab is the Myhal Centre Fabrication Facility. Printed surfaces are made with FormLabs® Elastic 50A Resin V1 in a FormLabs® SLA printer.

Substrate Type	Source	Thickness	Features	Feature Height
Trizact™ Hookit 268XA sandpaper	3M™	0.08	pyramids	0.47
PTFE tape	Unknown	0.21	N/A	N/A
PVC tape	Tapebear	0.16	N/A	N/A
Custom printed short ridges, flat device	MYFab	0.5	ridges	0.4
Custom printed long ridges, flat device	MYFab	0.5	ridges	0.4
Custom printed sawtooth ridges, fingerpad	MYFab	0.5	sawteeth	0.2
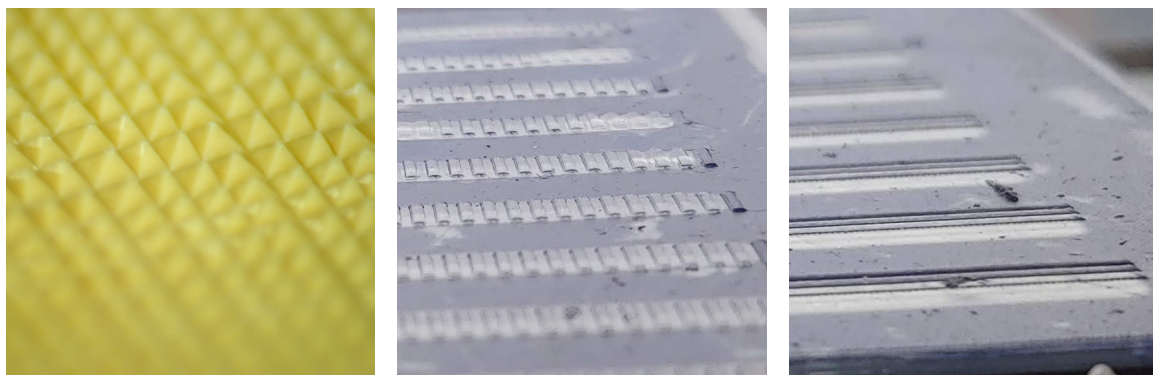
(a) Trizact™ sandpaper.   (b) Custom-printed short ridges.   (c) Custom-printed long ridges.

Figure 4.5: Examples of microtopography used in adaptive surface devices. Note that these images are not taken at the same scale. All pictured microtopography features are 0.4-0.5 mm in height.

Surface microtopography is a rich design space with a great deal of application-specific design options. While microtopography design in general has been discussed in Section 3.2.3, a few particularly relevant parameters altered in this work are discussed below:

- The stock material used to fabricate microtopography features can drastically alter the effective stiffness of a microtopography surface. Materials used in device design vary from very hard (aluminum oxide) to very soft (elastic resin).

- Feature shape impacts the behaviour of microtopography under load. Shapes used in device design include micropyramid arrays and microridge rows.

- Feature size relative to the size of asperities in a contacting surface affects frictional interactions. Sizes used in device design range between 200 and 500 microns.

- Microtopography layout determines the locations and coverage of microtopography features on a patterned surface. Commercially available surfaces used in device design place microtopography features in arrays across the entire surfaces, whereas custom printed surfaces place microtopography features in rows across the active regions only.

While all of these parameters impact surface adaptation, layout is a particularly impactful parameter in the context of active adaptive surfaces. The layout of microtopography relative to active regions determines how the microtopography affects contact properties in different surface actuation states. If the surface is entirely covered with microtopography features, an object will contact some features

in all states. If only the active regions are covered with microtopography features, then an object will likely not contact the features when the surface is in the deflated state. The friction-tuning behaviour of an adaptive surface should therefore show a greater difference between the neutral and deflated states if the microtopography coverage is limited to the active regions.

4.2.3   Structural Layer and Control Layer

The structural (middle) and control (base) layers control airflow from a pneumatic inlet to the contact layer, enabling actuation of the contact layer in defined active regions. In this work, commercially available materials are used for the structural and control layers to facilitate fast and simple fabrication. These materials are described in Table 4.2.

Table 4.2: Materials used for adaptive surface device structural and control layers. MYFab is the Myhal Centre Fabrication Facility.

Layer	Description	Source	Thickness
Structural	3M VHB (unknown version, white)	McMaster-Carr	0.127 mm
Structural	3M VHB 5906 (black)	McMaster-Carr	0.13 mm
Control	Extruded acrylic	MYFab	6 mm

Once the contact layer has been designed, the structural layer can be designed by specifying the dimensions and shapes of the cutouts that create active regions. All of the adaptive surfaces discussed in this work use rectangular active regions. For each new adaptive surface design, the contact layer is subjected to pneumatic pressure with varying candidate active region widths. Active region widths for which the contact layer visibly deflects are selected for the final surface design. For gripper fingerpad devices, the orientation of the active regions relative to the gripper is also determined. For flat devices, the orientation of active regions is not relevant since these devices are tested in multiple orientations. The different active geometry configurations used are shown in Table 4.3.

Table 4.3: Active region dimensions and layouts used for adaptive surface devices.

Base type	Shape	Width	Length	Separation	Count	Orientation
Flat	Rectangle	5 mm	52.5 mm	10 mm	5	N/A
Flat	Rectangle	3 mm	51.5 mm	5 mm	9	N/A
Flat	Rectangle	2 mm	53 mm	6 mm	9	N/A
Fingerpad	Rectangle	3.25 mm	16 mm	2.5 mm	6	Perpendicular

Once the structural layer has been designed, the engraved pneumatic channels in the control layer can be designed such that the channel widths match the active region widths. The control layer channels are laid out in a fork structure. An inlet channel leads into the device from the pneumatic inlet to a long connecting channel. From this connecting channel, various "tine" channels branch out, with one channel for each active region or column of active regions. This fork structure is visible (with and without the structural layer added) in Figure 4.6. Multiple inlets can be used to obtain multiple controllable pneumatic channel sets (provided that the channels do not connect to one another). In this work, however, all bases have only a single inlet.

Two very different base form factors are used with structural and control layer dimensions as shown in Table 4.4. The flat base is designed for ease of testing. Since testing involves mounting
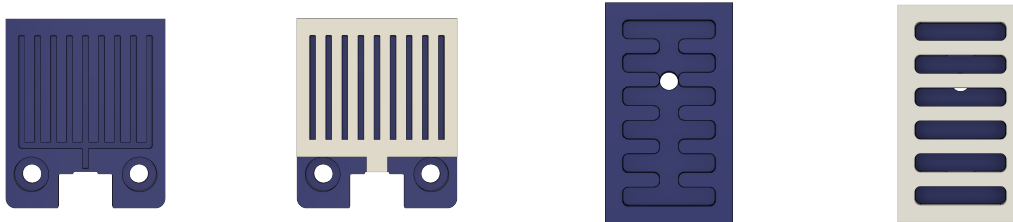
(a) Control layer alone for flat device.

(b) Structural layer added for flat device.

(c) Control layer alone for fingerpad device.

(d) Structural layer added for fingerpad device.

Figure 4.6: For both device form factors, the engraved pneumatic channels in the control layer are designed to match the widths of the active region cutouts in the structural layer.

the base to a flat testing platform, the inlet for this form factor connects to the side of the base to avoid interfering with mounting. Conversely, the fingerpad base is designed to replicate a stock Robotiq 2F-85 gripper fingerpad so that the stock fingerpads can easily be replaced with adaptive fingerpads. Since the back of the fingerpad is the surface that is the least likely to interfere with gripping, the inlet for the fingerpad form factor is placed at the back of the fingerpad.

Table 4.4: Dimensions of control (base) and structural (middle) layer for each form factor.

Base type	Control layer dimensions [mm]	Structural layer dimensions [mm]
Flat	95×80	70×80
Fingerpad	22×38	22×38

4.3 Device Fabrication

This section summarizes the fabrication process for an adaptive surface device.

4.3.1 Overview

Keeping both practical considerations and the design and fabrication objectives (Section 4.1.1) in mind, most adaptive surface device components are fabricated using CAM (computer-aided manufacturing) processes. Major tools and equipment used during fabrication are listed in Table 4.5.

Table 4.5: Tools and equipment used to fabricate adaptive surface devices. MB219 is part of the Bio-Inspired Materials and Design Laboratory space, MYFab is the Myhal Centre Fabrication Facility, and MC78 is the Department of Mechanical and Industrial Engineering machine shop.

Type	Make	Location	Purpose
3-axis CNC	Othermill V2	MB219	Mill flat device bases
5-axis CNC	Pocket NC V2-10	MYFab	Mill fingerpad bases
SLA printer	FormLabs® Form 2	MYFab	Print custom top surfaces
Laser cutter	Universal Laser Systems VLS4.75	MC78	Cut middle layers

(a) Printed surface, with supports.   (b) Printed surfaces, no supports.   (c) Fingerpad with printed surface.

Figure 4.7: Resin-printed adaptive fingerpad surfaces.

4.3.2   Contact Layer

Where commercially available surfaces are used for the contact layer, the only fabrication step required is cutting a piece of the surface to size. Where custom surfaces are fabricated, additive manufacturing (3D printing) methods are used.

Printed microtopography surfaces are designed in 3D CAD in Autodesk Fusion 360. The resulting STL objects are then submitted to the Myhal Centre Fabrication Facility resin (stereolithography, often abbreviated SLA) printing service for fabrication. Initially, the surfaces were printed using supports (shown in Figure 4.7a); however, the small imperfections after support removal affected the seal between the top layer and the middle layer. Fortunately, since the layers are flat-based, they can be printed directly on the print bed, thus avoiding the use of supports and yielding smooth device surfaces (shown in Figure 4.7b).

4.3.3   Structural Layer

The fabrication process for the structural (middle) layer is simple. The outer dimensions of the layer and the active region edges are modelled as a 2D CAD drawing in AutoCAD. This geometry is then used to laser cut the structural layer from sheets of VHB™ tape as shown in Figure 4.8a.

4.3.4   Control Layer

The control (base) layer fabrication process involves multiple steps: laser cutting the stock piece outline, generating engraving toolpaths in 3D CAD/CAM software, engraving channels into the stock piece, and drilling a hole through which to attach the inlet piece.

To simplify fabrication, base layer stock pieces are fabricated in batches using the Myhal Centre Fabrication Facility laser cutting service. This workflow allows the base outline to be cut easily and inexpensively, but also limits the base material to extruded acrylic (the only non-porous material available through this service). A prepared stock piece is shown in Figure 4.8b.

Once the stock pieces have been prepared, computer numerically controlled (CNC) machining is used to engrave the pneumatic channels. Two different CNC milling machines are used: a lower-
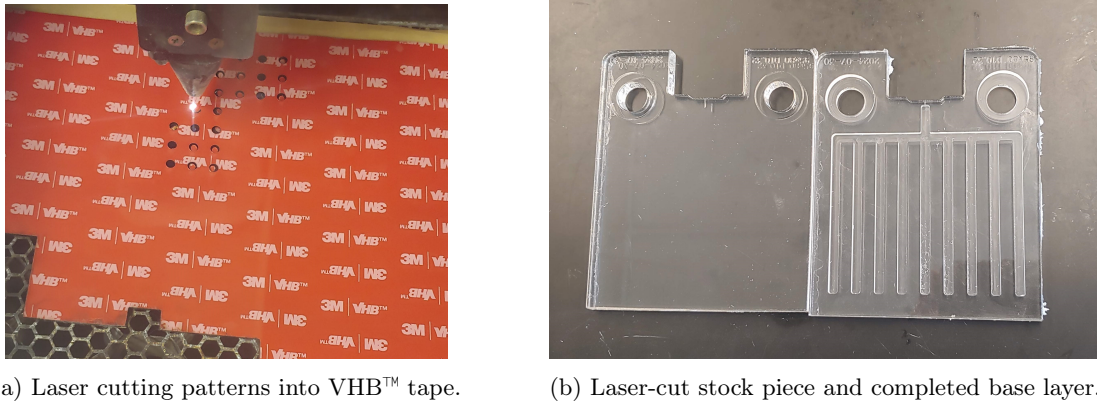
(a) Laser cutting patterns into VHB™ tape.   (b) Laser-cut stock piece and completed base layer.

Figure 4.8: Adaptive surface device components fabricated using laser cutting.

precision 3-axis machine for the flat bases and a higher-precision 5-axis machine for the fingerpad bases, which are smaller and require more carefully positioned toolpaths. Ideally, single-flute endmill tools should be used when milling acrylic because of their superior chip evacuation properties. However, single-flute endmills are expensive and comparatively uncommon, particularly for the small tool diameters used when cutting millimetre-scale channels. For the 3-axis machine, only double-flute endmills are currently available.

Flat base layers are milled using pocket toolpaths with double-flute endmills in the 3-axis machine. Including setup and cleanup, fabrication of a single flat base typically takes around 90 minutes due to the small stepdowns used with a double-flute endmill for acrylic. Fingerpad base layers are milled using pocket toolpaths with single-flute endmills in the 5-axis machine. Including setup and cleanup, fabrication of a single base typically takes around 45 minutes, of which around 5 minutes are required for the actual machining. Sample toolpaths and engraved bases are shown for both base form factors in Figure 4.9.

The final stage in base layer fabrication is the drilling of the inlet hole. For the fingerpad base, the hole is drilled during machining using a bore toolpath. For the flat base, the hole is instead drilled by hand because of the limited workspace of the 3-axis machine.

4.3.5   Device Assembly

Devices are assembled using two operations. First, epoxy is used to attach the pneumatic inlet fitting (and, for fingerpad devices, also the fingerpad mounting base) to the base layer. Second, the middle and top layers are attached to the base layer.

In line with the fabrication objective of using common and inexpensive parts, luer lock fittings are used to connect the device base to inlet tubing. Although luer fittings are not completely airtight, the pneumatic control apparatus is used to supply air on demand, meaning that slight leakage does not pose an issue. For both the flat and fingerpad devices, luer fittings are pressed into the hole in the device base layer and secured and sealed with two-part epoxy. In some cases (especially for the flat device base, for which the machining process is less precise), slight gaps in the applied epoxy layer can cause major air leakage at the fitting connection point. When air leakage is observed, gaps and holes are filled with a second coat of epoxy.
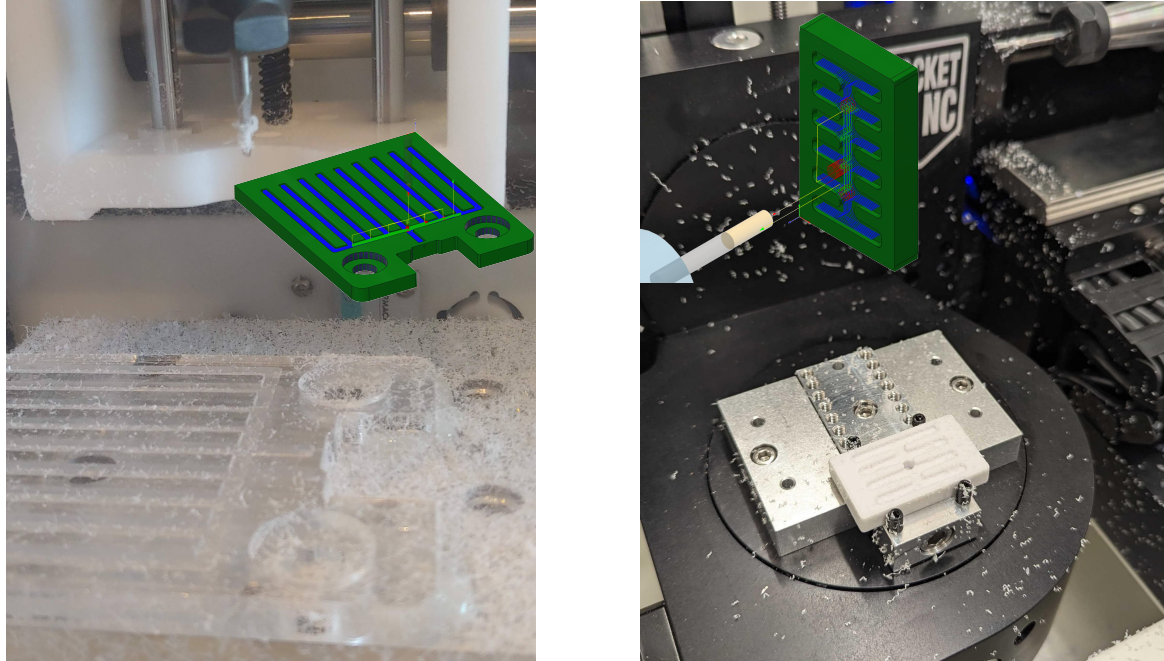
(a) Flat base after 3-axis CNC milling.

(b) Fingerpad base after 5-axis CNC milling.

Figure 4.9: Result of base milling process for each form factor. Insets: simulated CAM toolpaths.

For the fingerpad devices, the epoxy used to attach the luer fitting is also used to secure a 3D-printed mounting piece to the back of the fingerpad (shown as black and white pieces at the backs of the fingerpad bases in Figure 4.10).
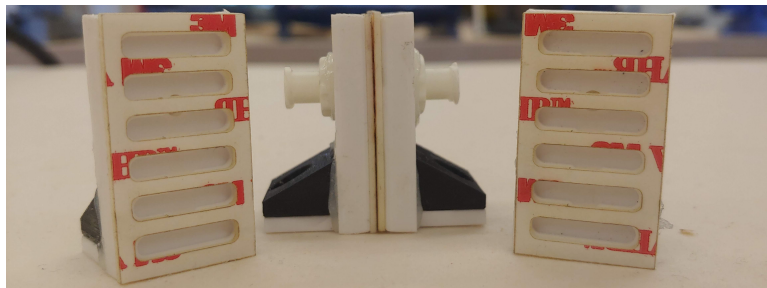
Figure 4.10: Several partially assembled fingerpads with middle layers connected to base layers.

To complete the fabrication process, the layers are assembled. First, the middle and base layers are attached as shown in Figure 4.10. The top layer is then carefully aligned with and attached to the middle layer. Finally, firm pressure is applied to the assembly to help ensure a strong adhesive connection. As can be seen from Figure 4.11, the fully assembled devices are not much thicker than their base layers, with only a slight increase in thickness added by the top and middle layers.

Connecting and using the adaptive surface devices is simple. A device must be mounted to the test platform (for flat devices) or gripper (for fingerpads), but this mounting process takes no more than a few minutes to complete. The device must also be connected to the pneumatic control

(a) Top view.   (b) Angled view.   (c) View from inlet side.
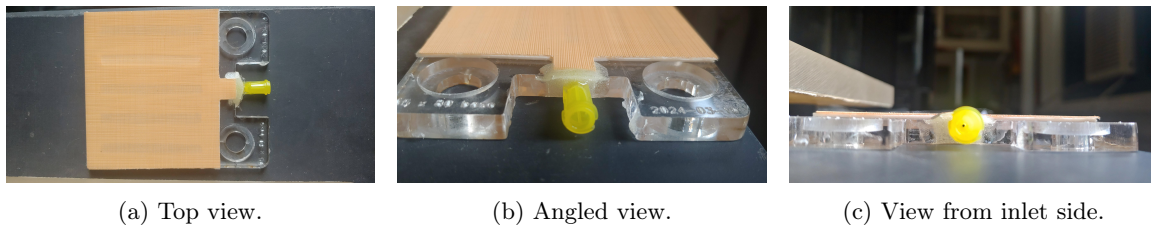
Figure 4.11: Sample fully assembled device (with Trizact™ sandpaper as the top layer).

apparatus (discussed in Chapter 5) by twisting its inlet fitting together with the mating luer fitting at the end of the pneumatic controller outlet tube.

4.4   Device Characteristics

In accordance with the objectives in Section 4.1.1, the adaptive surface device fabrication process uses common and commercially available materials, uses standard fabrication facility equipment rather than specialized tools, and enables comparison between design parameters. The fabrication process can be readily adapted to different equipment or material choices—for instance, the middle layers could be cut by hand, or the base layers could be 3D-printed rather than milled. Moreover, the total material cost per fingerpad device (tabulated in Table 4.6) is less than 1 CAD.

Given the convenience and speed of fabricating microtopography surfaces using a resin printer, devices can easily be manufactured in sets to compare the impact of changes in microtopography size and shape. For instance, a sample set of two flat devices involving printed ridges of differing length and orientation is characterized in Chapter 6. Making repeated parts is particularly fast—setting up and verifying CAD-CAM files takes time, but once a device design has been verified, the same design and fabrication files can be used repeatedly.

A major strength of this design is the separation of roles between the layers: the base layer provides both pneumatic inputs and rigidity, the middle layer defines active regions, and the top layer acts as a contact surface. Each individual layer can be easily customized or replaced with only minimal changes to other layers. For instance, the soft top and middle layers of the fingerpads wear out more quickly than the rigid base layer, but repair is simple and fast—the top two layers can be peeled off and replaced in a matter of seconds.

The adaptive surface devices are designed to be suitable for shear loading. Using a combination of rigid base materials and strong adhesive middle layers makes the devices robust to repeated use— many devices maintain their function for dozens or hundreds of (sometimes high-force) shear tests before failing. When devices fail, the most common failure mode is air escape due to delamination.

Table 4.6: Materials cost for sample adaptive fingerpad device with PVC tape used as contact layer.

Layer	Cost
Base (extruded acrylic)	CAD 0.10
Middle (3M™ VHB™)	CAD 0.46
Top (PVC tape)	CAD 0.01
Total	CAD 0.57

Under high pneumatic pressures and shear loads, the layers on some devices eventually separate, allowing air to escape from between the top and middle layers or from between the middle and bottom layers. This is a particular problem for the printed surfaces, which tend to leak more quickly and more often due to poor layer adhesion. Sample delaminated devices are shown in Figure 4.12.

Delamination most frequently occurs near the inlet or near the branching area of the fork pattern in the base layer. The delamination issue could potentially be addressed by using a stronger adhesive for the midlayer, by subjecting the assembly to heat or pressure while adhering layers, or by adding a rigid supporting layer between the middle layer and base layer.
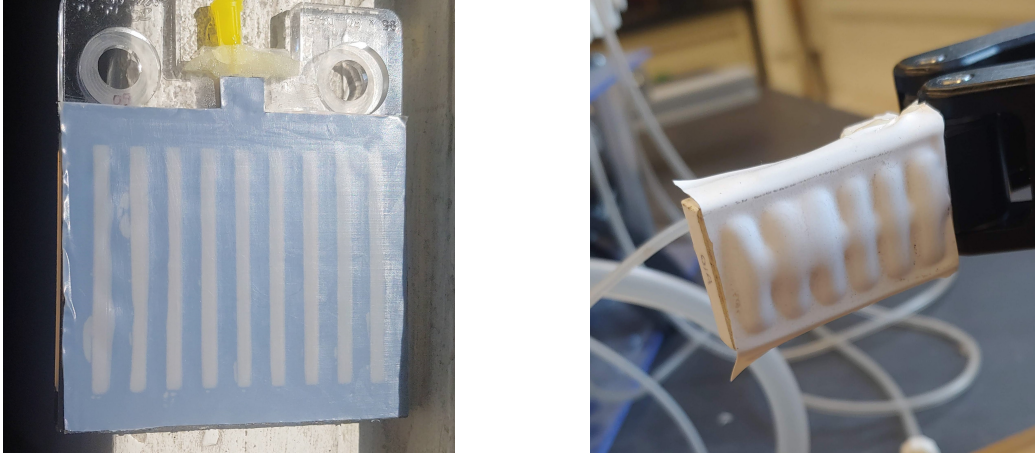
(a) Worn-out flat device with delamination surrounding active regions and torn top layer edges.

(b) Worn-out fingerpads with delamination leading to poorly defined inflated active regions.

Figure 4.12: End-of-life adaptive surface devices.

Also, the current method of attaching the fingerpad mounting piece to the base of the fingerpad is imprecise, leading to some asymmetry and misalignment (visible in Figure 4.13) between pairs of fingerpads. This issue could be solved by fabricating the mounting piece and fingerpad base as a single unit, or by using a jig during epoxy application.

Figure 4.13: Gripper with one adaptive fingerpad and one stock fingerpad. Fingerpad edges are misaligned because of uneven adhesive application between the adaptive fingerpad and its mount.

Chapter 5

Experimental Methodology

The adaptive surface devices described in Chapter 4 were designed to tune surface friction. This chapter summarizes the methods used to conduct shear force tests in order to characterize the friction-tuning capabilities of these devices. The pneumatic controller used to actuate devices is described in Section 5.1 (with additional information in Appendix B) and the force tester used to conduct shear force tests involving actuated devices is described in Section 5.2 (with additional information in Appendix C).

5.1 Pneumatic Control

This section provides a summary of the pneumatic control apparatus and control procedures used to actuate adaptive surface devices. Wherever a "pressure level" is mentioned, the value referenced is the *relative* pressure difference between a pneumatic channel and the environment.

The pneumatic control system has two core objectives: pressure regulation and pressure switching. Pressure regulation is the task of maintaining the pressure inside a device at a set and steady level. The pneumatic system is a closed-loop control system wherein a pressure sensor reads the current pressure in the pneumatic channel that connects to each air reservoir (the *input* channel). If the pressure sensed in an input channel is too low or too high, the control system runs a pump to move air into or out of the channel. This control loop is depicted in Figure 5.1. Once the input channel pressure is regulated appropriately, a *common* channel is used to connect the input channel to an *output* channel that supplies air to an adaptive surface device.
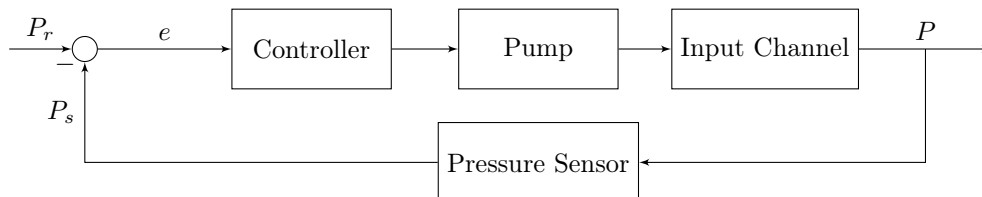

Figure 5.1: Block diagram for high-level pneumatic regulation process.

Pressure switching is the task of changing the pressure inside the pneumatic chambers of the device from the current pressure level to a new setpoint level. The pneumatic controller can pressurize its channels to levels between -100 kPa and +100 kPa. In practice, however, pressure switching

typically involves changes between three general states: neutral, inflated, and deflated (which were previously shown schematically in Figure 4.1 and pictured on real devices in Figure 4.3). The experiments discussed in Chapter 6 and Chapter 7 use -40 kPa as the deflated level, 0 kPa as the neutral level, and +40 kPa as the inflated level.

5.1.1 Control Apparatus

The multi-channel apparatus used in this work was designed by Kurtis Laqua, a former student in the Bio-Inspired Materials and Design Laboratory, and described previously in [174].

The multi-channel apparatus can be used with up to eight independent pneumatic outputs. It uses two reservoirs, one designated for positive pressure levels relative to atmospheric pressure and one designated for negative pressure levels. These reservoirs can be used to store pressurized air and connect to outputs on demand. The volume of the pneumatic channels (both in the apparatus and in the output device) is small relative to the volume of the reservoirs. Once a pneumatic channel is connected to a reservoir, the pressure in the channel will quickly converge to the pressure level of the reservoir, enabling rapid pressure switching.

Function of Common Channel

The multi-channel apparatus uses three input channels, where:

- the positive channel is connected to the positive reservoir as well as a pump that is configured to pump air into the positive reservoir,
- the negative channel is connected to the negative reservoir as well as a pump that is configured to pump air out of the negative reservoir, and
- the neutral channel is open to the atmosphere.

The three input channels are connected to a common channel via solenoid valves. The pressure level in the common channel is controlled by opening one of the input channel valves, thereby connecting the input channel to the common channel. The specific input valve to open is chosen based on the difference between the current pressure level in the common channel and the desired pressure level.

The common channel is also connected to the system's eight outputs via eight additional solenoid valves. Just as the input channel connections are used to set the pressure of the common channel, the common channel can be used to set the pressure of the output channels. The general approach to pneumatic control is to use the input channels to set the pressure of the common channel to the desired output level, and then open the valve between the common channel and the target output channel(s). The common channel acts as an intermediate to protect the output devices from large pressure changes and enable simple multi-channel output.

Controllable States

The pneumatic pumps have two valid states: `on` and `off`. If the pressure inside an input channel is above (for the negative channel) or below (for the positive channel) the current pressure setpoint, the corresponding pump turns on and runs until the input channel pressure has passed the setpoint value.
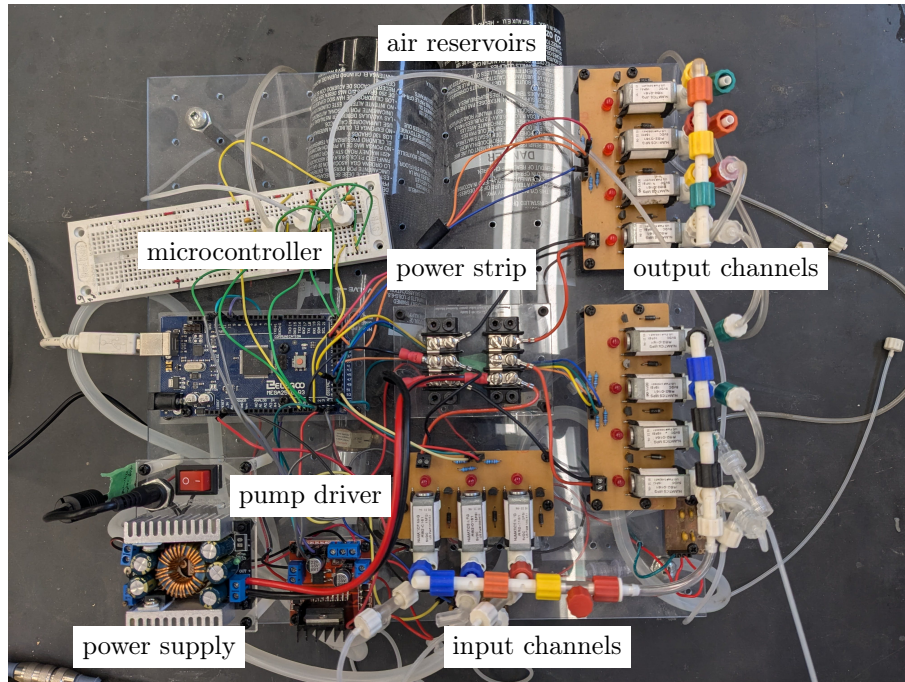
Figure 5.2: Pneumatic control apparatus with major components labelled.

Similarly, the solenoid valves that separate the input and output channels from the common channel have two states: `open` and `closed`. If the valve associated with an input or output channel is open, then that channel is connected to the common channel. If the valve associated with an input or output channel is closed, then that channel is isolated from the common channel.

Apparatus Components

The multi-channel pneumatics apparatus (pictured in Figure 5.2) is controlled by an ATmega2560 microcontroller (on an ELEGOO Mega 2560 microcontroller board). Channels take the form of tubing connected together by 5V solenoid valves (between channels) and luer fittings (within channel components). The reservoirs are inexpensive air tanks, and the 12V air pumps are driven by inexpensive L298N motor drivers. A 12V input supplies the pumps and is stepped down to 5V (distributed via a power strip in the form of a screw terminal barrier block) to supply the solenoid valves. The positive and negative input channels each carry an active pressure sensor, for which power is supplied by the microcontroller 5V output.

5.1.2   Control Procedures

This section provides an overview of the procedures involved in pneumatic control.

Connecting Devices

All output channel tubes terminate in female luer lock fittings to facilitate connection with the male luer lock fittings on the adaptive surface devices. A device can be connected to an output channel by twisting the output fitting onto the device fitting as in Figure 5.3.
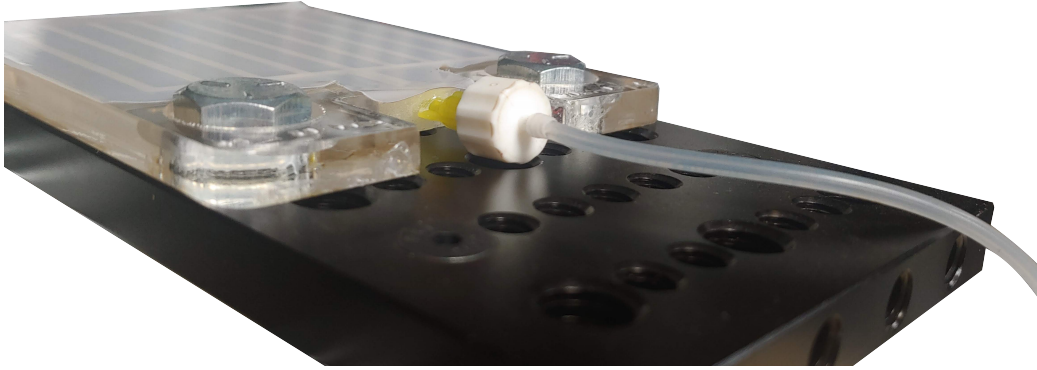
Figure 5.3: Flat active surface device with a pneumatic control apparatus output tube connected to its input via a luer lock fitting.

Regulating and Switching Device Pressure

The microcontroller in the pneumatic control apparatus runs a continuous regulation routine wherein it runs pumps as needed to maintain input channel pressure levels at the current setpoints. To switch the pressure in the common channel, the microcontroller must be given specific commands (i.e., commands to change setpoints or connect input/output channels to the common channel). Similarly, to connect/disconnect output device(s), the microcontroller must be given a specific command indicating which output valve(s) to open or close. Command codes are sent to the microcontroller over serial, either from within a larger test program or directly from the Arduino IDE. More information about the regulation and switching procedures (including flowcharts showing the associated code logic) is available in Appendix B.

5.2   Shear Force Testing

This section describes the methods used for shear testing of adaptive surface devices. The apparatus and methods presented here were used for testing of both flat devices (Chapter 6) and gripper finger-pads (Chapter 7). Some gripper experiments did not use the standard shear testing process; methods for those experiments are presented along with the experiment results throughout Chapter 7.

5.2.1   Test Apparatus

The shear force tester moves a force gauge linearly relative to a fixed platform. The force gauge is attached to a carriage which travels back and forth along a linear actuator. The force gauge is typically connected to a target load on the test platform and records the force required to pull this load. The force testing platform can be divided into three main subsystems:

1. Actuation subsystem
2. Force gauge subsystem
3. Test platform subsystem

Components for all three subsystems are mounted onto each other or onto the solid acrylic base of the tester excepting the motor driver, motor controller, and power/communication cables).
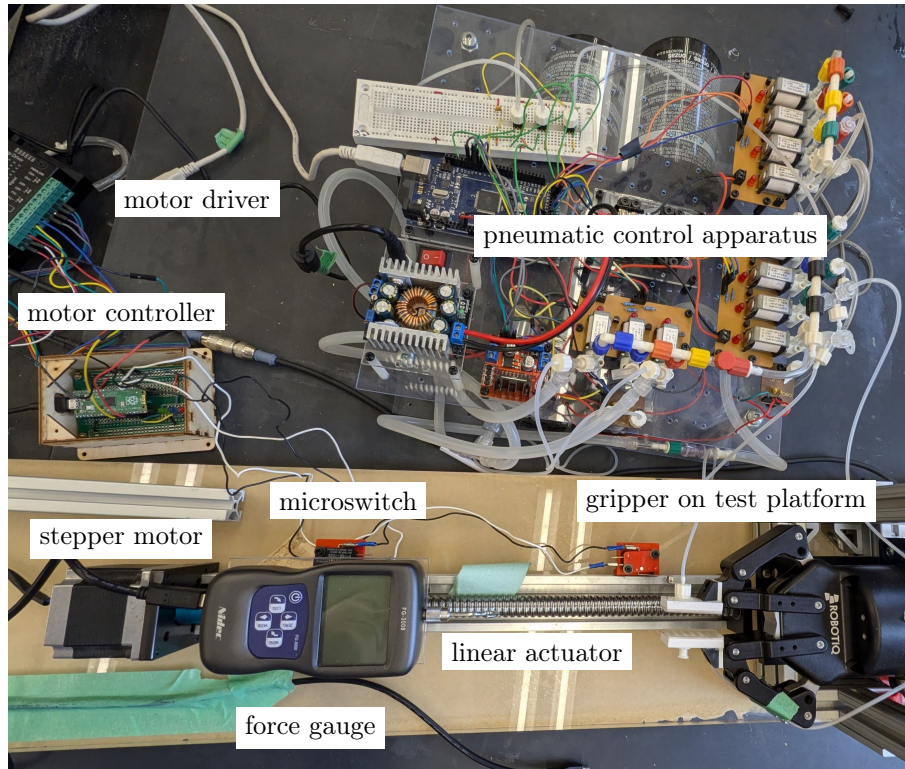
Figure 5.4: Overall experimental setup with major components and equipment labelled.

Force Gauge Subsystem

The force gauge subsystem is the simplest and consists only of the force gauge itself as well as the data cable that connects it to a computer for serial communication. Two different force gauges were used (pictured in Figure 5.5). The lower-capacity Mark-10 Series 4 force gauge (model M4-5) was mainly used for shear testing of flat devices, whereas the higher friction encountered during gripper testing necessitated use of the higher-capacity Shimpo Series FG-3000 force gauge (model FG-3008). The force gauges were used in the same manner, so this section will just refer to "the force gauge".

The force gauge measures force applied to its loading shaft in either tension or compression. The force gauge comes with several different attachments that can be threaded onto the loading shaft. Shear force tests use the hook attachment since it facilitates easy connections to target loads.

The gauge is mounted onto the linear actuator carriage (part of the actuation subsystem) via a custom laser cut plate through which bolts are attached to both the mounting holes in the back of the gauge and the mounting holes in the carriage. During force tests, the gauge shaft is connected to a target load via a wire.

Actuation Subsystem

This subsystem contains the bulk of the electromechanical components in the tester. Components include a linear actuator and carriage, a stepper motor, a motor driver, a custom motor controller circuit based on a Raspberry Pi Pico microcontroller board, two microswitches, and various support pieces and mounts.

Figure 5.5: The two force gauges used in shear testing. The Mark-10 M4-5 gauge (top) has a capacity of 25 N with a resolution of 0.01 N. The Shimpo FG-3008 gauge (bottom) has a capacity of 500 N with a resolution of 0.1 N.

When the stepper motor shaft turns, the carriage moves along the linear actuator. The carriage position must be determined at the start of each test in order to define a consistent reference frame. The carriage is homed by pressing microswitches at each end of the actuator. Each position (in motor steps) at which the carriage presses a switch is stored in the motor controller. The switch position closest to the motor is considered to be the origin position and the switch position farthest from the motor is considered to be the maximum position. During shear tests, the motor position is tracked in an open loop by counting steps relative to the origin position.

Test Platform Subsystem

The test platform subsystem is used to mount devices, constraint plates, and the Robotiq 2F-85 robotic gripper. This subsystem contains only mechanical components.

The main platform consists of a rectangular plate with an array of threaded holes, which is mounted on two pieces of aluminum extrusion to raise it to the approximate height of the force gauge shaft. For flat device tests, the device is connected to the test platform directly and a test sled is pulled across the top of the device by the force gauge. To constrain the vertical position of this test sled, a spring-loaded upper constraint plate sits above the flat device (positioned so that it applies a roughly constant force to the top of the sled). For gripper tests, the gripper is mounted to the test platform using a custom bracket and a target block is pulled out of the gripper's grasp by the force gauge.
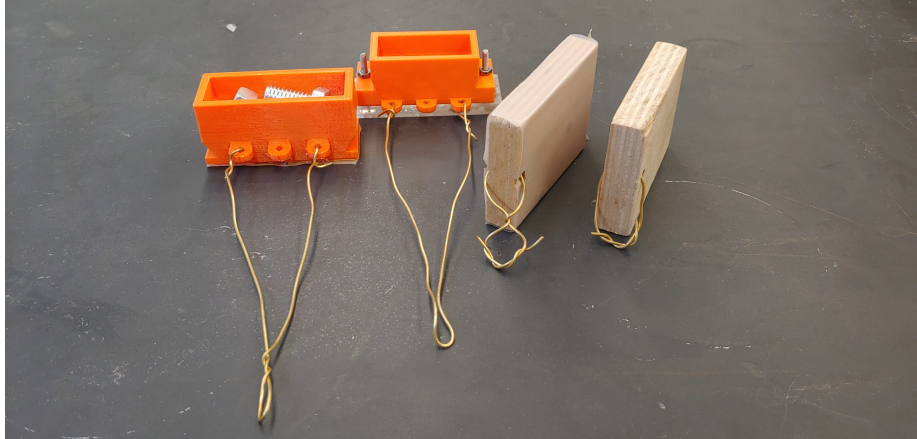
Figure 5.6: 3D-printed test sleds (left) and plywood target blocks (right) that are used for shear tests with flat and fingerpad devices respectively.

5.2.2 Data Collection and Integration

Data are collected from four sources:

1. Position data are tracked by counting motor steps.
2. Force data are collected by the force gauge.
3. Pressure data are collected by pressure sensors in the pneumatic control apparatus.
4. Where applicable, gripper status and position data are collected by the gripper.

The data are collected synchronously from four separate devices over serial. One value is read from each device in order in a loop and loop indices are recorded along with the data. This allows the data to be recorded in separate CSV files but still easily associated and integrated.

5.2.3 Test Process

Flat device tests use test sleds and gripper tests use target blocks. All sleds and target blocks used in this work are shown in Figure 5.6. Each 3D-printed sled features a cavity that can be filled with weights, a loop that is positioned at the same height as the force gauge connector, and (in some cases) holes that can be used to attach rigid bases of varying material to the sled. The target blocks are small pieces of wood that are used either bare or wrapped in tape.

Procedures

Once the actuator subsystem has been calibrated and a device has been mounted (either directly to the test platform or on the gripper), the following steps are required to run a shear force test:

1. Place the sled on the flat device or (for a gripper test) grip the target block.
2. Move the force gauge to the start position and connect it to the sled or target block.
3. Begin collecting data using the motor controller, force gauge, pneumatic controller, and (if applicable) gripper.
4. While continuing to collect data, pull the sled or target block away from the test platform at a constant velocity.

Limitations

The shear force tester generally works well and consistently, but does have a few limitations. Alignment is imperfect: the platform is not perfectly level relative to the linear actuator (because of component imperfections), the gripper is not mounted completely square to the test platform, and devices are not always perfectly flat so may not be level relative to the platform. Also, the microcontroller used for stepper motor controller has performance limitations. Its memory performance worsens after around 8-10 force tests, causing timing problems that interfere with motor driver signals and introduce noise to the test process. When this occurs, a power cycle is required to return it to its usual behaviour.

Chapter 6

Friction and Shear Testing Results

Previous chapters have presented the design and fabrication process for adaptive surface devices (Chapter 4) and methods for actuating and testing these devices (Chapter 5). This chapter discusses the first set of experiments conducted for this thesis, which explored the adaptive surface design space by characterizing the frictional properties of **flat adaptive surfaces** in different actuation states.

Although most of the questions addressed in this thesis relate to gripping (and thus require results from the gripper tests in Chapter 7), this chapter begins to address the first research question:

RQ1 How does multi-level active surface adaptation influence shear grip strength and shear friction?

Hypothesis: Surface deflection toward a gripped object (inflation) will increase grip friction.

Hypothesis: Surface deflection away from a gripped object (deflation) will decrease grip friction.

The results of this experiment series partially support these hypotheses. The hypothesis that inflating the active regions increases friction was supported by experimental data. For all experiments, inflating the active regions significantly increases shear force on a sliding object compared to the neutral state. However, the hypothesis that deflating the active regions decreases friction was *not* supported by experimental data. For the surface without microtopography, deflating the active regions marginally decreases shear force compared to the neutral state. For the microtopography surfaces, however, deflating the active regions actually significantly increases shear force compared to the neutral state (and sometimes even compared to the inflated state). This is an interesting difference between the two surface types that will be discussed in Section 6.3.

Overall, the shear force curves for each test are very consistent across trials, indicating that these multi-level adaptive surfaces tune friction in a repeatable, predictable manner—an outcome with exciting implications for contact modulation in robotic gripping.

6.1   Experimental Process

Following the procedures outlined in Chapter 5, tests in this experiment series measured the shear force experienced by a test sled sliding over an adaptive surface device. The overall test setup is pictured in Figure 6.1a.

Before each test, the device and sled were set up on the test platform. The device was mounted onto the platform with its active regions parallel to the direction of sled motion. To constrain the

(a) Test setup viewed from the front.   (b) Test setup viewed from the back.
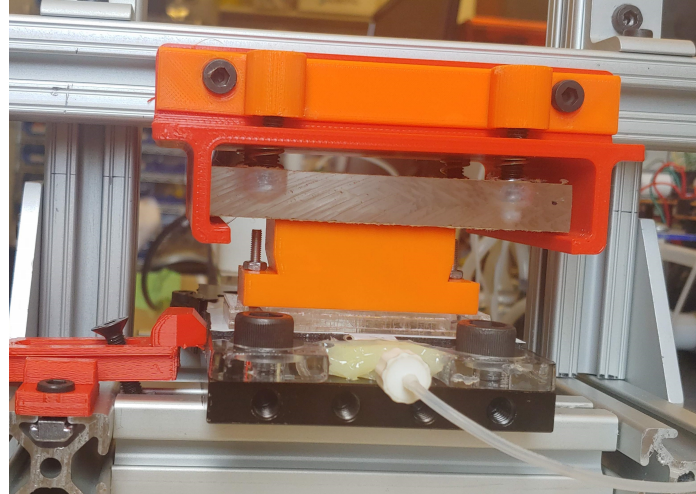
Figure 6.1: Shear test setup for flat devices. Before each test, the sled is placed as far toward the back of the test platform as possible. The upper constraint plate can be manually pressed upward, compressing the springs and allowing easy readjustment of the sled. During the test, the sled slides between the upper constraint and the adaptive surface device as it is pulled by the force gauge.

horizontal position of the device, bolts were inserted through its mounting holes (located near its pneumatic inlet) and into threaded holes at the far end of the test platform. Clamps or double-sided tape were used to constrain the device's vertical position. Two sleds were used in shear tests:

- a sled with a solid base that could either be used alone as a 3D-printed polylactic acid (PLA) target surface or covered with flexible target surfaces (e.g., PTFE tape), and

- a sled with holes in the base for attaching rigid target surfaces (e.g., acrylic as in Figure 6.2).

Before each test, the selected sled was filled with small weights (e.g., nuts and bolts) and its mass was recorded. The sled was then positioned on top of the device and connected to the force gauge. A spring-loaded plate (Figure 6.1b) was used to constrain the sled's vertical position.
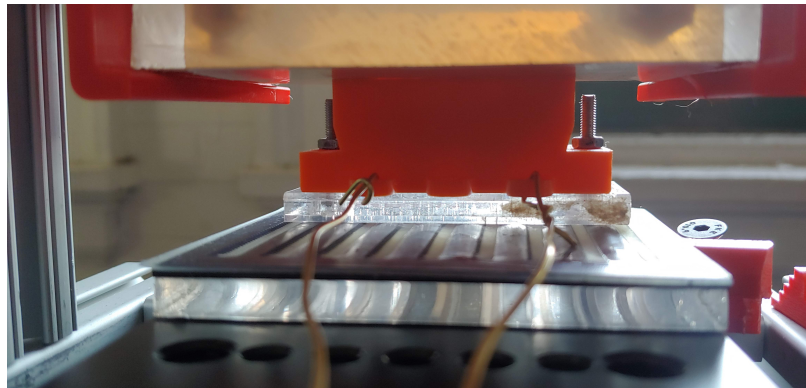
Figure 6.2: Test sled positioned between an adaptive surface device (bottom) and the upper constraint plate (top). A target surface composed of acrylic is bolted onto the sled.

Figure 6.3: The three adaptive surface devices used in flat device testing, pictured after all tests had been completed. The PVC device (centre) shows some visible wear as dark streaks along the active region edges, and the printed device with the short widthwise ridge features (left) shows some defects from excess resin deposition during printing that are not visible on the printed device with the long lengthwise ridge features (right).

6.2 Shear Force Tests

This section describes the tests that were conducted to characterize the frictional properties of flat adaptive surface devices. Test results are discussed here and then summarized in Section 6.3.

6.2.1 Test Procedure

Three adaptive surface devices (pictured in Figure 6.3) were tested. For all three devices, the active regions were rectangular strips with a width of 3 mm, but the contact layer designs differed:

1. A device with PVC tape as the top layer and no patterned microtopography.
2. A device with a 3D-printed (resin) surface as the top layer, on which long ridge features run lengthwise along the active regions.
3. Another device with a 3D-printed surface as the top layer, on which short ridge features run widthwise along the active regions.

Three different actuation pressures were used: -40 kPa for the deflated state, 0 kPa for the neutral state, and 40 kPa for the inflated state. Three trials were run for each actuation state, meaning that each sled-device pair was used in at least 9 trials in total.

6.2.2 Results and Discussion

Effect of Actuation Pressure

All adaptive surface devices show a correlation between actuation state and shear force. The force-time data measured when pulling an acrylic-based sled and a PTFE-based sled across a PVC device are shown in Figure 6.4. For both sleds, the inflated state produced significantly higher forces than other states and the deflated state produced slightly lower forces than the neutral state. Interestingly, the forces are fairly consistent across trials (i.e., the shaded region for each series is narrow) and the curves for the different actuation states are similar in shape within each plot.

The force-time data measured when pulling an acrylic-based sled and a PTFE-based sled across two printed devices with ridge features are shown in Figure 6.5. For both printed devices, unlike the PVC device, the deflated state always produced forces that were higher than in the neutral state. For the device with long ridges, the inflated state always produced higher forces than in other states, so much so that the force experienced by the acrylic sled sliding on the inflated device (Figure 6.5a)
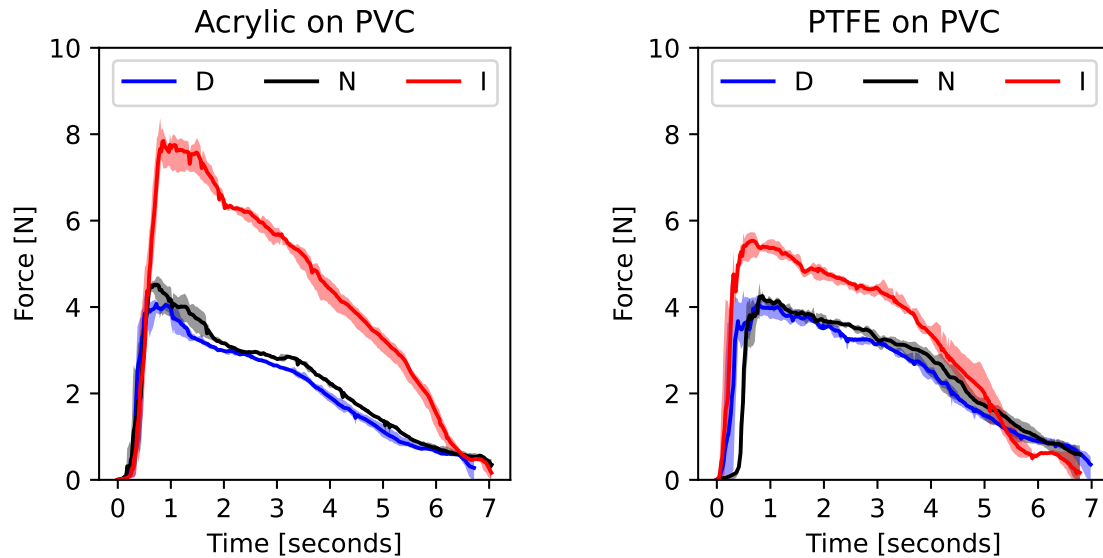
(a) Forces measured for the acrylic sled.

(b) Forces measured for the PTFE sled.

Figure 6.4: Shear force vs. time when pulling an acrylic-based sled and a PTFE-based sled across a PVC device. For each data series (representing data for one actuation state), the shaded region is the area covered by force curves from 3-4 different trials and the solid line is the average of these curves. Legend entry D stands for deflated, N stands for neutral, and I stands for inflated.

exceeded the force gauge's capacity and the test was aborted. For the device with short ridges, the inflated state always produced significantly higher forces than the neutral state. Interestingly, however, the PTFE sled experienced higher shear forces for the deflated state than for the inflated state when sliding on the device with short ridges. This result, where the *deflated* state produces the highest forces, was not seen for any other flat device test. This test will be discussed further in Section 6.3.

In this experiment series, it is clear that actuating the adaptive surface devices changes their frictional interactions with test sleds. The test results show similar relationships between device actuation state and shear force across different sled-device pairs: shear forces are highest in the inflated state and lowest in the deflated state (for the PVC device) or neutral state (for printed devices). Interestingly, multiple tests involving the printed surfaces produced force curves that were indicative of stick-slip behaviour (a phenomenon that was discussed in Section 3.2.1). This behaviour is visible as jagged sections of the curves in Figure 6.5 and is shown in more detail for the deflated state of the surface with long ridges in Figure 6.6.

The consistency of the force curves within each actuation state is also a particularly interesting result. The data for most sled-device pairs showed remarkably similar force-time and force-position curves (i.e., there was little variation in test data across trials, as indicated by the small area coverage of the shaded regions in Figure 6.4 and Figure 6.5). As seen in Figure 6.6, even the sled's stick-slip motion had a similar oscillation amplitude across trials.
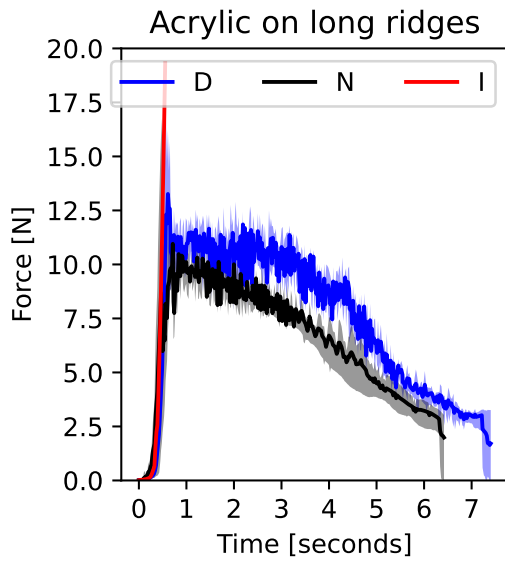
(a) Forces measured for the acrylic sled on the device with the long ridges.
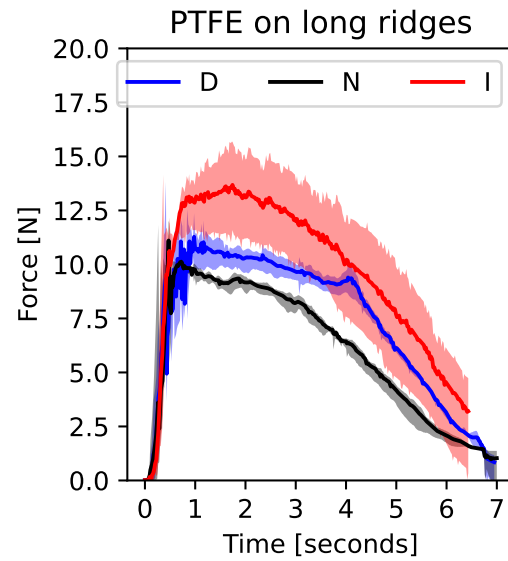
(b) Forces measured for the PTFE sled on the device with the long ridges.
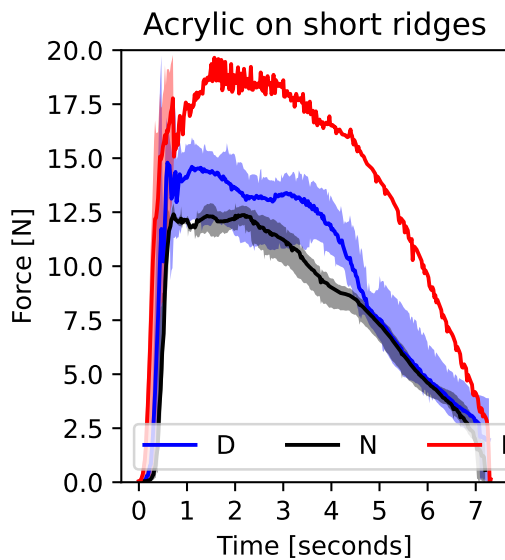
(c) Forces measured for the acrylic sled on the device with the short ridges.
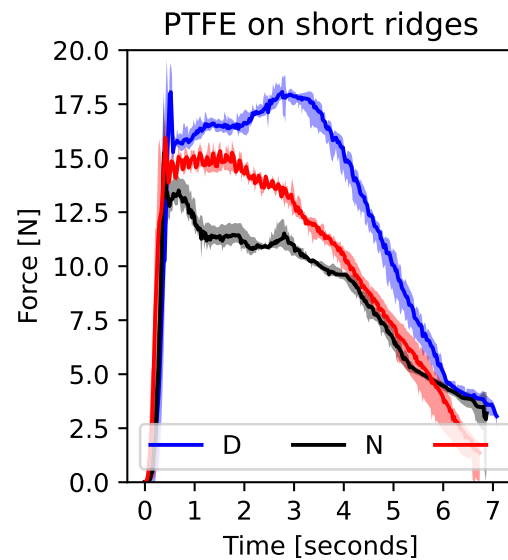
(d) Forces measured for the PTFE sled on the device with the short ridges.

Figure 6.5: Shear force vs. time when pulling an acrylic-based sled and a PTFE-based sled across two printed adaptive surfaces with ridge microtopography features of differing length and orientation. Each plot shows force data from all actuation states for one sled-device pair. For each data series (representing data for one actuation state), the shaded region is the area covered by force curves from 3-4 different trials and the solid line is the average of these curves. The inflated state for the acrylic sled on the device with long ridges is an exception where only 1 trial was conducted due to equipment limitations. Legend entry D stands for deflated, N stands for neutral, and I stands for inflated.
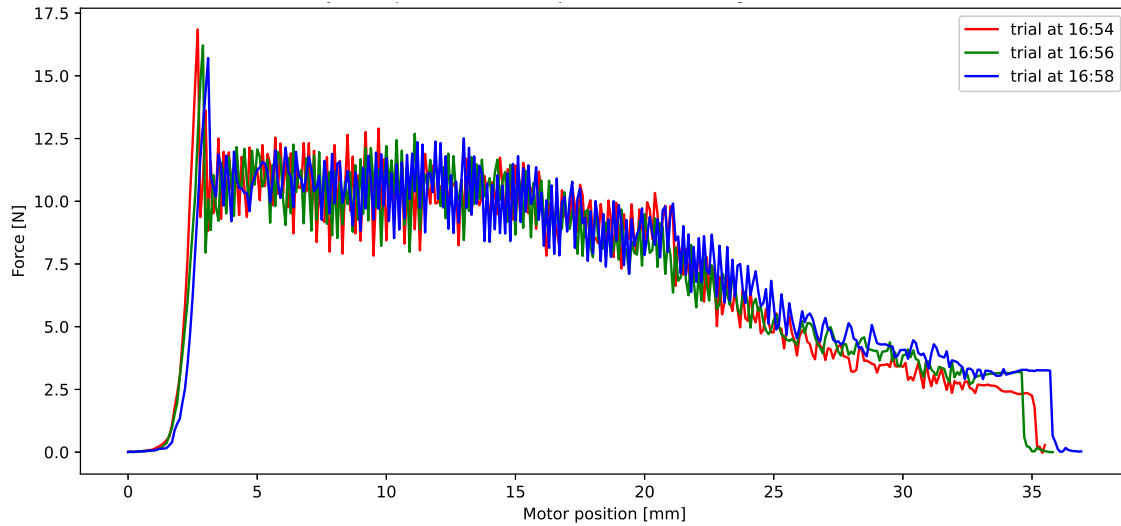
Figure 6.6: Shear force vs. motor (gauge) position when pulling an acrylic-based sled across a printed surface with long ridges and deflated active regions. The jagged oscillations in the force data indicate stick-slip behaviour.

Effect of Device and Sled Material Choice

For each trial, a representative mean shear force was computed using data from a 1 second period immediately after the initial peak of the force-time curve. The ranges and averages of these per-trial mean values are shown for each test (i.e., each sled-device pair and actuation state) in Figure 6.7. The average and peak shear force values for each test are also reported in Table 6.1. Many of the computed mean values have a very small range—this aligns with the observation that the force-time curves are consistent in shape across trials and indicates that the results of this testing are fairly repeatable.

Based on these average force data as well as the force-time curves shown in Figure 6.4 and Figure 6.5, it is clear that tests involving the PVC device have lower friction than tests involving the printed devices. Similarly, the difference between the average force in the neutral state and the
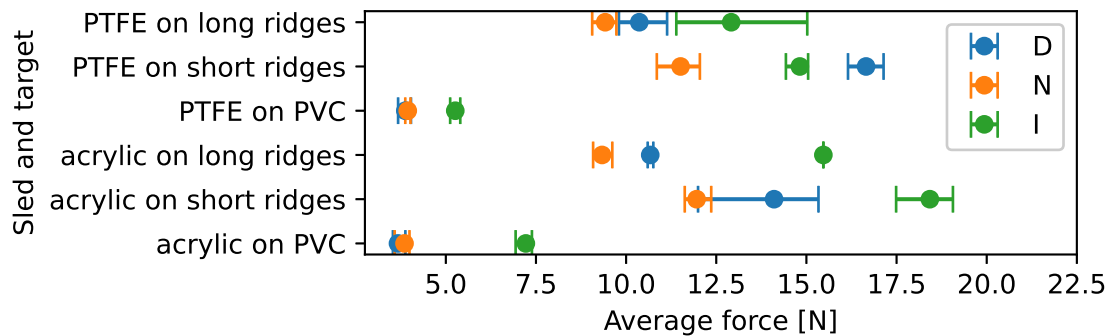
Figure 6.7: Comparison of mean shear forces from trials involving acrylic- and PTFE-based sleds on different flat adaptive surface devices. For most tests, shear force data come from 3-6 trials. This plot shows the range (bar) and average value (dot) of the per-trial mean force values.

Table 6.1: Average (F_a) and peak (F_p) shear forces for dual-constraint tests using different flat adaptive surface devices, test sleds, and actuation states. For each device-sled combination, the ratio of F_a to the average force for the neutral state (F_0, in blue) is provided. Each average force value is the mean of mean force values from 3-4* trials. Similarly, each peak force value is the maximum of maximum forces from 3-4* trials. Per-trial maxima were computed using all force measurements and per-trial mean values were computed using measurements from a 1 second interval shortly after the maximum force. *Data from 3 trials were available for all tests except for the test of the acrylic sled on the inflated printed surface with long ridges, for which only 1 trial was completed.

| Device	Sled	State	P [kPa]	F_a [N]	F_p [N]	F_a/F_0
PVC	Acrylic	D	-40	3.7	4.3	0.95
PVC	Acrylic	N	0	F_0=3.9	4.7	1
PVC	Acrylic	I	+40	7.2	8.4	1.85
PVC	PTFE	D	-40	3.9	4.5	0.99
PVC	PTFE	N	0	F_0=3.9	4.6	1
PVC	PTFE	I	+40	5.3	5.7	1.36
Printed (long ridges)	Acrylic	D	-40	10.7	16.9	1.15
Printed (long ridges)	Acrylic	N	0	F_0=9.3	16.8	1
Printed (long ridges)	Acrylic	I	+40	15.5	>20	1.67
Printed (long ridges)	PTFE	D	-40	10.4	13.8	1.11
Printed (long ridges)	PTFE	N	0	F_0=9.4	12.0	1
Printed (long ridges)	PTFE	I	+40	12.9	15.7	1.37
Printed (short ridges)	Acrylic	D	-40	14.2	19.8	1.18
Printed (short ridges)	Acrylic	N	0	F_0=12.0	13.5	1
Printed (short ridges)	Acrylic	I	+40	18.4	19.8	1.53
Printed (short ridges)	PTFE	D	-40	16.7	19.6	1.45
Printed (short ridges)	PTFE	N	0	F_0=11.5	17.7	1
Printed (short ridges)	PTFE	I	+40	14.8	16.8	1.29

average force in the inflated state is smaller for the tests involving the PVC device than for most tests involving the printed devices. This suggests that the printed surfaces are more suitable for tuning friction because actuating these surfaces allows a larger range of shear forces to be achieved.

6.3 Discussion

This chapter has characterized the extent to which actuating flat adaptive surface devices can tune friction between the device and a sliding sled. This section summarizes the main results and discusses limitations and next steps.

6.3.1 Main Results

The experiments in this chapter characterize the impact of adaptive surface actuation on shear forces experienced by a constrained sliding sled. The main results from these experiments are that:

- Multi-level adaptive surface devices can consistently tune friction.
- Inflating active regions increases the friction at the interface.
- For surfaces without microtopography, deflating active regions decreases friction.
- For surfaces with microtopography, deflating active regions increases friction.

This difference in deflated device behaviour is possibly an artefact of the printed surfaces' contact and structural layer designs. The printed surfaces used as contact layers in these devices have relatively thick (0.5 mm) substrates. When a printed surface is deflated, its thick top surface deflects by only a very small distance across the active region width (3 mm). The microtopography-covered active regions may not be fully recessed, meaning that a test sled may contact both the microtopography and the inactive regions—leading to a higher contact area than expected in the deflated state.

All surfaces tested in this chapter would be suitable for friction tuning, but in different circumstances. The PVC device is useful when lower overall friction levels are needed and when the neutral state should be an intermediate state (i.e., friction can be both increased and decreased from the default level). The printed devices are useful when higher overall friction levels are needed and when the neutral state should be low-friction (i.e., friction can only be increased from the default level).

6.3.2   Limitations and Next Steps

This experiment series was limited by time constraints (due to challenges with the test apparatus) and imperfect manufacturing of printed microtopography surfaces. The test setup initially used an upper constraint plate without springs, which led to inconsistent results since this plate had to be removed and replaced for each new test. When data collection was restarted after the test setup was redesigned, there was not much time remaining, and so the number of devices tested and number of trials performed for each device were both limited. To confirm experimental results, more devices should be tested using more trials per test. Other limitations stem from two mistakes made during manufacturing of the printed surfaces:

- A conservative estimate of the printer's capabilities led to overly thick surface substrates.
- Imprecise assembly led to misalignment between layers for the surface with short ridges.

The desired deflation behaviour for the printed surfaces was for the surface microtopography to be fully pulled away from the interface. Since the overly thick substrate retracts only a small distance at -40 kPa, the actual behaviour appears to be that the features retract slightly but remain in contact with the sled at the interface, particularly near the active region edges. This issue is exacerbated for the device with short ridges, for which some microtopography is positioned outside of the active regions due to misalignment between layers. For this device, deflation may have allowed the sled to contact the inactive regions of the device while *also* contacting misplaced and/or insufficiently retracted ridges, leading to its unusually high friction in its deflated state.

Overall, the results presented in this chapter indicate that adaptive surface devices with PVC or printed microtopography surfaces can effectively tune friction. The next chapter discusses the characterization of adaptive gripper fingerpads.

Chapter 7

Shear Tests of Adaptive Fingerpads

Friction and shear force testing for flat devices (Chapter 6) explored the adaptive surface design space, yielding a candidate set of designs that effectively and robustly adapted surface friction. These designs were modified to fit a gripper fingerpad form factor, creating **adaptive fingerpad** devices. The adaptive fingerpads were then attached to an industrial robotic gripper (shown in Figure 7.1) and used to grip objects under shear load. The design and fabrication process for adaptive fingerpad surfaces was discussed in Chapter 4; this chapter describes the experimental characterization of their frictional properties and gripping behaviour.
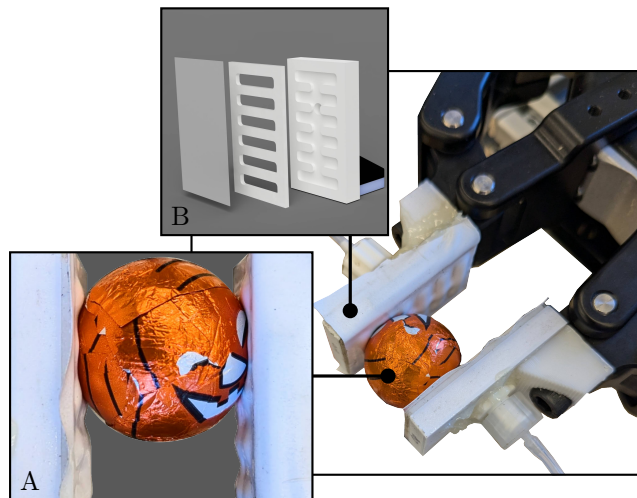
Figure 7.1: Structured pneumatic fingerpads gripping a round object. Inset A: inflated active regions partially enveloping the object. Inset B: a render of the fingerpad layers.

Results in this chapter address the research questions introduced in Chapter 2. An overview of key results for each question is provided below.

RQ1 How does multi-level active surface adaptation influence shear grip strength and shear friction?
Hypothesis: Surface deflection toward a gripped object (inflation) will increase grip friction.
Hypothesis: Surface deflection away from a gripped object (deflation) will decrease grip friction.
Hypothesis: Adding microtopography to grip surfaces will increase grip friction.

Hypothesis: An active microtopography-covered surface will experience higher grip friction than either an active flat surface or a neutral microtopography-covered surface; i.e., multi-level adaptation will have synergistic effects.

The first hypothesis is generally supported by experimental results in Section 7.2 and Section 7.3: when fingerpads are actuated after gripping an object, inflating the active regions always increases both normal and shear forces, and this increase is usually substantial. However, the second hypothesis is contradicted by experimental results: when fingerpads are actuated after gripping an object, deflating the active regions slightly decreases normal force, but shear force is generally unchanged or only marginally decreased compared to the neutral state. Interestingly, the last two hypotheses are contradicted by experimental results, as microtopography-covered fingerpads appear to have similar friction levels to flat fingerpads made from the same material.

RQ2 How does the order of operations when using multi-level surface adaptation in a gripping process impact grip friction?

Hypothesis: Since the gripper used in this work stops closing its fingers when object contact is detected, inflating the adaptive grip surface pre-gripping (such that initial contact between an object and the grip surface occurs only in the raised active regions) will result in decreased contact area and decreased friction, whereas inflating the adaptive grip surface post-gripping will result in increased contact area and increased friction.

This hypothesis is confirmed by experimental results in Section 7.3, as inflating the fingerpads pre-gripping always decreases friction whereas inflating post-gripping increases friction.

RQ3 Can we leverage knowledge of the pressure in the pneumatic chamber to draw conclusions about changing grip conditions?

Hypothesis: When the adaptive grip surface is inflated prior to gripping, the pressure in the pneumatic chamber will increase when an object is gripped.

This hypothesis is confirmed by experimental results in Section 7.4, as gripping an object with inflated fingerpads produces a rapid increase in internal pressure that can be used for object detection.

RQ4 Can we use grip surface adaptation to facilitate macroscale grip interactions like interlocking and enveloping?

Hypothesis: When gripping small objects, more enveloping/interlocking interactions will be present when the adaptive grip surface is inflated than when it is neutral.

Hypothesis: When the adaptive grip surface is deflated while gripping objects with protrusions at a lengthscale similar to the active region lengthscale, interlocking will occur.

This hypothesis is confirmed by experimental results in Section 7.5, which show that both interlocking and enveloping interactions can be demonstrated with compatible objects.

Overall, the adaptive fingerpad experiments show an exciting relationship between actuation state, actuation timing, and grip interface friction. Related works with adaptive grip surfaces that use membrane deflection [55], [131], [144]–[146], [148]–[151] do not investigate the impact of actuation timing on grip friction, nor do they usually test a deflated state. Of the few existing friction-tuning grippers [10], [12], [55], [128], [130], [131], most do not investigate the impact of combining

frictional effects at the microscale from microtopography with the mesoscale effects from surface morphology changes and macroscale effects from grip articulation (i.e., they look at only microscale and macroscale effects, or only mesoscale and macroscale). Many of the relationships and multi-level control options investigated in this chapter have not yet been comprehensively explored in the literature. While the results presented in this work are limited, they open the door to a rich and largely unexplored experimental space.

7.1 Experimental Process

Gripper experiments used the Robotiq 2F-85 gripper, an underactuated two-fingered rigid gripper[1]. This section describes the four processes involved in *all* gripper experiments:

1. mounting the gripper to the test platform,
2. installing custom adaptive fingerpads on the gripper,
3. actuating the fingerpads, and
4. gripping objects.

Experiment-specific test procedures are explained in the associated experiment sections.

7.1.1 Gripper Setup

Once the gripper is mounted to the test platform as described below, its existing fingerpads can be removed easily and new fingerpads can be installed.

Gripper Mounting

A custom laser-cut bracket is used to mount the gripper on the test platform as shown in Figure 7.2. The gripper is mounted such that the opening plane of its fingers is roughly horizontal. Mounting the gripper in this orientation ensures that gravitational loads acting on a gripped object impact the fingerpads equally (as opposed to, e.g., the unequal distribution of load that would occur when positioning the gripper with one finger below the other). The gripper could also have been mounted with its fingers pointing down; however, in this orientation, the vertical position of the fingertips would vary relative to the force gauge and object positioning would become unwieldy.[2]

Fingerpad Installation

The adaptive fingerpads tested in this series of experiments were designed as drop-in replacements for the stock (original) fingerpads of a 2F-85 gripper. The gripper's stock fingerpads are connected using two positioning pins and a bolt. The fingerpads can thus be easily removed and replaced provided that the replacement fingerpads have a flat base with correctly sized and spaced mounting holes. Detached fingerpads are shown in Figure 7.3.

---

[1]Robotiq 2F-85 product page: robotiq.com/products/adaptive-grippers

[2]Since the gripper's finger extension depends on the finger separation (i.e., when the fingers come closer together they also extend farther out from the gripper body), the vertical position of the fingertips during gripping depends on the thickness of the gripped object if the gripper is mounted with its fingers pointing down.

(b) Gripper viewed from the side.

(a) Acrylic bracket connecting the gripper base to the test platform, viewed from the back.

(c) Gripper with one of its original ('stock') fingerpads replaced with an adaptive fingerpad, viewed from the front. An air supply tube is connected at the back of the adaptive fingerpad.

Figure 7.2: 2F-85 gripper mounted to test platform.
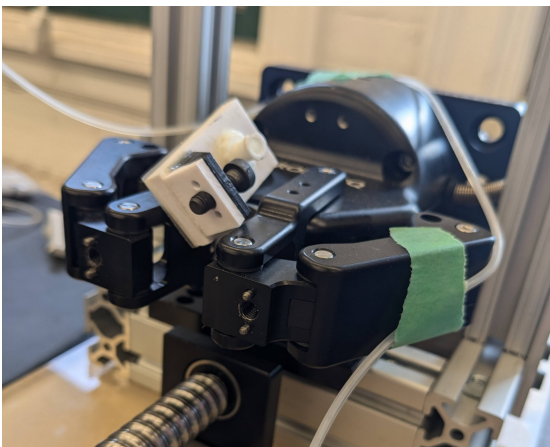
(a) Back side and base of an adaptive fingerpad, with the pneumatic inlet fitting (white) visible at the back of the fingerpad.

(b) Front side and base of an adaptive fingerpad. The active regions of the fingerpad surface are visible under the (translucent) top layer.

Figure 7.3: 2F-85 gripper after removal of its fingerpads. The pins and threaded holes used to position and secure fingerpads are visible in the gripper finger surfaces. A detached fingerpad with a bolt inserted through its base is resting on top of the gripper.

7.1.2   Gripper Control

Like the flat devices tested in Chapter 6, the adaptive fingerpads are actuated using a custom pneumatic controller (described in Chapter 5). This section describes fingerpad actuation and gripper control and then summarizes the five different actuation cases used during gripper experiments.

Actuation Procedure

The control parameters used when actuating the gripper are shown with their value ranges in Table 7.1. When gripping, the 2F-85 closes until *either* a preset target finger separation distance is reached *or* an object is detected (based on finger force-feedback) [175]. This means that the target finger separation may not always be reached—and in fact, it typically is not, since the finger separation is often set to be slightly less than the target object width to make up for slight errors in finger position feedback. If the exact size of a target object is not known, the gripper can be set to close to an underestimate of the object size. With this method, the gripper fingers will stop moving when object contact is detected; however, the object is typically gripped with more force than if the finger separation is set precisely, meaning that this method poses a risk to delicate objects.

Table 7.1: Range of possible control parameter values for grip testing. Note that the grip force setting is approximate, so actual grip forces are typically not equal to target grip forces.

Parameter	Units	Minimum value	Maximum value
Actuation pressure	kPa	-40	+40
Fingerpad separation	mm	0	85
Nominal grip speed	mm/s	20	150
Nominal normal grip force	N	20	235

The 2F-85 has a grip readjustment feature, which is disabled at the minimum grip force setting (20 N) and enabled at all other grip force settings. This regrasp feature activates when:

1. grip force is set to be >20 N, and

2. an object was detected while closing, and

3. because an object was detected, the fingers have not reached the target finger separation distance (which acts as a minimum separation distance here), and

4. the object is slipping (based on changes in the 2F-85's automatic object detection signal).

When the regrasp feature activates, the gripper tightens its fingers repeatedly until either the object stops slipping or the minimum finger separation distance is reached. Since these changes in finger position and grip force add variability to the test process, activating the regrasp feature during fingerpad testing is undesirable. Accordingly, all tests were conducted with grip force set to 20 N.

A simple three-step process is used for control of the gripper and the adaptive fingerpads:

1. If applicable, the fingerpads are actuated to their pre-grip pressure level. This step is called *prior* actuation.

2. The target object is held between the gripper fingerpads and the gripper is set to close to its target separation at its target speed and force.

3. If applicable, the fingerpads are actuated to a different post-grip pressure level. This step is called *live* actuation.

Actuation Test Cases

When conducting experiments, five fingerpad actuation test cases were used:

1. Neutral (N), where the pads were not actuated.
2. Deflated-live (DL), where the pads were deflated *after* gripping a block in the neutral state.
3. Deflated-prior (DP), where the pads were deflated *before* gripping a block.
4. Inflated-live (IL), where the pads were inflated *after* gripping a block in the neutral state.
5. Inflated-prior (IP), where the pads were inflated *before* gripping a block.

A schematic of these cases is shown in Figure 7.4. In all cases, the pneumatic controller was used to control fingerpad pressure—even for the neutral case, the controller was still connected to the fingerpads in order to monitor their actual internal pressure.
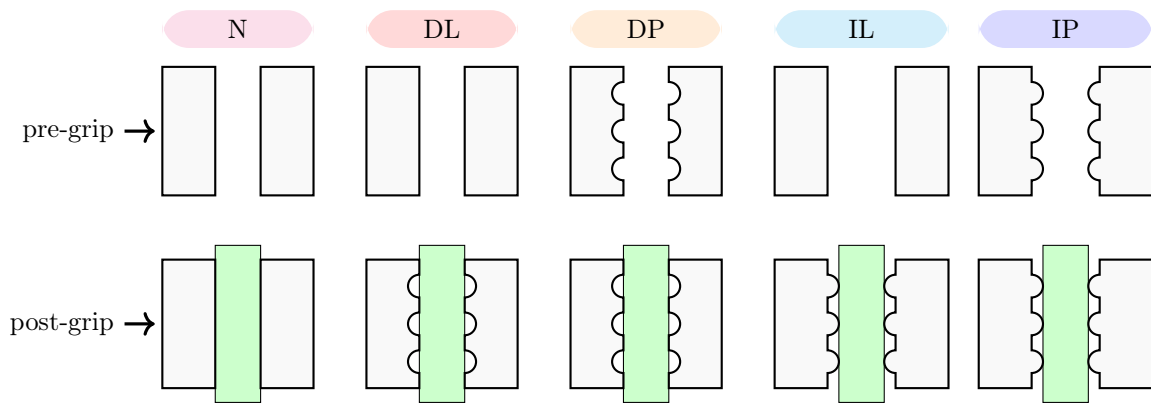

Figure 7.4: Schematic of the five actuation cases used for testing adaptive fingerpads. N is neutral (no actuation), DL is deflated-live (grip-then-deflate), DP is deflated-prior (deflate-then-grip), IL is inflated-live (grip-then-inflate), and IP is inflated-prior (inflate-then-grip).

7.2   Normal Force Tests

According to the Amonton-Coulomb law discussed in Section 3.2, friction force is proportional to normal force. Although this law does not perfectly describe compliant materials (like the soft surface of the adaptive fingerpads), normal force still significantly affects friction for such materials. It is thus necessary to assess the impact of surface adaptation on the *normal* forces applied to a gripped object before evaluating its impact on *shear* forces. To assess how surface adaptation impacts normal grip force, a force-sensitive resistor (FSR) was used to test normal force during gripping with different actuation cases.

7.2.1   Test Procedure

The force-sensitive resistor (FSR) was obtained from the Myhal Centre Fabrication Facility and came attached to a small piece of metal backing. The holes in this metal backing were used to position the FSR and backing relative to a mounting plate, and then the FSR was connected to the mounting plate using double-sided tape as shown in Figure 7.5a.

(a) The FSR mounted to a metal plate.

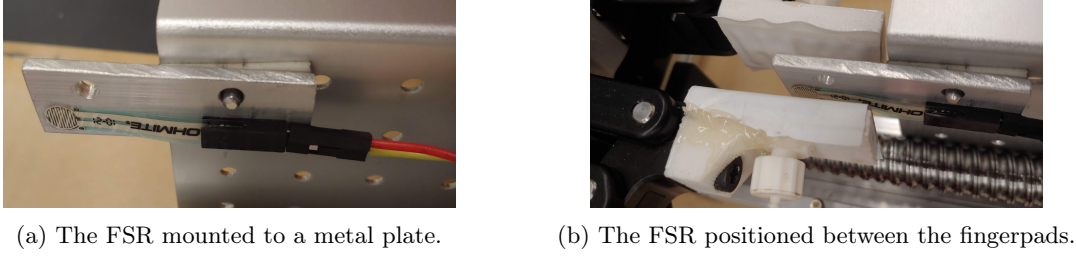(b) The FSR positioned between the fingerpads.

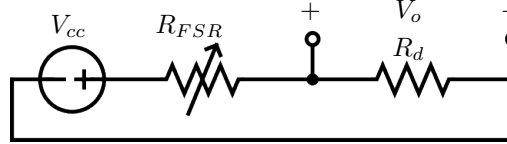Figure 7.5: Force-sensitive resistor (FSR) test setup.

Figure 7.6: Schematic for the voltage divider circuit used to determine the FSR resistance.

To test the normal force applied by the gripper fingerpads, the FSR was positioned between the fingers of the opened gripper as shown in Figure 7.5b. Since the gripper fingers are underactuated and thus will tilt to better align to gripped objects, the FSR did not need to be perfectly parallel to the fingerpads. The FSR position was kept relatively consistent to avoid inconsistencies caused by differing relative positions of the small FSR active area and the (similarly small) fingerpad active regions. PVC-covered fingerpads were used as the adaptive fingerpads in this experiment.

FSR data were gathered by reading the output voltage in a voltage divider circuit (shown in Figure 7.6) using an ATmega2560 microcontroller. The supply voltage was $V_{cc} = 3.3V$ and the pull-down resistor had a resistance of $R_D = 10\text{k}\Omega$. The measured output voltage (V_o) can be expressed in terms of the FSR resistance (R_{FSR}) using the voltage divider rule:

$$V_o = V_{cc} \left(\frac{R_D}{R_D + R_{FSR}} \right) \tag{7.1}$$

Rearranging Equation 7.1, the resistance across the FSR can be computed in $\text{k}\Omega$:

$$R_{FSR} = R_D \left(\frac{V_{cc}}{V_o} - 1 \right) \tag{7.2}$$

The FSR resistance has an approximate inverse power-law relationship with applied force:

$$F_{FSR} \propto \frac{1}{R_{FSR}} \tag{7.3}$$

FSRs are generally not suitable for *absolute* force measurements, but are useful for *relative* force measurements. FSR data from this experiment were thus compared across fingerpads and across actuation states in terms of relative voltage and resistance results.

7.2.2   Results and Discussion

Typical voltage readings and approximate resistances for each fingerpad type and actuation case are shown in Table 7.2. Voltage-time data from several trials are presented in Figure 7.7, with data for the adaptive fingerpads plotted versus actuation pressure in Figure 7.7a and data for the stock fingerpads plotted alone in Figure 7.7b. The "forces" discussed in this section are gauged in terms of resistance, where a lower FSR resistance corresponds to a higher sensed force (per Equation 7.3).

Table 7.2: Voltage readings and the corresponding FSR resistances (computed with Equation 7.2). For each fingerpad type and actuation case, the average of all voltage readings is reported and the standard deviation is given in parentheses. Values were computed using data from 17 and 18 trials for the PVC and stock fingerpads respectively. The data range is 1.83V-1.70V=0.13V. Higher voltage/lower resistance corresponds to higher force.

Fingerpads	Case	Measured Voltage V_o [V]	Resistance R_{FSR} [kΩ]
PVC	DL	1.70 (0.11)	9.5
PVC	DP	1.75 (0.17)	8.9
PVC	N	1.80 (0.13)	8.3
PVC	IL	1.83 (0.07)	8.0
PVC	IP	1.80 (0.08)	8.3
Stock	N/A	1.80 (0.38)	8.3

The Robotiq 2F-85 gripper controls normal force during grip closure: its fingers stop moving once object contact is detected based on an approximate force threshold (with current feedback from the fingers used to proxy force) [175]. This means that the adaptive fingerpads and stock fingerpads should establish grip on an object with similar average normal forces despite their differing material composition. The FSR data in Table 7.2 generally align with this expectation: stock fingerpads, adaptive fingerpads in the N case, and adaptive fingerpads in the IP case all grip with the same force (i.e., the same FSR resistance of 8.3kΩ). However, the normal force applied by the adaptive fingerpads in the deflated prior (DP) case is slightly lower (i.e., the FSR resistance is higher at 8.9kΩ). This decrease in force likely occurred because the FSR was positioned near the centre of an active region, which would be retracted in the deflated state and would not fully contact the FSR.

The deflated live (DL) and inflated live (IL) cases involve fingerpad actuation *after* an object has been gripped, and so object detection-based force limits are not as directly applied to the fingerpads in these cases. Both live actuation cases show normal forces that differ significantly from the neutral and prior cases. When the fingerpads grip an object in their neutral state and then deflate, the FSR resistance increases from 8.3kΩ to 9.5kΩ. In contrast, when the fingerpads grip an object in their neutral state and then inflate, the FSR resistance decreases from 8.3kΩ to 8.0kΩ. The normal force test data thus suggest three interesting conclusions:

1. Both neutral adaptive fingerpads and stock fingerpads apply the same normal grip force.

2. Inflating adaptive fingerpads during gripping (the IL actuation case) reduces the resistance of the force-sensitive resistor by about 4%, so inflation slightly increases normal force.

3. Deflating adaptive fingerpads during gripping (the DL actuation case) increases the resistance of the force-sensitive resistor by about 15%, so deflation slightly decreases normal force.

Overall, however, the impact of fingerpad actuation is relatively minor, and the standard deviation values reported in Table 7.2 are also large in comparison to the voltage measurement range.
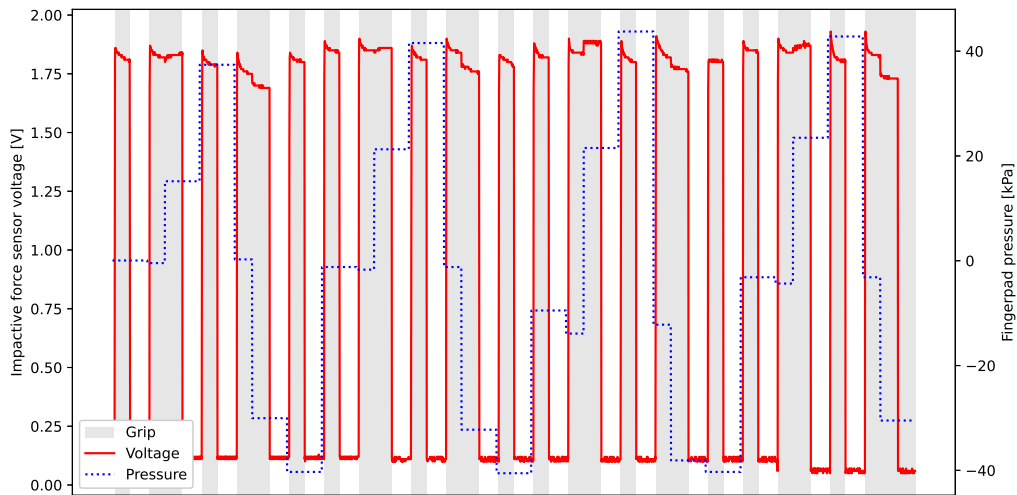
(a) FSR voltage when gripped by the PVC fingerpads in various actuation cases. For N cases, the fingerpad pressure (blue dashed line) is 0 kPa for the duration of the grip event. For DP/IP cases, the pressure is -40/+40 kPa (respectively) throughout the grip event. For DL/IL cases, the pressure drops/rises from 0 kPa to -40/+40 kPa after the grip event begins. DL and IL pressures appear to differ from DP and IP pressures because the pressure level is recorded before the fingerpads fully pressurize—in actuality, however, the fingerpad pressures for the DL and IL cases were close to -40/+40 kPa throughout the majority of data collection time.
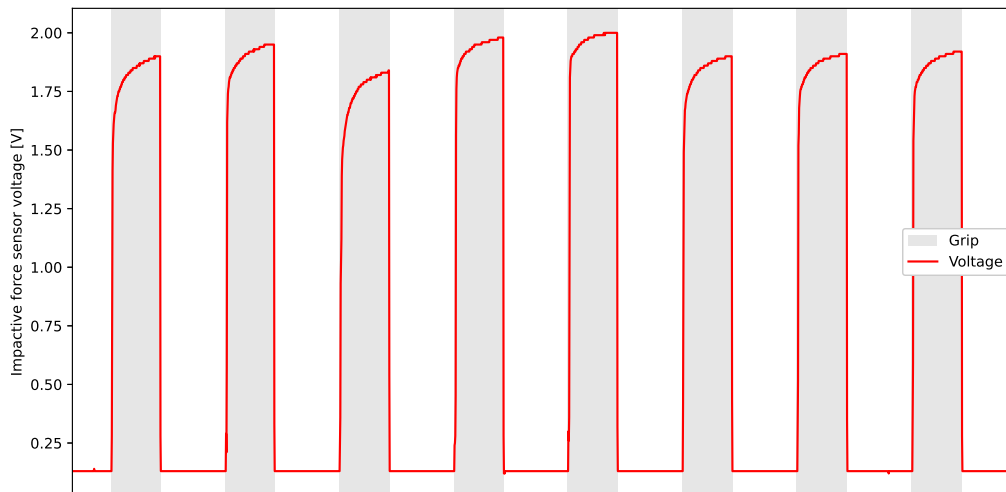
(b) FSR voltage when gripped by the stock fingerpads.

Figure 7.7: Voltage (red line) through a force-sensitive resistor (FSR) in response to grip events and (for the PVC fingerpads) fingerpad actuation pressure. Grey regions indicate grip events (i.e., time periods in which the gripper was closed against the FSR). Higher voltage indicates lower FSR resistance and higher compressive force.

Looking at the measured voltage curves in Figure 7.7, the voltage measurements for each grip event differ in behaviour for the adaptive fingerpads versus the stock fingerpads. For the stock fingerpads shown in Figure 7.7b, the voltage rises sharply when the fingerpads contact the object but then continues to rise slowly over the duration of the grip event. A typical grip event in these experiments lasted for around 4 seconds, which is too long a time period for this slow rise in voltage measurements to be adequately explained by material creep or finger inertia. For the adaptive fingerpad data shown in Figure 7.7a, in contrast, the voltage rises to a maximum when the fingerpads contact the object but then slowly decreases over the duration of the grip event. This decrease in voltage could be the result of the viscoelasticity of the soft materials used in the adaptive PVC fingerpads. When the fingerpads close around the FSR, the pressure in the contact region will be higher than in non-contact regions, but the soft middle and top layers of the fingerpads will then deform and distribute load. It is possible that the FSR voltage under steady-state load still increases over time for adaptive fingerpads (as it does for stock fingerpads) but is counteracted by force reduction due to deformation. More testing with different rigid and soft fingerpad materials could help to determine the cause of this difference in voltage trends between different fingerpads.

7.3   Shear Force Tests

The main design objective in this project was to controllably tune friction at the grip interface. The shear force tests performed to assess frictional properties were hence more extensive than other tests of the grip surface. These tests investigated multiple fingerpads (with different top layer materials) gripping different target block materials. This section presents the results of all shear force tests conducted on the adaptive fingerpads.

7.3.1   Test Procedure

Target Objects

Two plywood blocks (pictured in Figure 7.8) were used as target objects during shear testing. One block was wrapped with thin PTFE (Teflon) tape and served as a low-friction target, while the other was left unwrapped and served as a high-friction target. The blocks were equal in thickness prior to wrapping, meaning that the Teflon-wrapped block was very slightly thicker after wrapping. A loop of wire was attached to each block in order to connect the blocks to the force gauge.

Figure 7.8: Target blocks for shear tests. Left: bare plywood. Right: wrapped with PTFE tape.

Shear Testing

To assess the friction-tuning capabilities of the fingerpads, a custom-built force tester (described in Chapter 5 and pictured in Figure 7.9) was used to measure the shear force required to cause a block to slip when gripped using different fingerpad actuation test cases. To set up each test, the gripper was mounted in a fixed position, its fingers were closed to grip a block, and then the gripped block was connected to a force gauge. T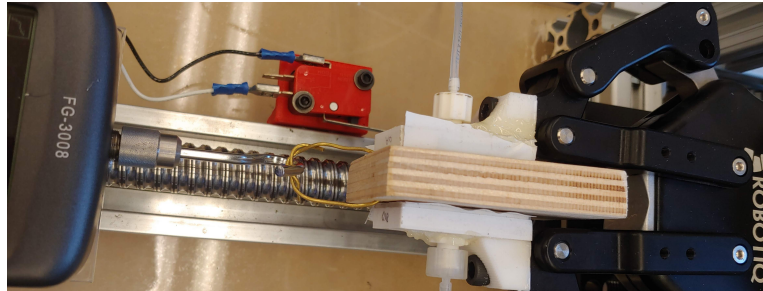he gauge was then translated away from the gripper at a constant velocity, slowly pulling the block from the gripper's grasp. Force data, actuation pressure data, gauge position data, and gripper status data were collected throughout the test.

(b) The force gauge travels along an actuated linear axis, applying force to the gripped block in the process. The applied force causes the block to slide relative to the gripper.

(a) A gripped target block is connected to the force gauge.
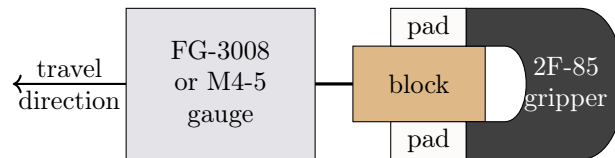
(c) Schematic showing connections and interfaces between gauge, block, and gripper during shear tests.

Figure 7.9: Shear testing apparatus for frictional characterization of fingerpads. The fingerpads are actuated by the pneumatic control apparatus (not pictured) before/after gripping the target block.

The objective of friction tuning is often safe gripping of delicate objects. Accordingly, a light grip was used during testing in order to fairly represent situations in which delicate objects must be grasped without excessive normal force. This was achieved by setting the target finger separation distance to be slightly larger than the block width, thereby avoiding the excessive grip forces that could otherwise be caused by slight positional errors. Using this separation distance for every test produced a consistently loose but stable grasp.

For the majority of gripper tests, an Shimpo FG-3008 gauge with a limit of 100 N was used. However, this gauge began malfunctioning and had to be replaced with the Mark-10 M4-5 force gauge that was used for testing of flat devices. Since the M4-5 has a force limit of 25 N, some shear tests could not be performed using this gauge. Specifically, the shear forces applied to a plywood block by 3D-printed adaptive fingerpads could not be measured, as peak shear forces for this material combination exceeded 25 N.

7.3.2   Results and Discussion

This section presents the results of testing conducted using the adaptive fingerpads, examining these results in terms of the impact of actuation case, fingerpad surface material, and target block material.

Effect of Actuation Case

The general hypothesis for these experiments was that, for most fingerpad surfaces and target materials, there should be an actuation pressure for which actuating the adaptive fingerpads results in a change in the friction at the fingerpad-target interface. Inflating the active regions should generally increase the contact area at the interface (likely causing interlocking and increasing friction), whereas deflating the active regions should generally decrease the contact area (likely decreasing friction). To test this hypothesis, experiments were conducted to characterize the relationship between

1. the internal pressure of PVC-covered fingerpads, and
2. the resulting shear force on a gripped PTFE-covered block.

These experiments used actuation pressure levels ranging from -40 kPa to +40 kPa. For each nonzero internal pressure level, both the live case (DL and IL) and the prior case (DP and IP) were tested. The characterization results are shown in Figure 7.10.
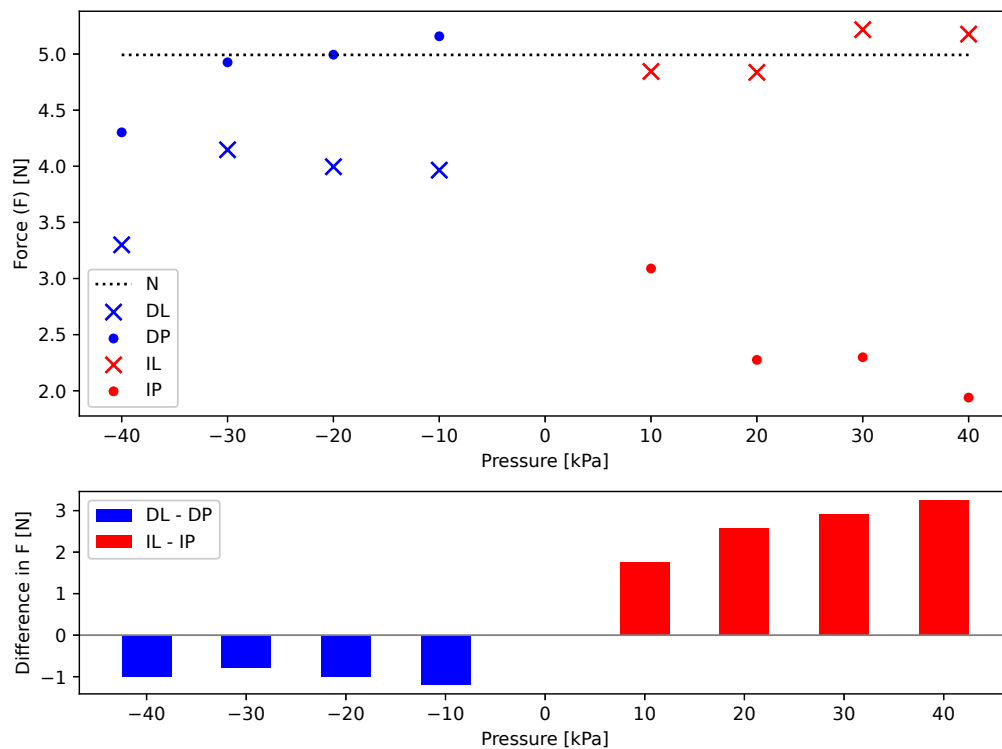
Figure 7.10: Shear force on a PTFE-wrapped block when gripped with fingerpads at different pressure levels. Forces in the IL case are much higher than in the IP case, and the difference between the cases (IL-IP) increases with pressure. In contrast, the difference between the DL and DP cases (DL-DP) is smaller and does not notably change with pressure. Each point is the average of data from 3 trials. All data were gathered in one day to control the impact of environmental conditions.

Deflated cases: The average shear forces were almost always lower in the DL case than in the DP case, with differences in forces (i.e., subtracting as $F_{DL} - F_{DP}$) ranging from -0.2 N to 1.2 N. This means that the friction on the block is lower when the active regions deflate after gripping (as opposed to before). As pressure increased from -40 kPa to 0 kPa, there was a very slight trend toward higher forces (for both DL and DP), likely due to increasing contact area between the fingerpad surface and the gripped block. At lower (more negative) pressures, the fingerpad surface recesses farther into the fingerpad's internal pneumatic chamber and is pulled tightly against the edges of the active regions, meaning that the surface does not contact the block in the active regions. By contrast, at higher (less negative) pressures, the fingerpad surface recesses only slightly, and parts of the active region surfaces may still contact the block, especially near the active region edges.

Inflated cases: The average shear forces in the IL case were always higher than in the IP case, with differences (IL-IP) ranging from 0.5 N to 3.2 N. This means that the friction on the block is higher when the active regions inflate after gripping (as opposed to before). As pressure increased from 0 kPa to +40 kPa, there were significant trends toward higher forces in the IL case and lower forces in the IP case. Again, these trends are likely related to changes in contact area. In the IP case, the gripper would have detected an object soon after the protruding active regions of the fingerpads contacted the block, causing the gripper to stop closing before the inactive regions of the fingerpads came into contact. This resulted in a lower final grip contact area relative to the neutral case. In contrast, in the IL case, the inflation of the active regions likely increased contact area by filling in any remaining gaps between the block and the active regions and promoting interlocking.

Overall, given appropriate actuation pressures, the DP and IL cases tend to increase shear force above the shear force measured in the neutral state. The DL and IP cases tend to decrease shear force below the shear force measured in the neutral state. With an informed choice of actuation case, the adaptive fingerpads can be used to tune friction at the grip interface.

Effect of Fingerpad and Target Block Material

Following the initial characterization of the impact of fingerpad actuation pressure and timing on shear force using PTFE against PVC-covered fingerpads, a smaller set of actuation pressure levels was used to test a larger set of fingerpad and target materials. Three actuation pressure levels were tested for the five actuation cases: -40 kPa (DL or DP), 0 kPa (N), and 40 kPa (IL or IP). Three main sets of adaptive fingerpads were tested:

1. the PVC-covered fingerpads that were used to test normal force and the effect of fingerpad actuation on the shear force
2. 3D-printed resin fingerpads with a flat surface
3. 3D-printed resin fingerpads with sawtooth microtopography on the surface of the active regions

For some tests, the stock fingerpads and/or a mismatched pair of fingerpads (with a stock fingerpad on one finger and a PVC-covered adaptive fingerpad on the other) were also used.

Both target blocks (bare plywood and PTFE-covered plywood) were used during shear testing of PVC-covered fingerpads. During testing of printed fingerpads, only the PTFE-covered plywood block was used, as the forces applied on the bare plywood block by the printed fingerpads exceeded the force gauge capacity.

Typical force curves for various tests using these actuation cases, fingerpads, and target blocks are shown in Figure 7.11. The peak (maximum) and average steady-state (mean) shear force values for all actuation cases are reported for each fingerpad-block pairing in Table 7.3.

Actuation cases: Among the five actuation cases, only the cases involving an inflated state (IL, IP) noticeably impacted shear friction forces compared to the neutral (N) case. By contrast, the cases involving a deflated state (DL, DP) did not substantially differ from the neutral (N) case. In the IL case, a gripped block generally experienced higher shear forces. In the IP case, a gripped block generally experienced lower shear forces. These trends match the characterization results: higher contact area and normal pressure in the IL case yields higher friction whereas lower contact area in the IP case yields lower friction. The change in friction forces between the IL and IP cases is substantial: the average shear force in the IL case is $1.7\times$ to $2.6\times$ higher than the average shear force in the IP case depending on the specific fingerpad-block combination used.

Inflated cases by material: For both the PVC fingerpads and the printed fingerpads, the IP case always results in significantly decreased shear force. However, the IL case is not as consistent across fingerpad materials. For the PVC fingerpads, the IL case yields significantly higher shear forces for both target blocks, but for the printed fingerpads (especially those with the sawtooth microtopography), the IL case appears to yield forces similar to those measured in the N, DL, and DP cases. Overall, it is clear that inflation can substantially impact friction at the grip interface.

Flat versus sawtooth surfaces: The magnitudes of the shear forces measured for the flat printed fingerpads and the sawtooth fingerpads are fairly similar overall, suggesting that (at least for the surface substrate and microtopography geometry used in these experiments) the presence of microtopography does not substantially increase friction. Interestingly, the IL, N, DL, and DP cases are much more similar to one another for the printed fingerpads with sawtooth microtopography than they are for the flat printed fingerpads. This is surprising—if the presence of the sawtooth features had any impact on friction at the interface, one would expect that deflating the active regions (and thereby pulling the sawtooth features away from a gripped object) would change the shear forces experienced by a sliding object. Specifically, one would expect the shear forces to be lower in the DL and DP cases than in the IL and N cases.

There are multiple possible explanations for the apparent lack of connection between microtopography and friction, but the most likely cause in this case is the thick substrate and soft material of the printed surfaces. The printed surfaces are much thicker and stiffer than the PVC surface, and so the deflection of the printed surfaces is less apparent than that of the PVC surface. Deflating the printed surface to -40 kPa may not deflect the surface enough to fully retract the sawtooth features, resulting in similar frictional behaviour in the DL and DP cases compared to the N case. The low shear forces in the IL case could be the result of the sawtooth features contacting the gripped object first, preventing the base substrate from fully contacting the object between the features and thereby reducing the overall contact area. It is also possible that the soft material used to print these fingerpads compresses too easily—if even the flat fingerpads can interlock with asperities on the surface of the gripped object, the presence of microtopography may not further increase interlocking. Further testing is required to conclusively explain these results.

Neutral case by material: Finally, to evaluate the impact of fingerpad and target material in isolation (i.e., without fingerpad actuation), different fingerpad-target combinations were also tested and compared in their neutral states. These combinations included some tests performed
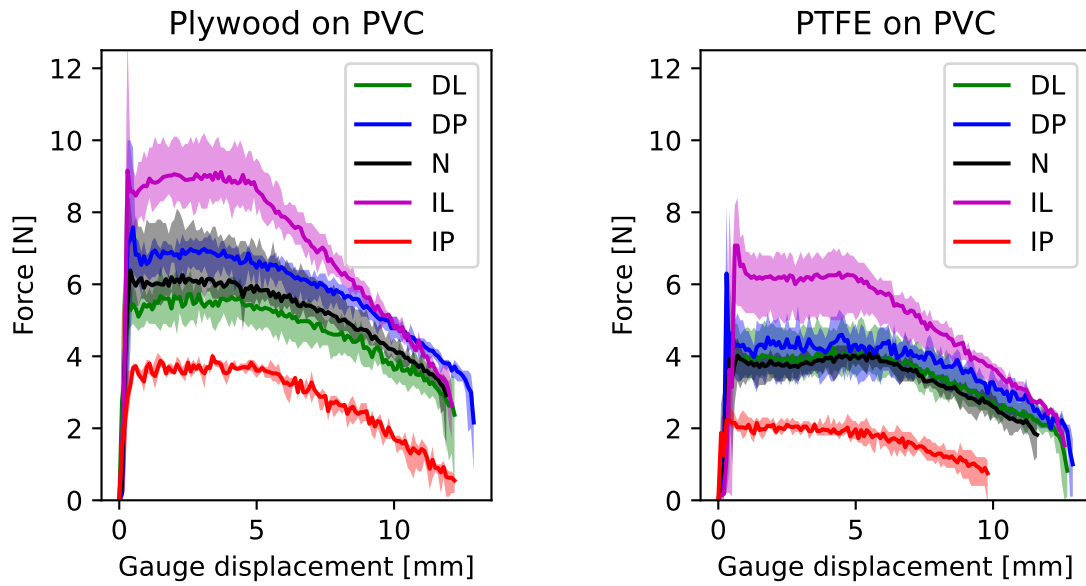
(a) Shear force when gripping a bare plywood block with PVC fingerpads. Forces in the IL and IP cases are significantly higher and lower (respectively) than others. Other cases (DL, DP, N) generally overlap.

(b) Shear force when gripping a PTFE-covered block with PVC fingerpads. Again, IL forces are much higher and IP forces are much lower. DL, DP, and N have slightly more overlap than in (a).
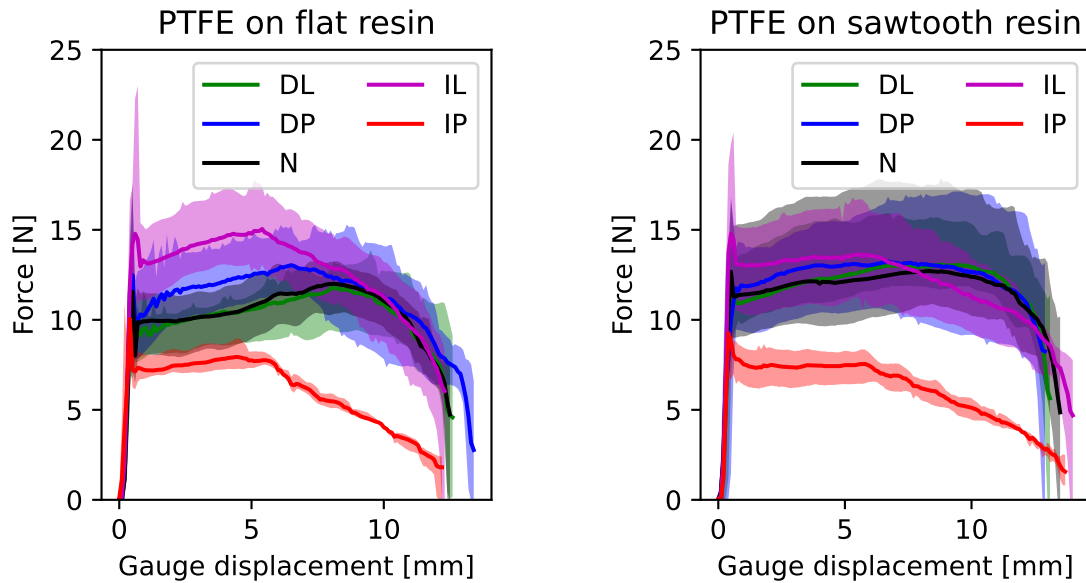
(c) Shear force when gripping a PTFE-covered block with flat printed (resin) fingerpads. Unlike (a) and (b), the IL case overlaps heavily with the other cases, but the IP case is still significantly lower-force.

(d) Shear force when gripping a PTFE-covered block with printed (resin) fingerpads with sawtooth micro-topography. Most actuation cases overlap— only the IP case stands out with lower forces.

Figure 7.11: Shear force vs. gauge displacement when gripping test blocks with different fingerpad combinations and using different actuation cases. Each plot shows force data for one fingerpad-block combination. For each actuation case, the shaded region is the area covered by force curves from 3-6 different trials and the solid line is the average of these curves.

Table 7.3: Average (F_a) and peak (F_p) shear forces for gripper tests using different fingerpads, target blocks, and actuation cases. For each fingerpad-block combination, the ratio of F_a to the average force for the neutral case (F_0, in blue) is provided. Each average force value is the mean of mean forces from 3* trials. Similarly, each peak force value is the maximum of maximum forces from 3* trials. Per-trial maxima were computed using all force measurements and per-trial mean values were computed using measurements from a 2 second interval in which the block was sliding steadily. *Data from 3 trials were available for all tests except for the test of the DP case for a plywood block on one PVC fingerpad and one stock fingerpad, for which only 2 trials were completed.

| Fingerpads	Target	Case	P [kPa]	F_a [N]	F_p [N]	F_a/F_0
Stock	Plywood	N/A	N/A	7.7	19.1	N/A
Stock	PTFE	N/A	N/A	6.8	12.3	N/A
PVC	Plywood	DL	-40	5.3	6.4	0.91
PVC	Plywood	DP	-40	6.9	10.0	1.19
PVC	Plywood	N	0	F_0=5.8	8.7	1
PVC	Plywood	IL	+40	9.4	14.1	1.62
PVC	Plywood	IP	+40	4.4	9.2	0.76
PVC	PTFE	DL	-40	3.3	6.8	0.85
PVC	PTFE	DP	-40	4.3	8.7	1.10
PVC	PTFE	N	0	F_0=3.9	4.8	1
PVC	PTFE	IL	+40	5.2	10.5	1.33
PVC	PTFE	IP	+40	2.0	4.3	0.51
PVC and stock	Plywood	DL	-40	7.8	15.0	0.83
PVC and stock	Plywood	DP	-40	9.4	18.9	1
PVC and stock	Plywood	N	0	F_0=9.4	18.1	1
PVC and stock	Plywood	IL	+40	12.9	17.5	1.37
PVC and stock	Plywood	IP	+40	7.5	17.4	0.80
PVC and stock	PTFE	DL	-40	4.9	10.5	1.11
PVC and stock	PTFE	DP	-40	5.3	9.3	1.20
PVC and stock	PTFE	N	0	F_0=4.4	7.9	1
PVC and stock	PTFE	IL	+40	7.0	13.9	1.59
PVC and stock	PTFE	IP	+40	3.0	5.8	0.68
Resin (flat)	PTFE	DL	-40	10.7	13.9	1.08
Resin (flat)	PTFE	DP	-40	13.5	16.9	1.36
Resin (flat)	PTFE	N	0	F_0=9.9	14.4	1
Resin (flat)	PTFE	IL	+40	14.0	23.0	1.41
Resin (flat)	PTFE	IP	+40	7.8	10.9	0.79
Resin (sawtooth)	PTFE	DL	-40	11.1	14.1	1.08
Resin (sawtooth)	PTFE	DP	-40	14.9	17.1	1.45
Resin (sawtooth)	PTFE	N	0	F_0=10.3	14.2	1
Resin (sawtooth)	PTFE	IL	+40	15.0	20.4	1.46
Resin (sawtooth)	PTFE	IP	+40	8.2	12.8	0.80
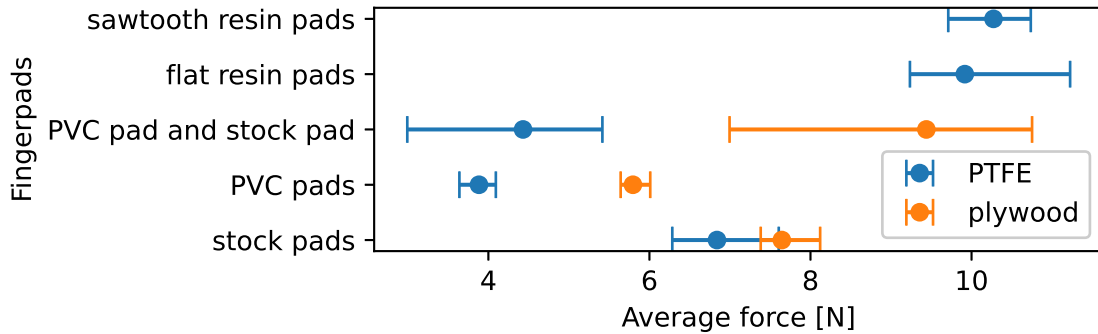
Figure 7.12: Comparison of mean shear forces experienced by target blocks during steady-state sliding for different (neutral) fingerpad surfaces. For each fingerpad-target combination, shear force was tested in 3 trials. For each trial, the mean of the forces measured during steady-state sliding was computed. This plot shows the range (bar length) and average (dot position) of the per-trial mean force values.

on the gripper's stock fingerpads. The average steady-state shear forces for each fingerpad-target combination are shown in Figure 7.12, and the full force curves used to obtain these average forces are shown in Figure 7.13. Across materials:

- The PVC fingerpads applied the lowest shear forces and their range for each target block was relatively small, indicating consistent frictional behaviour.
- The printed fingerpads applied the highest shear forces. The force ranges were smaller for the sawtooth pads than for the flat pads, indicating that the results for the sawtooth pads were more consistent.
- The stock fingerpads were the most consistent across target block materials, with the force range for the PTFE target block overlapping with that of the plywood target block.
- The pairs with one PVC fingerpad and one stock fingerpad were the least consistent across target materials and their range for each target block was quite large.

Since only a small amount of data were available for the printed fingerpads, data from 3 trials were used for each bar in Figure 7.12. The results thus may not be completely representative, and more data should be collected to confirm these initial conclusions.

7.4 Demonstration: Pressure-Based Object Detection

Following the quantitative characterization of the adaptive fingerpads, the PVC-covered fingerpads were also used for more qualitative testing and demonstration. One particularly interesting feature of pneumatic fingerpads is their suitability for morphological computation approaches. The internal pressure of pneumatic fingerpads can be both controlled and read, and pressure sensor feedback can be used to draw conclusions about grip conditions.

For instance, Pozzi et al. [150] recently showed that a simple object detection scheme can be implemented using pressure feedback from inflatable fingerpads. If a fingerpad is inflated prior to gripping an object, its initial volume, V_0, decreases to $V < V_0$ when the object contacts and
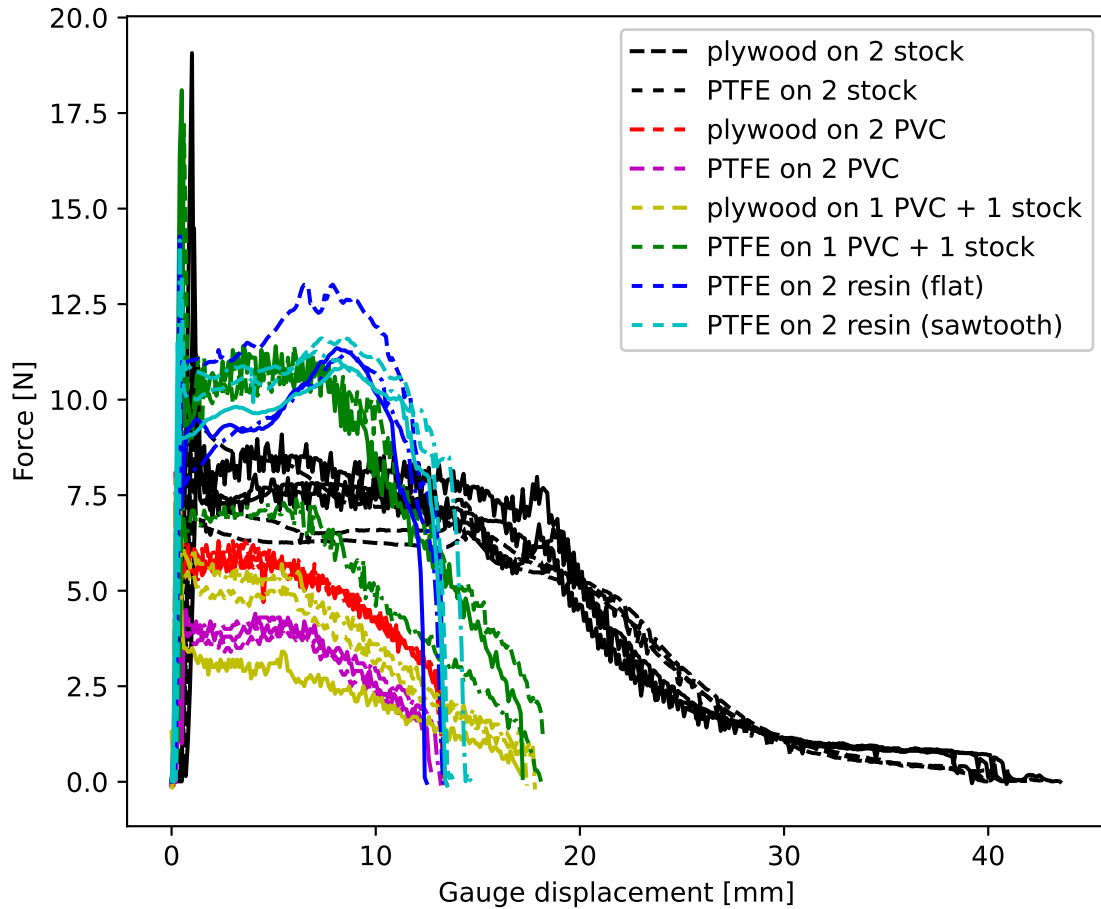
Figure 7.13: Shear force on target blocks when gripped using various different (neutral) gripper fingerpad pairs. The mismatched gripper fingerpad pair (1 PVC fingerpad and 1 stock fingerpad) produces the most variable force data. The evenly matched pairs of gripper fingerpads generally produce more consistent data—for instance, the tests run with 2 PVC fingerpads produce force curves that are clearly clustered. Resin fingerpads produce the highest shear forces and PVC fingerpads produce the lowest shear forces. In general, for a given fingerpad pair, the PTFE target will experience lower shear forces than the plywood target. The stock finger data cover a larger domain because the geometry of these fingerpads and the force gauge used for this set of tests enabled target blocks to be placed deeper inside the grasp workspace.

compresses the inflated regions. Per Boyle's Law, $P_0V_0 = PV$ when temperature is constant. The initial fingerpad pressure P_0 will hence increase to $P > P_0$ on contact with the object. This sudden increase in pressure can be interpreted as a crude object detection signal. If multiple such pressurized chambers are monitored independently, object motion can also be sensed (e.g., to detect slipping) by detecting pressure changes that shift from one chamber to another (as demonstrated recently by Laqua [174] and by He et al. [151]).

7.4.1   Test Procedure

To demonstrate object detection using pressure feedback, objects were gripped using inflated fingerpads while recording both the internal pressure of the fingerpads and the object detection status of the gripper. Since closed-loop pneumatic control of the fingerpads quickly corrects abnormalities in internal pressure, this test was conducted without pressure regulation. To do this, pressure regulation was disabled after the fingerpads were inflated, leaving the fingerpads as closed pressurized vessels for the duration of the test.

7.4.2   Results and Discussion

The gripped object (a plastic tube) and the data collected during object contact are shown in Figure 7.14. When the fingerpads contacted the tube, their internal pressure began to rise immediately. The gripper's object detection flag was set after 0.27 seconds, by which time the fingerpad pressure had already noticeably increased. This demonstration shows that inflated fingerpads can be used for pressure-based object detection. Furthermore, depending on the threshold pressure step needed, this proprioceptive pressure-based object detection approach can be faster than the 2F-85 gripper's built-in object detection.

   One limitation of this approach is the conflict between pressure monitoring for object detection and routine fingerpad pressure regulation. Disabling regulation facilitated detection of the changes in fingerpad pressure caused by object contact. However, since the pneumatic controller uses fittings that leak air quickly, disabling regulation also led to steady pressure losses over the course of this test (shown in Figure 7.15). This drawback can likely be mitigated by increasing the pressure regulation cycle time such that sudden pressure changes could be detected *before* the pressure is adjusted, avoiding ambuiguity around the source of pressure changes; more experimentation is required to confirm that this solution would enable ongoing regulation during object detection routines. The pneumatic controller fittings could also be replaced with more airtight fittings to permit temporary suspension of regulation without significant air losses.

7.5   Demonstration: Interlocking and Enveloping

In addition to (quantitatively) analyzing the microscale effects of fingerpad actuation on surface properties, the macroscale effects of the local morphology changes in the fingerpad surface were also investigated (using a qualitative approach). Shape adaptation is a desirable property in grippers because a grip surface that matches or complements the shape of a gripped object enables mechanical interlocking and/or enveloping. These macroscale interactions between the grip surface and a target surface can drastically improve grip strength.
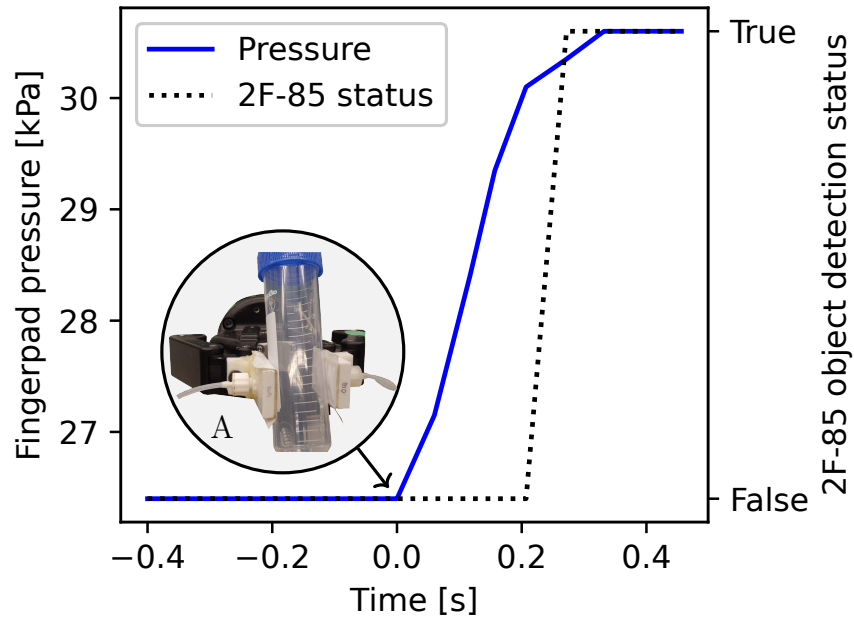
Figure 7.14: Change in fingerpad internal pressure and 2F-85 gripper object detection status while gripping a centrifuge tube. The pressure begins to increase well before the 2F-85 detects the gripped object. Inset A shows the gripped tube, with an arrow indicating the point at which the gripper comes into contact with the tube.
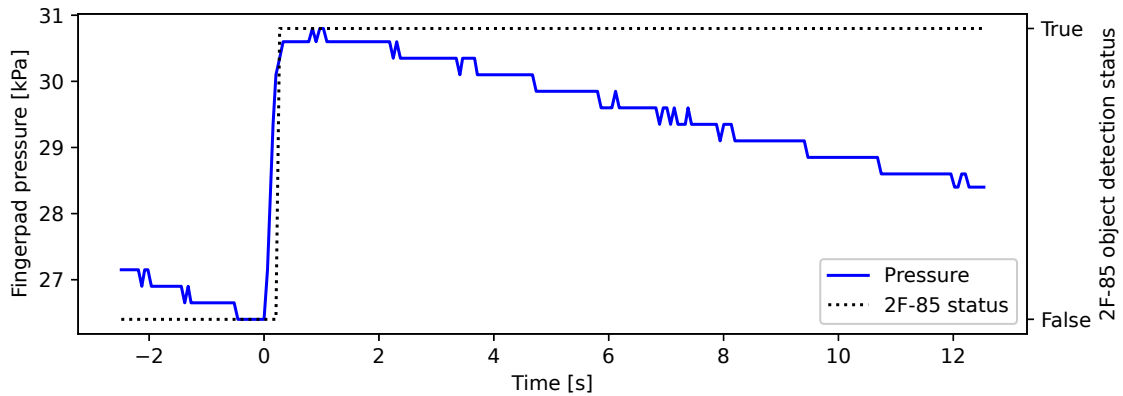

Figure 7.15: Using the current pneumatic control settings, the increases in fingerpad internal pressure that occur when an object is gripped are only unambiguously detectable when the fingerpad pressure is unregulated. In this state, due to air leakage at connection points in the pneumatic apparatus, the internal pressure of the fingerpads rapidly drops over time. When the fingerpad pressure data are viewed over a longer duration (e.g., over ∼14 seconds here rather than ∼1 second as in Figure 7.14), the declining fingerpad pressure becomes noticeable.

In this experiment, interlocking and enveloping interactions between the PVC-covered adaptive fingerpads and various compatible objects were qualitatively demonstrated by gripping objects and examining the grip interface.

7.5.1   Test Procedure

Since this demonstration was qualitative in nature, the test procedure was simple: objects were gripped using either inflated or deflated fingerpads (depending on the expected interactions with a particular object) and then photographed. Some sample gripped objects are shown in Figure 7.16.
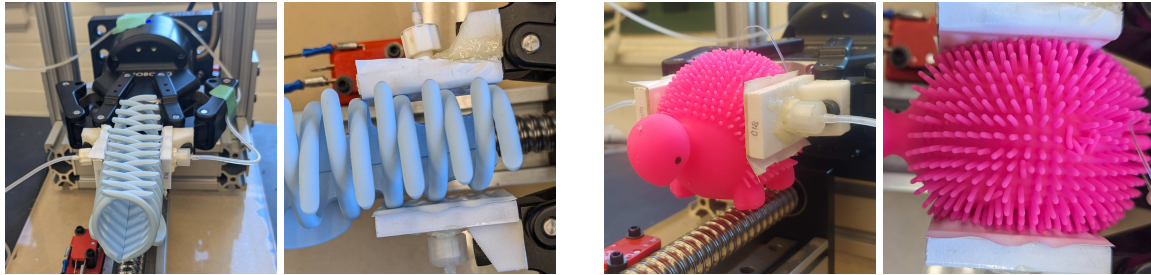
(a) Hair accessory with deflated fingerpads.   (b) Fluid-filled toy with inflated fingerpads.

Figure 7.16: Sample objects interacting with actuated gripper fingerpads. Interestingly, the grip on the fluid-filled toy was so light that the gripper's built-in object detection status never changed (i.e., the object detection flag remained at False for the duration of the grip on this toy)—indicating that the normal forces on the toy are low, and hence that the shear forces keeping the toy from slipping are likely to be the result of effective friction and adhesion more so than high normal forces.

7.5.2   Results and Discussion

Both interlocking and enveloping behaviours were demonstrated during this stage of gripper testing. When gripping objects with protrusions (e.g., a cannula fitting flange or a bolt head), the adaptive fingerpads were deflated to facilitate interlocking. When gripping small convex objects (e.g., a chocolate ball or a hex nut), the adaptive fingerpads were inflated to facilitate enveloping.

(a) Interlocking between flange of cannula fitting (green) and deflated fingerpads.

(b) Slight enveloping of foil-wrapped chocolate ball (orange) by inflated fingerpads.

Figure 7.17: Pictures of interlocking and enveloping behaviour viewed from above.

Interlocking: A cannula fitting was gripped with deflated fingerpads as shown in Figure 7.17a. The protruding edges of the fitting interlocked with the recessed areas of the fingerpad, increasing contact area at the grip interface. The direction of the forces experienced by the fitting during shear testing also changed compared to the neutral case. In the neutral case, the fitting nominally experienced only *shear* forces (as in Figure 7.18b). When interlocking, however, the fitting partially contacted internal faces of the active regions, producing increased *normal* forces (enhanced by the elastic response of the material compressed by the fitting during shear loading) that directly resisted the shear force applied to the fitting during testing (as in Figure 7.18a).
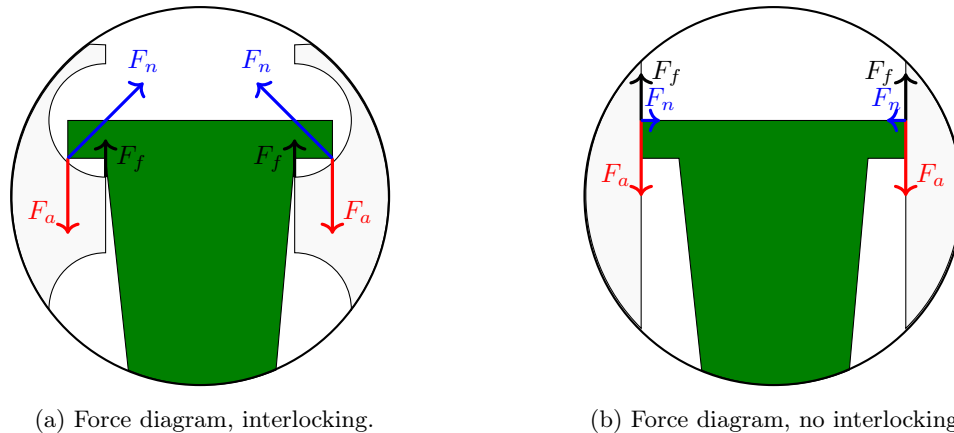

(a) Force diagram, interlocking.   (b) Force diagram, no interlocking.

Figure 7.18: With interlocking, applied force (F_a) pulling the fitting from the gripper is resisted by both normal (F_n) and shear (F_f) forces.

Enveloping: A small ball was gripped with inflated fingerpads as shown in Figure 7.17b, thereby increasing contact area by filling in gaps between the curved object surface and the flat pad surface.

7.6   Discussion

This chapter has characterized the extent to which actuating adaptive fingerpads can tune friction at the grip interface using active region deflection. This section summarizes the main results and discusses limitations and next steps.

7.6.1   Main Results

The four gripper-based experiments discussed in this chapter have characterized the impact of adaptive fingerpad actuation on normal and shear grip forces, demonstrated the sensory capabilities of these fingerpads, and shown that they can be used to interlock with or envelop compatible objects. The main results from these experiments are summarized in the following list.

- In general, inflating fingerpads before gripping (IP) decreases shear forces (but not normal forces) compared to neutral fingerpads, whereas inflating after gripping (IL) increases both normal and shear forces—meaning that the timing of actuation relative to gripping drastically impacts surface adaptation results, at least for the Robotiq 2F-85 gripper.

- Printed fingerpads with sawtooth microtopography have similar frictional properties to flat fingerpads made from the same material, indicating that the presence of sawtooth microtopography did not significantly impact friction.

- Adaptive pneumatic fingerpads can be used for object detection, and this pressure-based proprioceptive detection can be faster than the 2F-85 gripper's force-based object detection.

- In general, deflation does not meaningfully change the fingerpads' micro-scale frictional properties. However, it *does* cause changes in local surface morphology that enable useful macroscale grasping interactions such as interlocking and enveloping.

Overall, these experiments have shown that adaptive fingerpads can tune friction at the grip interface. They have also shown that the range of shear forces experienced for different actuation states varies depending on the fingerpad material, and that the role of surface microtopography is minor. Interestingly, the significant changes in shear friction forces that accompanied deflation for flat devices (as described in Chapter 6) were not observed with fingerpad devices.

Shear forces can be increased effectively and consistently by inflating adaptive fingerpads, and shear force increases are accompanied by relatively small increases in normal force. This improved shear-normal force ratio could reduce the risk of damage to delicate objects by lowering the risk of object slip while avoiding applying excessive grip pressure.

All adaptive fingerpad surfaces tested in this chapter would be suitable for friction tuning during gripping, but in different circumstances. The PVC device is useful when lower overall friction is acceptable and when multiple distinct friction levels are needed (since its IL and IP forces are drastically different from its forces in the N case). The printed devices are useful when higher overall friction is needed and when it is acceptable to have only one actuation case that noticeably impacts friction (since the IP case is the only case for which friction changes significantly, and all other cases overlap).

The impact of actuation timing on friction is a particularly interesting and unique result. Previous friction-tuning grip surfaces in the literature have not tested the effect of varying actuation timing. It is important to note that this relationship between actuation timing and friction is likely an artefact of the behaviour of the Robotiq 2F-85 gripper. When this gripper closes, it stops once reaction forces from an object are detected. This means that the IP case (where the active regions are protruding and contact the object first) will grip with a larger finger separation distance than the IL case. However, even if this relationship is specific to the Robotiq 2F-85 gripper, it can be replicated on other grippers if desired by slightly increasing the target finger separation distance used in the IP case. It is difficult to determine the exact reason for the lower friction in the IP case, but it is likely the result of both the larger gripper finger separation distance and a reduced overall contact area.

7.6.2   Limitations and Next Steps

Many of the experiments discussed in this chapter used data from a small set of trials due to time constraints and delays caused by malfunctioning equipment. To confirm the key results listed above, more data should be gathered for many experiments. In particular, both normal and shear force tests should be repeated with a variety of grippers. The Robotiq 2F-85 gripper's regrasp feature prevents
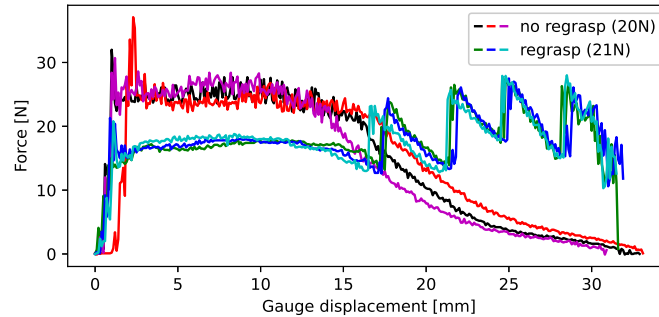
Figure 7.19: Shear force on a bare plywood block when gripped with the stock gripper fingerpads with and without the regrasp functionality. Regrasping is disabled when the nominal grip force is set to 20N and enabled when force is set to 21N or higher. Notice the periodic increases in force as the gripper attempts to regrasp the sliding block.

grip force from being used as a control parameter in shear testing because repeated grasp adjustment produces periodic force curves (shown in Figure 7.19) that make data analysis challenging. To both improve the generality of the results and enable testing at a range of constant grip forces, gripper experiments should be repeated on a second gripper that does not have regrasp functionality.

Similarly, the small set of data collected for (a single type of) printed microtopography should be greatly expanded. The initial adhesion challenges encountered with the printed surfaces (described in Section 4.4) prevented these printed surfaces from being tested until very close to the end of experimental work. As a result, only one type of microtopography (sawtooth features) could be tested and only 3 trials could be conducted for each test. Once the adhesion challenges have been fully resolved, design and fabrication of fingerpads with printed surfaces will be fast and simple (since 3D printing is a comparatively low-effort fabrication method). A larger set of different microtopography surfaces should be assembled into fingerpads, and these fingerpads should be used to gather substantially more data. When more data are available, more detailed analysis of the role of microtopography in multi-level surface adaptation for robotic gripping will become possible.

Chapter 8

Conclusion

In this work, a practical multi-level adaptive grip surface was designed and characterized, demonstrating that the surface can actively tune friction at the grip interface. This thesis has shown that layered adaptive surface devices with a thin top layer actuated by subsurface pneumatic chambers can be fabricated using standard digital fabrication equipment. Moreover, microtopography surfaces can be effectively fabricated using a 3D printer provided that their feature size is on the order of 10-100 microns. Since each layer of an adaptive surface device is relatively simple, devices can readily be repaired or customized—in particular, in many cases, the active region geometry can be completely changed by replacing the top two layers without the need to change the base layer (which is the most complex layer to fabricate). Using this design, pneumatic pressure can deflect the top surface in active regions that are clearly defined by the middle layer. Furthermore, most devices are robust and can be used repeatedly for shear force testing under shear loads exceeding 20 N—indicating that they can be used for many cycles in typical low-force grip conditions. This thesis aimed to address the following research questions:

RQ1 How does multi-level active surface adaptation influence shear grip strength and shear friction?

RQ2 How does the order of operations when using multi-level surface adaptation in a gripping process impact grip friction?

RQ3 Can we leverage knowledge of the pressure in the pneumatic chamber to draw conclusions about changing grip conditions?

RQ4 Can we use grip surface adaptation to facilitate macroscale grip interactions like interlocking and enveloping?

8.1 Main Findings

The main findings listed below (grouped by research question) summarize the experimental work discussed previously.

RQ1 As expected, inflating the active regions after gripping an object (IL case) tends to increase grip forces (both normal and shear) compared to the neutral case. Deflating the active regions after gripping an object (DL case) does decrease normal grip forces; however, contrary to

the initial hypothesis, deflation does not noticeably decrease friction forces, and sometimes even slightly increases friction compared to the neutral case (e.g., for the sawtooth surface). Surprisingly, adding microtopography during grip testing did not change frictional properties compared to a flat surface of the same base material—this contradicts the initial hypotheses that microtopography would increase friction and that inflated microtopography surfaces would experience particularly high friction due to synergy.

RQ2 The inflated-live (IL) case always produces higher shear forces than the inflated-prior (IP) case. This is likely at least partially an artefact of the specific gripper used during testing— since the gripper stops closing its fingers when object contact is detected, there is a difference in the finger separation for the IL case versus the IP case.

RQ3 Gripping an object with inflated active regions creates a sharp rise in fingerpad internal pressure, and this spike in pressure can be used as an object detection flag. This method can be used to obtain a object detection signal more quickly than the built-in object detection feature of the Robotiq 2F-85 gripper used during testing.

RQ4 For certain objects of compatible size, inflating or deflating the active regions of the grip surface can produce visible interlocking or enveloping interactions.

The adaptive grip surface design is limited in its friction tuning range. While the continuous top layer used in this design improves robustness compared to designs with multiple contact layers (e.g., that of Becker et al. [55]) by reducing the risk of snagging, using a single contact layer also limits friction tuning. Since actuation only changes the *morphology* of the contact surface rather than completely swapping contact surfaces, the range of friction force variance seen during grip testing is lower than that of designs that use separate high-friction and low-friction contact surfaces. However, the greater number of control states available and the ease of fabrication and repair make this adaptive grip surface far more practical for general robotic gripping applications. Moreover, the frictional properties of an adaptive grip surface with a continuous top layer and multiple inflatable active regions have not been explored in the literature—meaning that the experimental work conducted in this thesis expands the frontier of knowledge for surface adaptation.

8.2 Future Work

The multi-level adaptive grip surface design introduced in this work is simple to manufacture and customize, and the small set of design parameters explored in Chapter 6 and Chapter 7 only scratches the surface of the many possible interesting microtopography surfaces that could be investigated. As such, most suggested next steps involve extending the design space to explore more active region geometries, microtopography types, surface substrates, and channel layouts.

The designs tested in this work all used rectangular active regions. Other active region layouts that were partially designed or fabricated, but that could not be tested in time, included arrays of circular active regions as well as rows of active regions in which the region width increased from one side of the device to the other. Roberge et al. used a chevron arrangement for their microwedge-based adaptive adhesive devices [24]—this could also be an interesting active region layout or microtopography layout to explore further.

A limited set of microtopography shapes (pyramids, ridges, and sawteeth) were explored in this work. Microtopography surfaces that were partially designed or fabricated but not fully tested included a commercially available gecko-inspired adhesive micropillar surface with mushroom tips, a custom-printed surface with short pillar shapes, and a custom-printed surface with angled ridges (chevron shapes). To better compare our results to those of others, it would be beneficial to also test devices that use more common microtopography shapes like tall pillars or angled wedges.

Similarly, a limited set of surface substrates (PTFE, Trizact™, PVC, and FormLabs Elastic 50A V1 resin) were explored in this work. The resin surfaces should be the next surface substrate to be modified because, at their 0.5 mm thickness, they did not easily deflect under pneumatic pressure—these surfaces likely can and should be printed with a lower thickness. It could also be informative to test different substrates entirely—e.g., the printed resin microtopography could be compared against moulded elastomer surfaces, or against different commercially available surfaces.

All devices tested in this work used a single pneumatic input channel. Previous work from Laqua [174] tested multichannel microtopography-covered pneumatic smart surfaces (designed for adaptive adhesion) and found that actuating different regions of the surface in sequence could translate small objects, and that pressure feedback from each channel could be used to gather information about local conditions in the corresponding region. Similarly, multichannel inflatable surfaces have been used as two-dimensional tactile sensing arrays by Gaudeni et al. [152]. In the context of adaptive grip friction, a similar approach could be taken using multichannel adaptive grip surfaces for more complex actuation and sensing. For instance, multichannel grip surfaces could potentially be used to detect object sliding based on changes in relative channel pressures, to arrest object sliding by inflating active regions, or to manipulate objects in-hand using sequential channel actuation events. A simple next step could be to fabricate a dual-channel surface with one channel controlling active region strips oriented parallel to the object sliding direction (with these strips located closer to the fingerpad base) and another channel controlling a set of perpendicular active region strips (located closer to the fingerpad tips).

Other suggested future work could make the fabrication process even simpler. For instance, most gripper fingerpad alignment problems stem from imprecise epoxy-based adhesive joints between the fingerpad base and its mounting piece. This issue could be eliminated by fabricating the fingerpad base and its mounting piece from a single piece of stock material—e.g., by 3D-printing the unit or by using a two-step CNC process. Similarly, delamination issues (the most common failure mode for adaptive grip surfaces) could be ameliorated by improving the strength of the adhesion between the top layer and the middle layer or by adding a rigid middle layer for additional support (e.g., the adhesive middle layer could be placed on top of a laser-cut piece of acrylic of the same shape, eliminating the need for milled channels in the base layer and allowing the base layer to simply have a single open interior).

Other avenues for future work could extend shear testing and grip behaviour demonstrations. A larger variety of target object materials and shapes could be used in shear testing. In particular, the impact of enveloping and interlocking behaviours on shear force test results should be investigated by testing target objects with cavities or protrusions of compatible size. Object detection using pressure feedback should also be explored in more depth. Reducing the pressure regulation control rate would allow object detection to be implemented without disabling regulation, particularly if the pneumatic controller is adjusted to continuously monitor for steps in fingerpad pressure. If

multichannel devices are fabricated, the object detection feature could be extended for more general contact sensing—e.g., comparing pressure data across different channels could allow the placement of objects relative to the fingerpads to be determined, or enable slip detection. Multichannel devices could also be used to gather shear force data using a larger set of possible actuation cases—e.g., by actuating different channels at different times in the grip and test process.

Robotic gripper technology is evolving rapidly, with innovative soft and hybrid rigid-soft gripper designs enabling increased versatility and adaptability. The fabrication and experimental work conducted for this thesis sets the stage for more comprehensive testing of different adaptive grip surface designs and their capabilities. The incorporation of adaptive grip surfaces has the potential to address the versatility challenge by improving control authority and increasing dexterity in manipulation tasks, and perhaps to help robotic gripping become more useful in daily life.

Appendix A

Baseline Friction Force Results

Early in experimental work, baseline testing was conducted to validate the experimental procedure outlined in Chapter 5, evaluate initial candidate surface designs, and establish a set of baseline data to compare against early test data. Before testing flat devices with an upper constraint limiting the position of the test sled (i.e., with a dual constraint) as described in Chapter 6, flat devices were tested without an upper constraint and with the test sled sliding freely on a flat piece of material or on the device surface. The results of this baseline flat device testing are summarized in Section A.1. Similarly, before testing fingerpad devices as described in Chapter 7, the Robotiq 2F-85 gripper's stock fingerpads were used to gather some initial baseline data against which to compare the adaptive fingerpad data. The results of this baseline gripper testing are summarized in Section A.2.

A.1 Baseline Tests for Flat Devices

Baseline testing for flat devices aimed to both validate the overall experimental procedure and examine an initial set of candidate adaptive surface designs.

A.1.1 Test Procedure

This experiment series followed the shear test procedures outlined in Chapter 5 and Section 6.1.

Device and Sled Setup

Before each test, the device was secured to the test platform with its active regions either parallel (Figure A.1a) or perpendicular (Figure A.1b) to the direction of sled motion. To mount the device in a parallel orientation, bolts were inserted through the device's mounting holes (located near the pneumatic inlet) and then threaded into the test platform to pull the device snug against the platform. When the device was tested in a parallel orientation, it was always connected at the end of the test platform to consistently constrain its position relative to the starting position of the gauge. When the device was tested in a perpendicular orientation, its longer side length compared to the test platform width made its active regions off-centre when its mounting holes were used to connect it to the test platform directly. To remedy this, when in a perpendicular orientation, the device was placed on a 3D-printed connector (visible at the top of Figure A.1) to constrain its
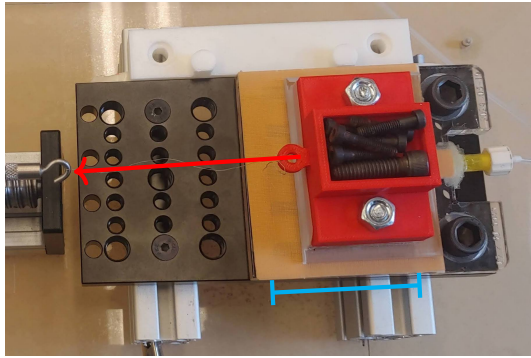
(a) Sled motion is parallel to active regions.   (b) Sled motion is perpendicular to active regions.
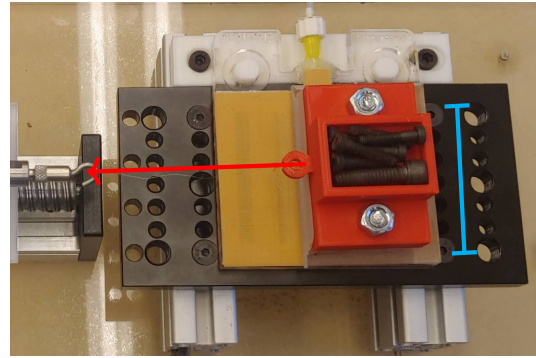
Figure A.1: Parallel and perpendicular device orientations for shear testing. The sled motion direction is indicated with a red arrow and the active region orientation is indicated with a cyan line.

Figure A.2: Baseline flat device test setup. The device is fixed to the test platform, which acts as a lower constraint. The sled rests freely atop the device and is pulled across the device by the gauge.

horizontal position while keeping the active region of the device top surface centered relative to the test platform. Clamps or double-sided tape were used to constrain the device's vertical position. Once the device was mounted, the test sled was massed, placed on the device, and connected to the force gauge as described in Section 6.1. The baseline test setup is pictured in Figure A.2.

Device Designs and Test Parameters

Shear tests measured the shear force experienced by a test sled sliding over an adaptive surface device. Two adaptive surface device designs were tested:

- A device with 2 mm wide strips as active regions and PTFE tape as the top layer. Since the PTFE tape was unpatterned, this device did not have surface microtopography.
- A device with 5 mm wide strips as active regions and Trizact sandpaper as the top layer. Since Trizact sandpaper is covered with small, hard pyramids arranged in a rectangular grid, this device did have (relatively large) surface microtopography.

For this series of tests, devices were tested in both the parallel orientation and the perpendicular orientation. Three different actuation pressures were used: -40 kPa for the deflated state, 0 kPa for the neutral state, and 40 kPa for the inflated state. For each combination of target sled material and device material, one test was conducted for each of the six different pressure-orientation
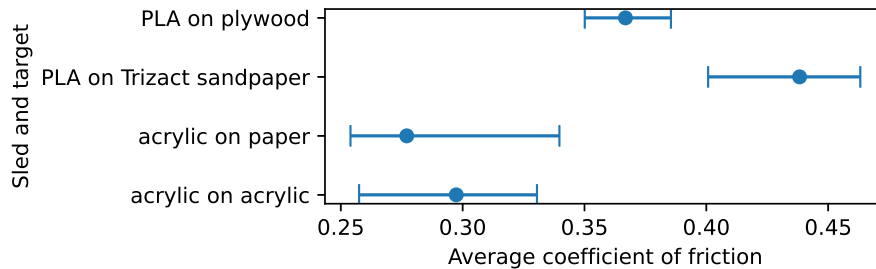
Figure A.3: Comparison of approximate effective coefficient of friction (eCoF) for acrylic- and PLA-based sleds with different stock sheets of material. For each combination of sled and stock materials, shear force was tested in 3-6 trials. The eCoF for each trial was computed by dividing the mean shear force measured during steady-state sliding by the sled mass and the gravitational constant. This plot shows the range (bar) and mean value (dot) of the per-trial eCoF values.

parameter pairs: parallel-deflated, perpendicular-deflated, parallel-neutral, perpendicular-neutral, parallel-inflated, and perpendicular-inflated. Three trials were run for each test, meaning that each sled-device pair was used in at least 18 trials in total.

A.1.2 Results and Discussion

This section presents results from two experiments:

1. The first experiment measured the force required to pull test sleds across *stock sheets of material* in order to verify the overall test process by gathering a baseline set of force data.
2. The second experiment measured the force required to pull test sleds across *adaptive surface devices* in order to evaluate the extent to which actuating the devices impacted force data.

For both experiments, the mean shear force (F_s, in N) from each trial was used to compute an approximate effective coefficient of friction (eCoF) between the sled and the sheet or device. To simplify computations, the eCoF at the interface between the sled and the device was computed using the Amonton-Coulomb law:

$$\text{eCoF} = \frac{F_s}{mg} \tag{A.1}$$

where m is the mass of the test sled in kg and g is the gravitational constant. Since in reality the adaptive surfaces are generally not well-described by this law, the eCoF results are not meaningful on their own and should only be used to make relative conclusions by comparing across tests.

Stock Material Testing

To establish a baseline for the force testing procedure overall, a sled with a bare PLA base and a sled with an acrylic base were pulled across various flat stock sheets of material. Some sample eCoF value ranges computed based on force measurements from this baseline testing are shown in Figure A.3 (with the average eCoF for each range indicated with a dot).

The acrylic-paper interface had the lowest eCoF, followed by the acrylic-acrylic interface. The highest eCoF values were computed for the PLA-Trizact interface, followed by the PLA-wood interface. These relative results generally match expectations — interfaces involving highly textured
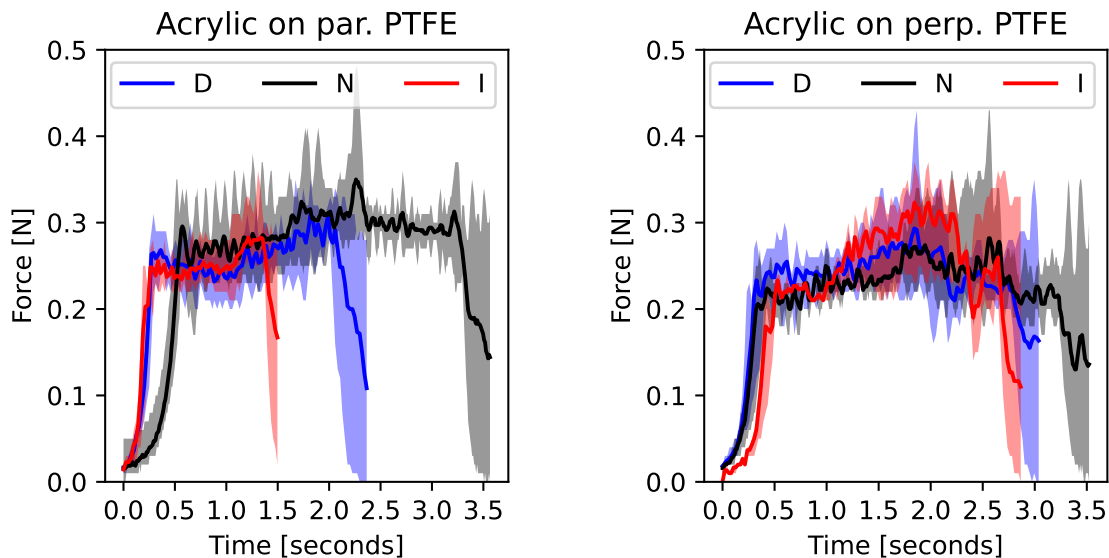
(a) Forces measured when the PTFE device was in the parallel orientation. The force curves for different actuation states largely overlap (with some differences in total duration that are likely the result of differing sled start positions).

(b) Forces measured when the PTFE device was in the perpendicular orientation. The force curves for different actuation states, as in (a), largely overlap other than a spike in the curve for the inflated state at $t = 2$.

Figure A.4: Shear force vs. time when pulling an acrylic-based sled across a PTFE device. Each plot shows force data from all actuation states for one device orientation. For each actuation case, the shaded region is the area covered by force curves from 4-6 different trials and the solid line is the average of these curves. The exception is the perpendicular-inflated test, for which only 2 trials were conducted. Legend entry D stands for deflated, N stands for neutral, and I stands for inflated.

and rough materials like sandpaper, 3D-printed PLA, and wood typically have higher coefficients of friction than interfaces involving smoother materials like sheet acrylic.

Effect of Actuation Pressure

If the actuation of an adaptive surface device changes its surface's effective coefficient of friction, there should be a difference in the average shear force measured for different actuation states.

By this heuristic, actuation of the PTFE device does not appear to meaningfully change shear forces experienced by a sliding block. The force-time data measured when pulling an acrylic-based sled across a PTFE device are shown in Figure A.4. For both device orientations, the force measurements collected when the device was in the deflated state overlap with the force measurements collected in the neutral and inflated states. For the perpendicular orientation, there is a slight increase in the average force for the inflated state compared to the neutral and deflated states (particularly at about two seconds into the test); however, the force curves for all three states overlap for the majority of the test, so this slight increase is not necessarily significant.

In contrast, for the Trizact device, actuation *does* appear to meaningfully change shear forces experienced by a sliding block. The force-time data measured when pulling an acrylic-based sled and a PTFE-based sled across a Trizact device are shown in Figure A.5. Compared to the PTFE device,

the data gathered using the Trizact device show significantly less overlap between the force-time series for the different actuation states. For the parallel orientation, tests in the inflated state show lower forces than tests in other states. In contrast, there is a clear increase in the force measured in the inflated state for the perpendicular orientation, although with different timing depending on the sled material—for the acrylic sled, the force increases near the start of the test, whereas the force increases only about halfway through the trial when the PTFE sled is used.

Quantitatively, these data suggest that the Trizact device's effective coefficient of friction is modulated by surface adaptation and that the PTFE device's effective coefficient of friction is not. Qualitative observations of the devices during testing suggest a possible explanation: the differing extent to which the surfaces of the two devices deflect in the active regions at the actuation pressures used in this experiment. The PTFE device's active regions are 2 mm in width, and the PTFE tape is quite thick at 0.21 mm. When the PTFE device is inflated or deflated, although the slight protrusions/recessed areas can be detected by touching the device, there is little to no *visible* change in the active regions. On the other hand, the Trizact device's active regions are 5 mm in width, and its surface deflection is easily detectable by eye or by feel. This difference in the extent to which the two device surfaces deflect could explain the difference in their shear force testing results—if the PTFE device's surface does not change significantly when pressurized, its frictional interactions would also not be expected to change significantly.

Effect of Device Orientation

The orientation of a device's active regions relative to the direction of sled motion can significantly change the way that the sled's leading edge interacts with the active regions. For both orientations, when the active regions are deflated, the contact area between the sled and the adaptive surface device should be lower on average than in the neutral case. However, in the parallel orientation, the sled consistently makes contact with the same geometry throughout most of its sliding, whereas in the perpendicular case it intermittently meets and passes the edges of the recessed active regions. Since the sled base is flat and the applied force should be roughly parallel to the adaptive surface, the sled should still slide across these edges smoothly in the perpendicular case. However, it is possible that the sled's leading edge could dip slightly when crossing a recessed active region and impact the inside of the active region—this would cause a local normal force opposing the global shear force.

When the active regions are inflated, the contact area between the sled and the adaptive surface will be lower when the device is in the parallel orientation. In this orientation, the sliding sled rests on and contacts only the raised active regions, and so its total contact area is lower compared to the neutral state. Since the active regions run parallel to the sled's motion, the sled maintains contact with the same set of raised regions for the duration of its sliding. In the perpendicular orientation, by contrast, the sliding sled makes and loses contact with the raised regions as it crosses them. This creates a slight rocking motion and can cause the leading edge of the sled to contact the front of a raised element, producing intermittent local normal forces that oppose the global shear force.

Based on the expected interactions between the sled and the active regions in these two orientations, shear forces experienced by the sled in the parallel orientation are expected to be lower in the inflated and deflated cases than in the neutral case. Shear forces experienced in the sled in the perpendicular orientation are expected to be (intermittently) higher in the inflated case than in the neutral case and (generally) lower in the deflated case than in the neutral case.
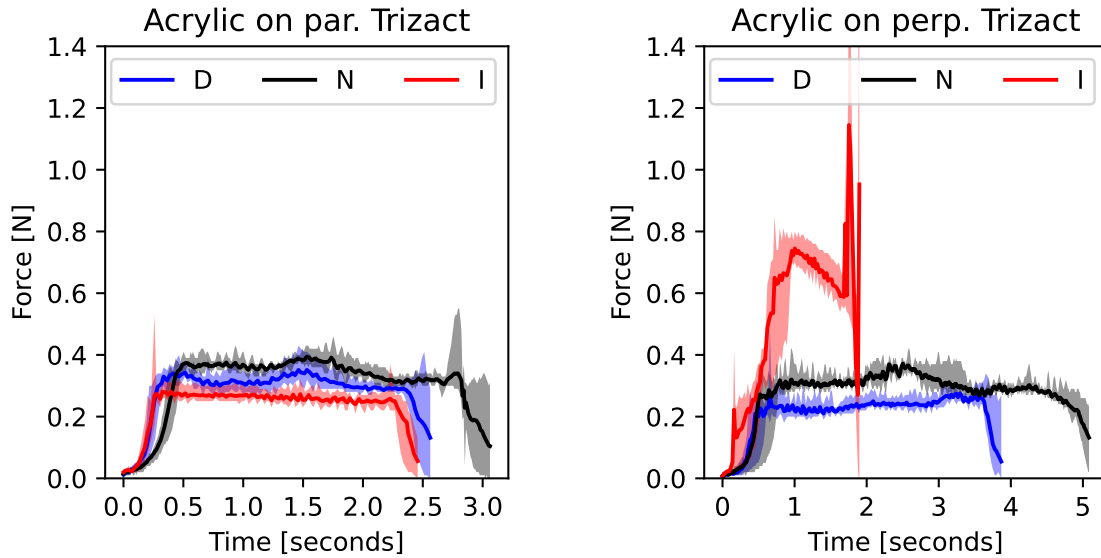
(a) Forces measured when the acrylic sled was pulled across the device in the parallel orientation.

(b) Forces measured when the acrylic sled was pulled across the device in the perpendicular orientation.
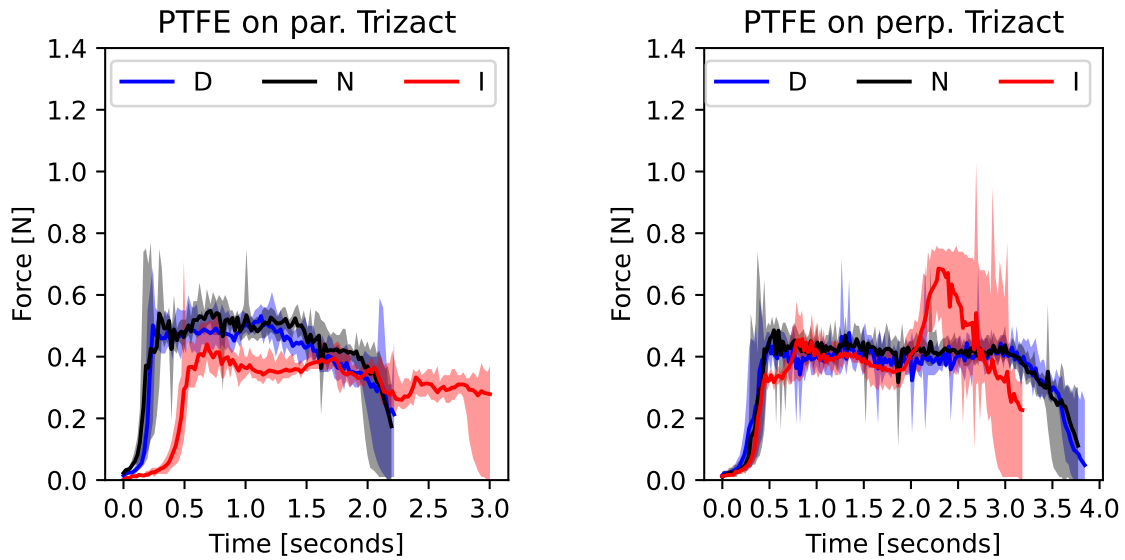
(c) Forces measured when the PTFE sled was pulled across the device in the parallel orientation.

(d) Forces measured when the PTFE sled was pulled across the device in the perpendicular orientation.

Figure A.5: Shear force vs. time when pulling an acrylic-based sled and a PTFE-based sled across a Trizact device. Each plot shows force data from all actuation states for one sled and one device orientation. For each actuation case, the shaded region is the area covered by force curves from 4-6 different trials and the solid line is the average of these curves. The exception is the perpendicular-inflated test for the acrylic sled, for which only 3 trials were conducted. Legend entry D stands for deflated, N stands for neutral, and I stands for inflated.
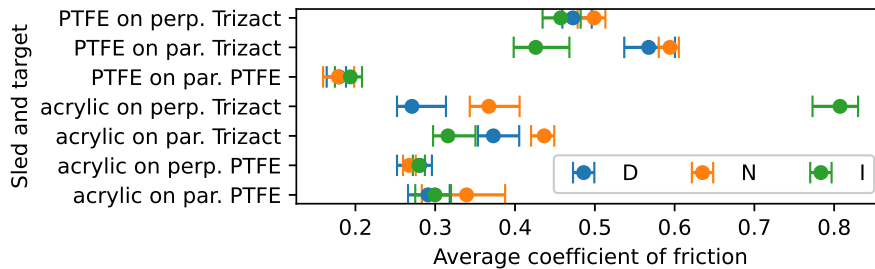
Figure A.6: Comparison of approximate effective coefficient of friction (eCoF) for acrylic- and PTFE-based sleds with Trizact and PTFE adaptive surface devices in different orientations and actuation states. For each sled-device combination, shear force was tested in 3-6 trials per actuation case. The eCoF for each trial was computed by dividing the mean shear force (measured during steady-state sliding) by the sled mass and the gravitational constant. This plot shows the range (bar) and mean value (dot) of the per-trial eCoF values.

For the PTFE device, the average shear forces generally match expectations. The neutral state produces slightly higher forces than the other states in the parallel orientation (Figure A.4a). In the perpendicular orientation (Figure A.4b), the neutral state produces slightly lower forces than the inflated state and similar forces to the deflated state. However, the differences between states and orientations are very minor and not necessarily significant—again, this is possibly because of the limited deflection of this device's contact layer.

For the Trizact device, there is a much clearer difference between the parallel and perpendicular orientations. As expected, the forces for the inflated state are lower than in the neutral state when the device is parallel (Figure A.5a and Figure A.5c) and intermittently higher than in the neutral state when the device is perpendicular (Figure A.5b and Figure A.5d). The forces for the deflated state are lower than or similar to the forces in the neutral state for both orientations. In the parallel orientation, the forces for the deflated state are slightly higher than the forces for the inflated state. With the active regions recessed in the deflated state, the contact area is reduced compared to the neutral state. However, the contact area is likely still greater when the inactive regions of the device are in contact and the active regions are not (in the deflated state) than the reverse (in the inflated state), so it is reasonable that shear forces would be slightly higher in the deflated state.

Effect of Device and Sled Material Choice

Since the normal force on the adaptive surface in this set of experiments comes from the weight of the test sled, the effective coefficient of friction can be computed for each test. For each trial, the force-time data from a 1 second period in which the sled was sliding at a constant velocity were used to compute a representative mean force for the overall trial. This mean force was used to compute the eCoF for each trial. The ranges and averages for each test's eCoF values are shown in Figure A.6.

Based on this eCoF data as well as the force-time curves shown in Figure A.4 and Figure A.5, tests involving the PTFE device have lower levels of friction than tests involving the Trizact device, particularly when the PTFE device is paired with the PTFE sled. This general pattern aligns with expectations, since PTFE is known to be an extremely low-friction material whereas the Trizact sandpaper is a high-friction abrasive. Based on the eCoF data, actuating the Trizact device has a

relatively low impact on its frictional properties when paired with the PTFE sled as compared to the acrylic sled. Force data for the PTFE-Trizact combination show overlap between the eCoF ranges for different actuation states and orientations (excepting the parallel-inflated case, for which the eCoF is much lower). In contrast, the force data for the acrylic-Trizact combination show significant differences between the eCoF ranges for different actuation states and orientations—for instance, the eCoF value for the perpendicular-inflated case is more than double that of the perpendicular-neutral and perpendicular-deflated cases.

Changes Made to Flat Device Testing Process After Baseline Testing

The baseline flat device tests showed some interesting correlations between actuation pressure, device orientation, and shear force for the Trizact device. However, the baseline setup is not representative of forces incurred during robotic gripping, in which compressive forces would be applied to both sides of a target object. In particular, the inflated states, which were intended to increase contact area with a target object, actually decrease contact area with a target object in most cases since the object is free to rise up with the inflated regions when resting freely atop the surface. As such, the test setup used during baseline testing was modified to add an upper constraint that would apply a normal force to the test sled to constrain its vertical position. This enabled adaptive surface testing that better evaluated the potential performance of a candidate surface in a gripping context.

The main flat device testing described in Chapter 6 also used different adaptive surface devices compared to this baseline testing. In baseline testing, the PTFE device showed poor surface adaptation performance and hence was not tested further. Although the Trizact device showed good surface adaptation performance, its abrasive features caused some wear to the bottom of the test sleds, suggesting that it would not be an appropriate general-purpose gripping surface, and so it also was not tested further.

Comparison Between Baseline and Main Flat Device Test Setups

The baseline and main flat device test setups could not be compared directly since they did not use an overlapping set of flat devices. However, there were some relevant data gathered with a prototype upper-constraint setup. These data are not completely reflective of the data gathered with the final upper-constraint setup in the main flat device tests, but they can be used to give a rough idea of the difference in forces measured using an upper constraint.

The forces measured for a neutral parallel PTFE device using this prototype upper-constraint setup are shown with the forces measured for the same device in the baseline test setup in Figure A.7. Two main differences are visible in this force-time data. First, the shear force magnitude is higher in the upper-constraint setup, likely because the normal force on the sled is higher. Second, the force-time curve is less flat for the upper-constraint setup, likely because the contact area with the upper constraint varies slightly depending on the sled's position.

Comparison Between Baseline and Main Flat Device Test Results

There are some interesting differences in the relationship between forces for different actuation states for a parallel device in the main tests as compared to the baseline tests. For the baseline tests, the forces for the inflated state were lower than in the neutral state. In the main tests, the
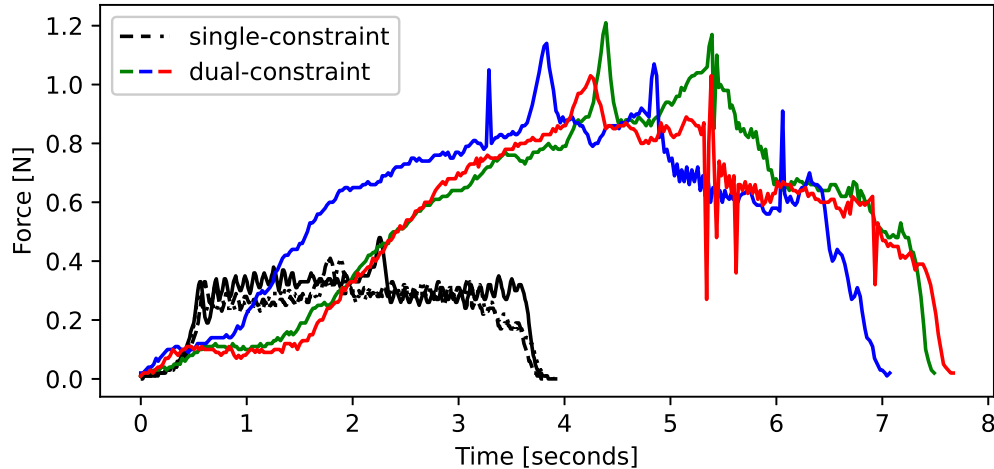
Figure A.7: Force-time data measured using an acrylic-based sled on the PTFE device in the neutral state and parallel orientation with both the single- and dual-constraint setups.

opposite is true: the forces for an inflated device are higher than those for a parallel neutral device. This difference in behaviour is likely attributable to the upper constraint plate's impact on the sled's vertical position. While the sled was free to rest on top of the inflated active regions in the baseline setup (decreasing its contact area with the device) in the main setup the sled must remain at roughly the same height relative to the test platform, meaning that the inflated active regions compress against the sled and likely increase the total contact area.

A.2   Baseline Tests for Fingerpad Devices

Before testing adaptive fingerpad devices as described in Chapter 7, the shear forces applied by the stock gripper fingerpads were tested as a baseline to ensure that force data could be gathered reliably.

A.2.1   Test Procedure

Baseline testing for the gripper fingerpads followed the test process outlined in Section 7.3.

A.2.2   Results and Discussion

The force curves generated during baseline gripper testing are shown in Figure A.8. The force data for objects gripped by the stock fingerpads were reasonably consistent across trials. For instance, the force curves measured when gripping the bare plywood block nearly overlap and show stick-slip oscillations with consistent amplitude. The force curves measured when gripping the PTFE-covered block are slightly farther apart, but two of three curves are almost overlapping, and all curves have the same general shape. Based on this baseline test, the shear force testing procedure appears to be reasonably well controlled, and so the data obtained for adaptive fingerpads should be reliable.
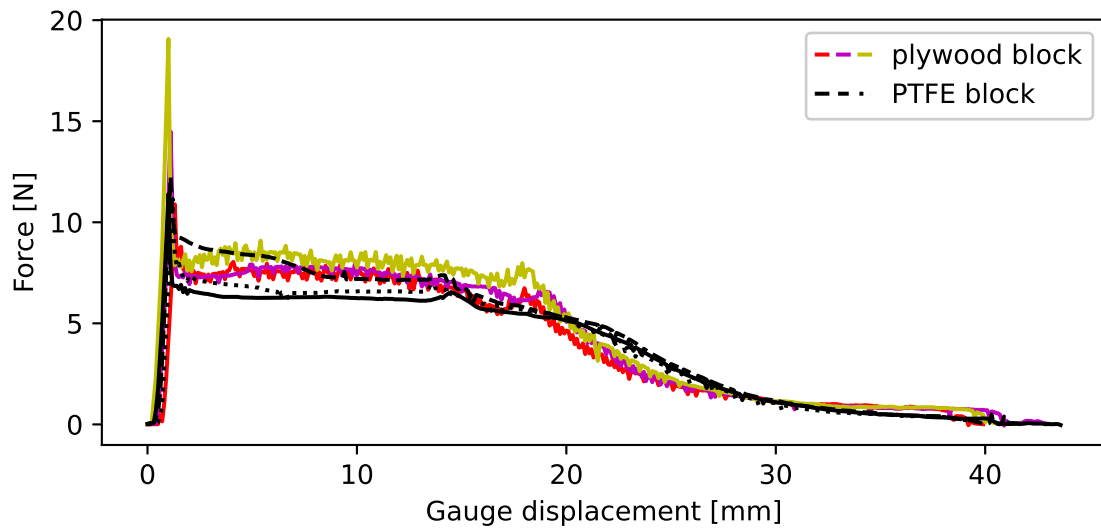
Figure A.8: Shear force on target blocks when gripped using stock gripper fingerpads. Magenta, red, and yellow curves were obtained when gripping the plywood block and black curves were obtained when gripping the PTFE-covered block. The force curves are relatively consistent for each target block material, particularly in the case of the bare plywood block. Notice the slight stick-slip behaviour (indicated by periodic spikes in force data) in the plywood block data.

Appendix B

Pneumatic Control Apparatus

Files associated with the multi-channel pneumatic control apparatus can be found in a dedicated GitHub repository: benchtop_pneumatics_8output.

B.1 Controller Communication

While the pneumatic control apparatus can be run independently, it is more often run as part of an overarching test program. In either case, the apparatus is used by sending command strings to the ATmega2560 microcontroller over serial. These command strings use a three-part format including a letter code that identifies a specific action, an integer ID that identifies a specific component, and a value that identifies the desired state change or setting associated with the action and component. A list of valid commands is provided in Table B.1.

Table B.1: List of serial command codes along with their associated full command format and a description of their function. The value 999 is used as a placeholder to fill empty command parts (e.g., to fill the valve ID for a command that sets *all* valves).

Code	Command Format	Action
SI	<SI, valve ID, state>	Sets state of a single input valve.
SO	<SO, valve ID, state>	Sets state of a single output valve.
AI	<AI, 999, state>	Sets state of all input valves.
AO	<AO, 999, state>	Sets state of all output valves.
GI	<GI, sensor ID, 999>	Returns pressure reading for an input channel.
GO	<GO, sensor ID, 999>	Returns pressure reading for an output channel.
VI	<VI, valve ID, 999>	Returns current state of a single input valve.
VO	<VO, valve ID, 999>	Returns current state of a single output valve.
RS	<RS, pump ID, setpoint>	Sets setpoint for a single input channel pump.
RG	<RG, pump ID, 999>	Returns current setpoint for a single pump.
PS	<PS, pump ID, state>	Sets state of a single pump.
PG	<PG, pump ID, 999>	Returns current state of a single pump.

The ATmega2560 microcontroller continuously runs a main control loop which first checks for and acts on serial inputs (as shown in Figure B.1) and then regulates pressure in the input valves based on the current setpoint (as shown in Figure B.2).
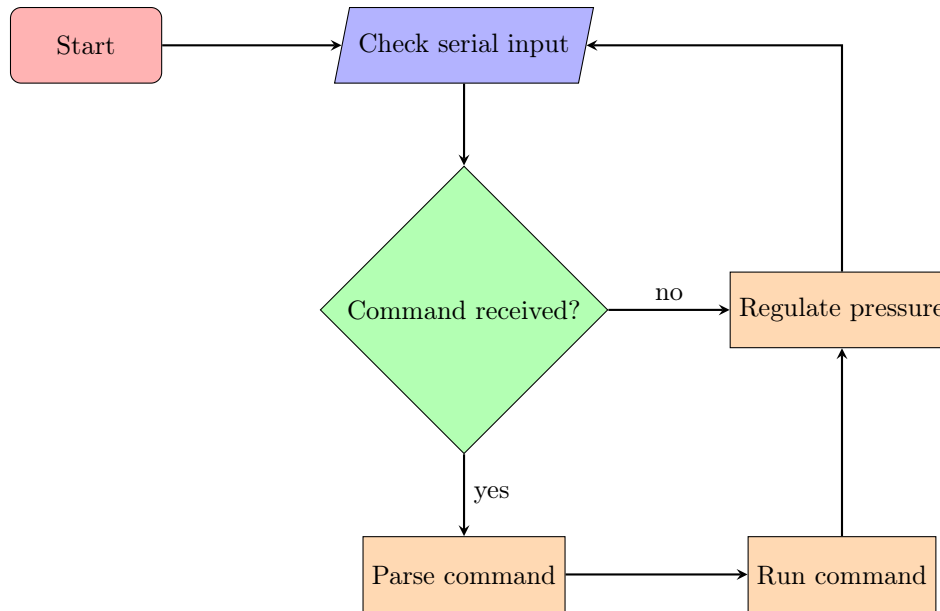
Figure B.1: Flow of main pneumatic control loop.

In experimental work, the pneumatic control apparatus was generally controlled through higher-level testing code that abstracted many of the low-level control operations required for pressure regulation. This testing code provided the user with the ability to simply enter new pressure setpoints as desired, with all other operations being handled by preprogrammed functions.

To run the pneumatic control process without an external test program, the Arduino IDE can be used to send serial commands directly to the device; however, the user must then type the full command in its three part format as shown in Table B.1. A Python wrapper script `python_devices.py` is provided in the GitHub repository to enable command line control of the device without the need to type exact command strings.

B.2   Pneumatic Control Procedures

As previously mentioned in Section 5.1, the pneumatic control system has two core objectives: regulation and switching.

B.2.1   Regulation

On startup, the default setpoints for the positive and negative input channels are both set to 0 kPa (meaning that the pressure in both channels should be about the same as atmospheric pressure). The setpoint for a given channel can be changed via user input by using the `RS` command code shown in Table B.1.

The regulation process (the `pressure_control` function) runs once per iteration of the main loop and turns pumps on or off as needed to change the pressure in the input channels. A pump state change is triggered when its associated input channel reaches a pressure level that differs from its current setpoint by more than a error threshold value (b).

The regulation process uses a simple bang-bang control approach as follows:

1. Get a new pressure reading $P[n]$ from each pressure sensor.

2. For each pressure sensor reading, compute the exponentially weighted moving average[1] (EWMA) with $\alpha = 0.01$:

$$\bar{P}[n] = \alpha P[n] + (1 - \alpha)\bar{P}[n-1]$$

3. For the negative input channel:

   (a) Compute the regulation error as the difference between the current average pressure reading $\bar{P}_N[n]$ and the setpoint pressure S_N:

   $$e_N = \bar{P}_N[n] - S_N$$

   (b) If the error e_N is *greater than* the error threshold b ($e_N > b$) then the negative input channel pump is turned `on` to lower the pressure in the channel.

   (c) If the error e_N is *less than* the *negative* of the error threshold b ($e_N < -b$) then the negative input channel pressure is sufficiently low and the pump is turned `off`.

4. For the positive input channel:

   (a) Compute the regulation error as the difference between the current average pressure reading $\bar{P}_P[n]$ and the setpoint pressure S_P:

   $$e_P = \bar{P}_P[n] - S_P$$

   (b) If the error e_P is *less than* the *negative* of the error threshold b ($e_P < -b$) then the positive input channel pump is turned `on` to raise the pressure in the channel.

   (c) If the error e_P is *greater than* the error threshold b ($e_P > b$) then the positive input channel pressure is sufficiently high and the pump is turned `off`.

The error threshold value b is set to a small positive value (e.g., $b = 0.3$). If this threshold is changed to a *smaller* positive value, then the pumps will run more frequently to regulate pressure within a smaller target range. Similarly, if this threshold is changed to a *larger* positive value, then the pumps will run less frequently. The regulation process is depicted as a flowchart in Figure B.2.

B.2.2   Switching

Unlike pressure regulation, pressure switching is not a default control routine and does not have an associated function on the ATmega2560 microcontroller. Rather, higher-level programs can control pressure switching by calling specific commands in sequence. The control system is programmed this way because (unlike pressure regulation) pressure switching might involve different sequences of actions for different output devices or test procedures. For instance, one test might involve switching only between pressure levels within a current state (e.g., switching from inflated at $+10$ kPa to inflated at $+50$ kPa) whereas another might involve switching between different states (e.g., switching from inflated at $+20$ kPa to deflated at -20 kPa)—these two tests, although both types of pressure switching, would greatly differ in the number and type of control actions involved.

---

[1]This is a type of low-pass single-pole infinite impulse response (IIR) filter.
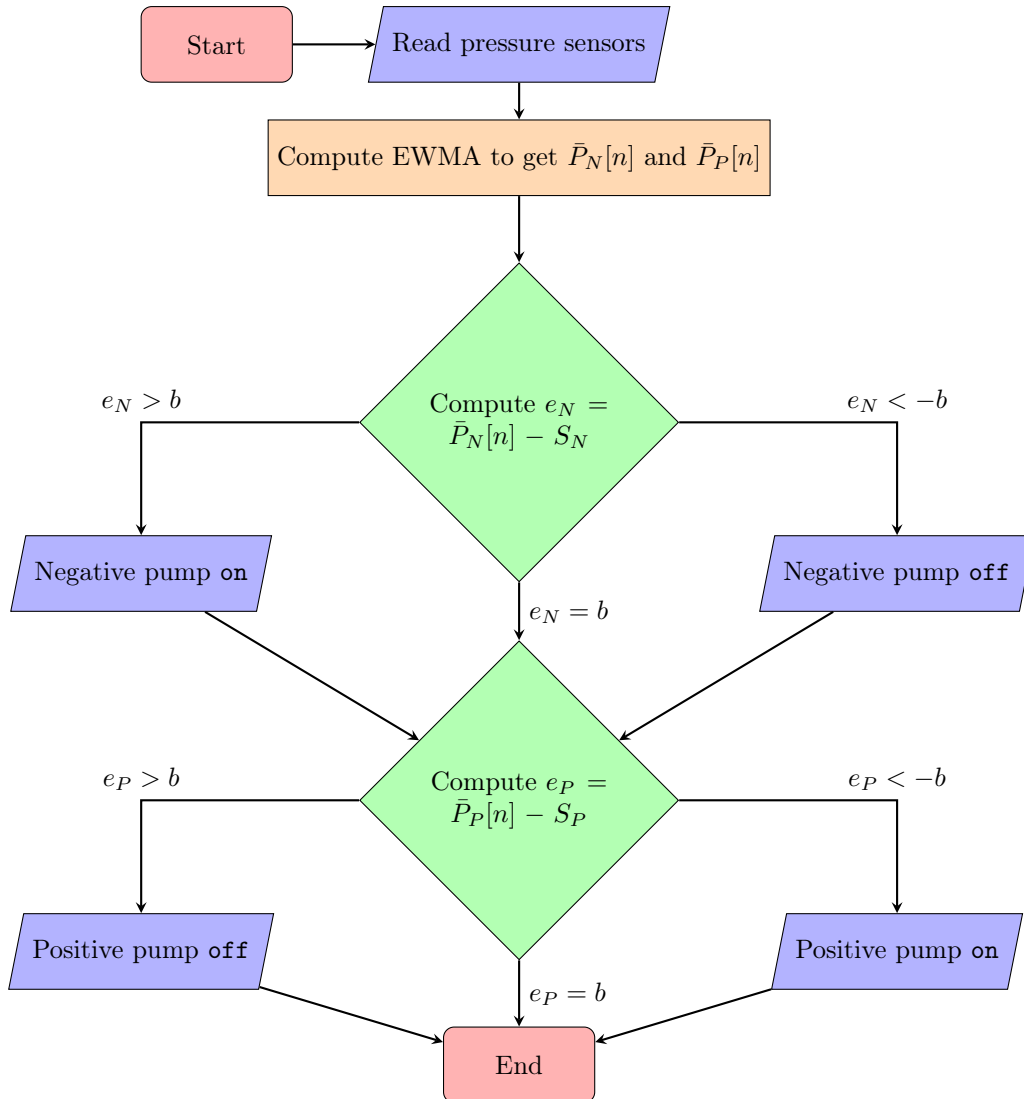
Figure B.2: Flow of pneumatic regulation control loop.

In general, pressure switching involves the following steps:

1. Close all output valves to isolate devices from the switching process.

2. If the desired next state is *neutral*, close all input valves and then reopen the neutral input valve.

3. Otherwise, if the desired next state (deflated or inflated) of the device is *the same as* the current state:

    (a) Change the input channel setpoint to match the desired next pressure.

    (b) Open the valve between the common channel and the current input channel if not already open.

    (c) Wait and run regulation until the input channel pressure (and the common channel pressure) reach the setpoint.

4. Otherwise, if the desired next state (deflated or inflated) *differs from* the current state:

    (a) Change the input channel setpoint to match the desired next pressure.

    (b) Close all input valves.

    (c) Open the neutral input valve to allow the common channel pressure to return to atmospheric pressure levels (avoiding sudden changes between very high and very low pressures).

    (d) Wait with the neutral valve open for a few seconds.

    (e) Close the neutral valve.

    (f) Open the desired input valve.

    (g) Wait and run regulation until the input channel pressure (and the common channel pressure) reach the setpoint.

5. Open the valve between the common channel and the desired output channel(s).

This process is depicted in Figure B.3.
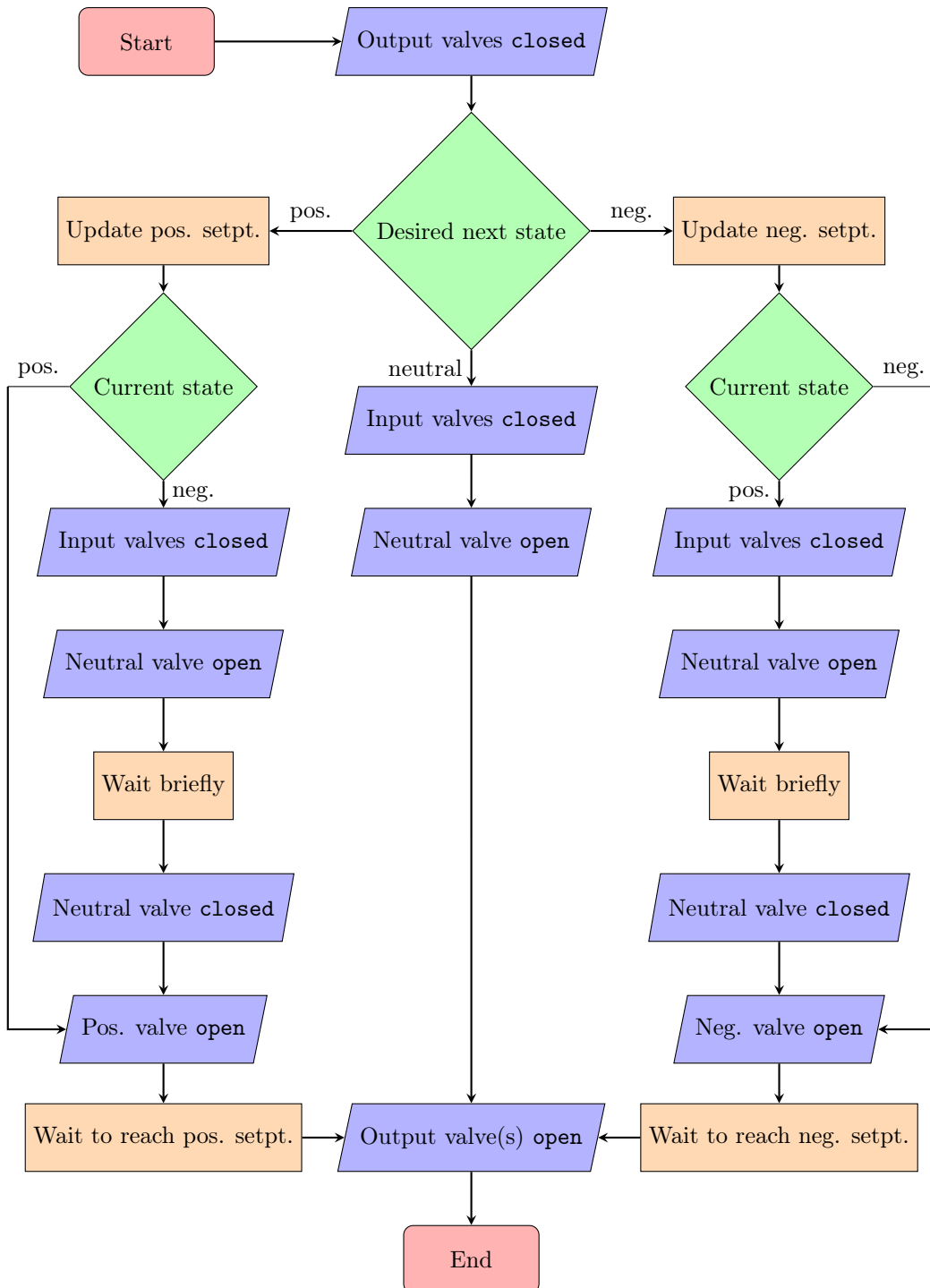
Figure B.3: Flow of pressure switching control in a typical application for this system. "Pos.", "neg.", and "setpt." are abbreviations for "positive", "negative", and "setpoint".

Appendix C

Shear Force Test Apparatus

Files associated with the shear force test apparatus can be found in two dedicated GitHub repositories: benchtop_force_tester_build and benchtop_force_tester_code.

C.1   Data Handling

The process for cleaning force test data (i.e., removing outliers and cropping the start and end of force curves) is shown in Figure C.1.
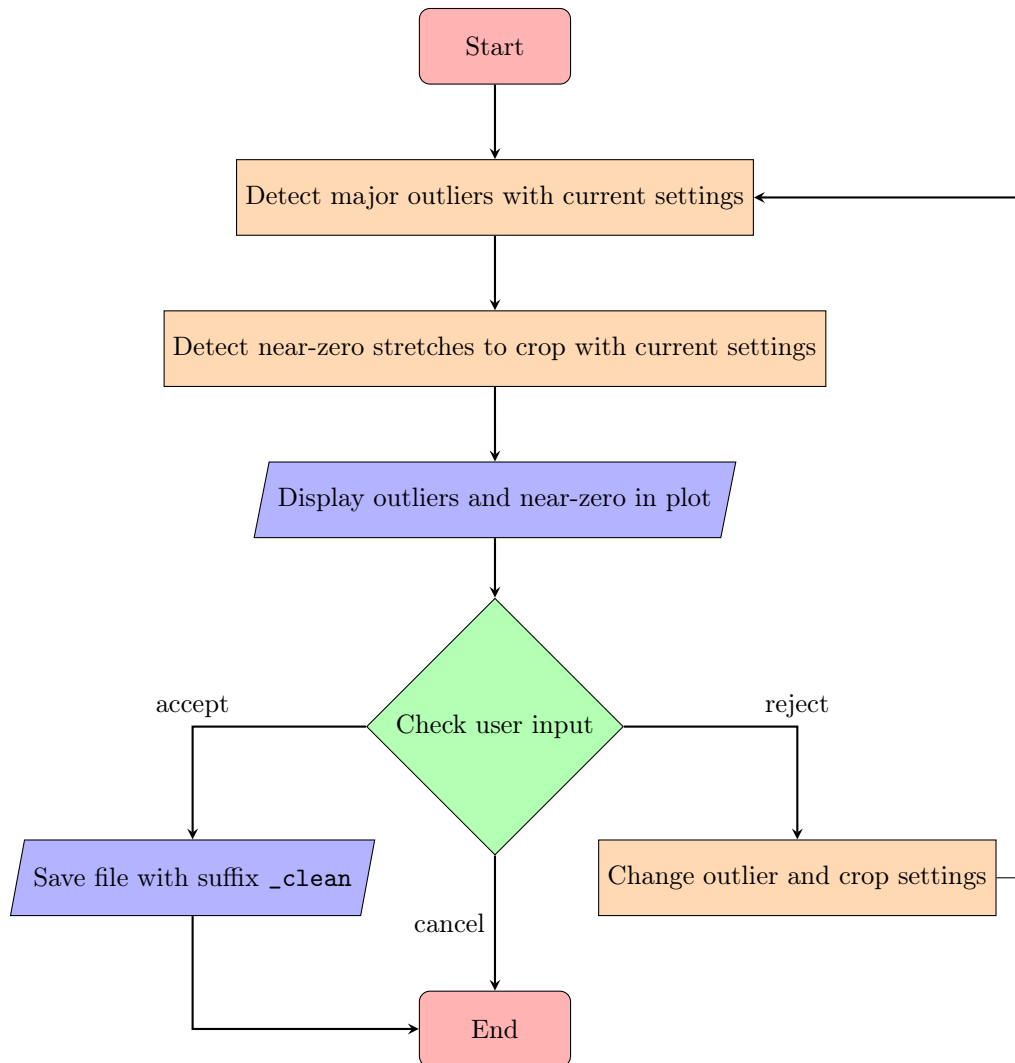
Figure C.1: Flow of data cleaning after force tests.

Bibliography

[1] Y. Hao and Y. Visell, "Beyond Soft Hands: Efficient Grasping With Non-Anthropomorphic Soft Grippers," *Frontiers in Robotics and AI*, vol. 8, 2021. DOI: 10.3389/frobt.2021.632006.

[2] H.-T. Lin, T.-F. Hong, and W.-L. Li, "Grip Performance Affected by Water-Induced Wrinkling of Fingers," *Tribology Letters*, vol. 58, no. 3, p. 38, Jun. 2015. DOI: 10.1007/s11249-015-0515-4.

[3] T. Hao, H. Xiao, J. Wang, X. Wang, S. Liu, and Q. Liu, "Friction Enhancement Through Fingerprint-like Soft Surface Textures in Soft Robotic Grippers for Grasping Abilities," *Tribology Letters*, vol. 72, no. 2, p. 47, Jun. 2024. DOI: 10.1007/s11249-024-01848-2.

[4] D. Prattichizzo and J. C. Trinkle, "Grasping," in *Springer Handbook of Robotics*, B. Siciliano and O. Khatib, Eds., Berlin, Heidelberg: Springer, 2008, pp. 671–700. DOI: 10.1007/978-3-540-30301-5_29.

[5] J. Shintake, V. Cacucciolo, D. Floreano, and H. Shea, "Soft Robotic Grippers," *Advanced Materials*, vol. 30, no. 29, p. 1 707 035, Jul. 2018. DOI: 10.1002/adma.201707035.

[6] M. R. Cutkosky and P. K. Wright, "Friction, Stability and the Design of Robotic Fingers," *The International Journal of Robotics Research*, vol. 5, no. 4, pp. 20–37, Dec. 1986. DOI: 10.1177/027836498600500402.

[7] M. Ciocarlie, C. Lackner, and P. Allen, "Soft Finger Model with Adaptive Contact Geometry for Grasping and Manipulation Tasks," in *Second Joint EuroHaptics Conference and Symposium on Haptic Interfaces for Virtual Environment and Teleoperator Systems (WHC'07)*, Mar. 2007, pp. 219–224. DOI: 10.1109/WHC.2007.103.

[8] Q. Lu and N. Rojas, "On Soft Fingertips for In-Hand Manipulation: Modeling and Implications for Robot Hand Design," *IEEE Robotics and Automation Letters*, vol. 4, no. 3, pp. 2471–2478, Jul. 2019. DOI: 10.1109/LRA.2019.2906544.

[9] K. Mizushima, T. Nishimura, Y. Suzuki, T. Tsuji, and T. Watanabe, "Surface Texture of Deformable Robotic Fingertips for a Stable Grasp Under Both Dry and Wet Conditions," *IEEE Robotics and Automation Letters*, vol. 2, no. 4, pp. 2048–2055, Oct. 2017. DOI: 10.1109/LRA.2017.2717082.

[10] Q. Lu, A. B. Clark, M. Shen, and N. Rojas, "An Origami-Inspired Variable Friction Surface for Increasing the Dexterity of Robotic Grippers," *IEEE Robotics and Automation Letters*, vol. 5, no. 2, pp. 2538–2545, Apr. 2020. DOI: 10.1109/LRA.2020.2972833.

[11] W. Ruotolo, D. Brouwer, and M. R. Cutkosky, "From grasping to manipulation with gecko-inspired adhesives on a multifinger gripper," *Science Robotics*, vol. 6, no. 61, eabi9773, Dec. 2021. DOI: 10.1126/scirobotics.abi9773.

[12] S. Nojiri, K. Mizushima, Y. Suzuki, T. Tsuji, and T. Watanabe, "Development of Contact Area Variable Surface for Manipulation Requiring Sliding," in *2019 2nd IEEE International Conference on Soft Robotics (RoboSoft)*, Apr. 2019, pp. 131–136. DOI: 10.1109/ROBOSOFT.2019.8722754.

[13] T. D. Ta, T. Umedachi, and Y. Kawahara, "Design of Frictional 2D-Anisotropy Surface for Wriggle Locomotion of Printable Soft-Bodied Robots," in *2018 IEEE International Conference on Robotics and Automation (ICRA)*, Brisbane, QLD: IEEE, May 2018, pp. 6779–6785. DOI: 10.1109/ICRA.2018.8463177.

[14] M. R. Cutkosky, "Climbing with adhesion: From bioinspiration to biounderstanding," *Interface Focus*, vol. 5, no. 4, p. 20 150 015, Aug. 2015. DOI: 10.1098/rsfs.2015.0015.

[15] E. Kroner and E. Arzt, "Bio-inspired adhesive surfaces: From principles to applications," in *Smart Materials Series*, P. Fratzl, J. W. Dunlop, and R. Weinkamer, Eds., Cambridge: Royal Society of Chemistry, 2013, pp. 310–321. DOI: 10.1039/9781849737555-00310.

[16] A. Jagota and C.-Y. Hui, "Adhesion, friction, and compliance of bio-mimetic and bio-inspired structured interfaces," *Materials Science and Engineering: R: Reports*, vol. 72, no. 12, pp. 253–292, Dec. 2011. DOI: 10.1016/j.mser.2011.08.001.

[17] D. Rus and M. T. Tolley, "Design, fabrication and control of soft robots.," *Nature*, vol. 521, no. 7553, pp. 467–475, 2015. DOI: 10.1038/nature14543.

[18] V. Babin and C. Gosselin, "Mechanisms for Robotic Grasping and Manipulation," *Annual Review of Control, Robotics, and Autonomous Systems*, vol. 4, no. 1, pp. 573–593, May 2021. DOI: 10.1146/annurev-control-061520-010405.

[19] C. Melchiorri and M. Kaneko, "Robot Hands," in *Springer Handbook of Robotics*, B. Siciliano and O. Khatib, Eds., Berlin, Heidelberg: Springer, 2008, pp. 345–360. DOI: 10.1007/978-3-540-30301-5_16.

[20] B. Zhang, Y. Xie, J. Zhou, K. Wang, and Z. Zhang, "State-of-the-art robotic grippers, grasping and control strategies, as well as their applications in agricultural robots: A review," *Computers and Electronics in Agriculture*, vol. 177, p. 105 694, Oct. 2020. DOI: 10.1016/j.compag.2020.105694.

[21] H. Jiang, Z. Wang, Y. Jin, *et al.*, "Hierarchical control of soft manipulators towards unstructured interactions," *The International Journal of Robotics Research*, vol. 40, no. 1, pp. 411–434, Jan. 2021. DOI: 10.1177/0278364920979367.

[22] E. Mirzaieepoor, M. S. Hassanli, P. Moradi, and M. M. Khoddami, "Mathematical Studying in Control of Grasping," *International Journal of Science and Qualitative Analysis*, vol. 2, no. 1, p. 1, Jul. 2016. DOI: 10.11648/j.ijsqa.20160201.11.

[23] S. Caldera, A. Rassau, and D. Chai, "Review of Deep Learning Methods in Robotic Grasp Detection," *Multimodal Technologies and Interaction*, vol. 2, no. 3, p. 57, Sep. 2018. DOI: 10.3390/mti2030057.

[24] J.-P. Roberge, W. Ruotolo, V. Duchaine, and M. Cutkosky, "Improving Industrial Grippers With Adhesion-Controlled Friction," *IEEE Robotics and Automation Letters*, vol. 3, no. 2, pp. 1041–1048, Apr. 2018. DOI: 10.1109/LRA.2018.2794618.

[25] T. M. Huh, H. Choi, S. Willcox, S. Moon, and M. R. Cutkosky, "Dynamically Reconfigurable Tactile Sensor for Robotic Manipulation," *IEEE Robotics and Automation Letters*, vol. 5, no. 2, pp. 2562–2569, Apr. 2020. DOI: 10.1109/LRA.2020.2972881.

[26] M. Guelker, "Get a Handling on Grippers," Festo Corp., White Paper, 2020, p. 2.

[27] M. Costanzo, G. De Maria, and C. Natale, "Two-Fingered In-Hand Object Handling Based on Force/Tactile Feedback," *IEEE Transactions on Robotics*, vol. 36, no. 1, pp. 157–173, Feb. 2020. DOI: 10.1109/TRO.2019.2944130.

[28] R. Kanegae, Z. Wang, and S. Hirai, "Easily Fabricatable Shell Gripper for Packaging Multiple Cucumbers Simultaneously," in *2020 IEEE International Conference on Real-time Computing and Robotics (RCAR)*, Sep. 2020, pp. 188–192. DOI: 10.1109/RCAR49640.2020.9303297.

[29] L. Zhou, L. Ren, Y. Chen, S. Niu, Z. Han, and L. Ren, "Bio-Inspired Soft Grippers Based on Impactive Gripping," *Advanced Science*, vol. 8, no. 9, p. 2 002 017, 2021. DOI: 10.1002/advs.202002017.

[30] B. Zhang, J. Zhou, Y. Meng, *et al.*, "Comparative study of mechanical damage caused by a two-finger tomato gripper with different robotic grasping patterns for harvesting robots," *Biosystems Engineering*, vol. 171, pp. 245–257, Jul. 2018. DOI: 10.1016/j.biosystemseng.2018.05.003.

[31] C.-M. Chang, L. Gerez, N. Elangovan, A. Zisimatos, and M. Liarokapis, "On Alternative Uses of Structural Compliance for the Development of Adaptive Robot Grippers and Hands," *Frontiers in Neurorobotics*, vol. 13, Nov. 2019. DOI: 10.3389/fnbot.2019.00091.

[32] M. Ciocarlie, F. M. Hicks, R. Holmberg, *et al.*, "The Velo gripper: A versatile single-actuator design for enveloping, parallel and fingertip grasps," *The International Journal of Robotics Research*, vol. 33, no. 5, pp. 753–767, Apr. 2014. DOI: 10.1177/0278364913519148.

[33] A. Milojević, S. Linß, Ž. Ćojbašić, and H. Handroos, "A Novel Simple, Adaptive, and Versatile Soft-Robotic Compliant Two-Finger Gripper With an Inherently Gentle Touch," *Journal of Mechanisms and Robotics*, vol. 13, no. 011015, Nov. 2020. DOI: 10.1115/1.4048752.

[34] C. Laschi, B. Mazzolai, and M. Cianchetti, "Soft robotics: Technologies and systems pushing the boundaries of robot abilities," *Science Robotics*, vol. 1, no. 1, eaah3690, Dec. 2016. DOI: 10.1126/scirobotics.aah3690.

[35] E. W. Hawkes, C. Majidi, and M. T. Tolley, "Hard questions for soft robotics," *Science Robotics*, vol. 6, no. 53, eabg6049, Apr. 2021. DOI: 10.1126/scirobotics.abg6049.

[36] Y. Wang, Y. Wang, R. T. Mushtaq, and Q. Wei, "Advancements in Soft Robotics: A Comprehensive Review on Actuation Methods, Materials, and Applications," *Polymers*, vol. 16, no. 8, p. 1087, Apr. 2024. DOI: 10.3390/polym16081087.

[37] S. Gong, Q. Ding, J. Wu, *et al.*, "Bioinspired Multifunctional Mechanoreception of Soft–Rigid Hybrid Actuator Fingers," *Advanced Intelligent Systems*, vol. 4, no. 5, p. 2 100 242, 2022. DOI: 10.1002/aisy.202100242.

[38] G. M. Whitesides, "Soft Robotics," *Angewandte Chemie International Edition*, vol. 57, no. 16, pp. 4258–4273, 2018. DOI: 10.1002/anie.201800907.

[39] F. Ilievski, A. D. Mazzeo, R. F. Shepherd, X. Chen, and G. M. Whitesides, "Soft Robotics for Chemists," *Angewandte Chemie*, vol. 123, no. 8, pp. 1930–1935, 2011. DOI: 10.1002/ange.201006464.

[40] S. Song, "Soft Robotic Grippers Using Gecko-Inspired Fibrillar Adhesives for Three-Dimensional Surface Grasping," Thesis, Carnegie Mellon University, Jun. 2017. DOI: 10.1184/R1/6723002.v1.

[41] P. Glick, S. A. Suresh, D. Ruffatto, M. Cutkosky, M. T. Tolley, and A. Parness, "A Soft Robotic Gripper With Gecko-Inspired Adhesive," *IEEE Robotics and Automation Letters*, vol. 3, no. 2, pp. 903–910, Apr. 2018. DOI: 10.1109/LRA.2018.2792688.

[42] O. Yasa, Y. Toshimitsu, M. Y. Michelis, *et al.*, "An Overview of Soft Robotics," *Annual Review of Control, Robotics, and Autonomous Systems*, vol. 6, no. 1, pp. 1–29, May 2023. DOI: 10.1146/annurev-control-062322-100607.

[43] L. Y. Lee, O. A. Syadiqeen, C. P. Tan, and S. G. Nurzaman, "Closed-Structure Compliant Gripper With Morphologically Optimized Multi-Material Fingertips for Aerial Grasping," *IEEE Robotics and Automation Letters*, vol. 6, no. 2, pp. 887–894, Apr. 2021. DOI: 10.1109/LRA.2021.3052420.

[44] H. Hauser and A. Hamacher, *Morphological computation: The hidden superpower of soft-bodied robots*, RoboHub. [Online]. Available: https://robohub.org/morphological-computation-the-hidden-superpower-of-soft-bodied-robots/.

[45] J. Guo, J. Leng, and J. Rossiter, "Electroadhesion Technologies for Robotics: A Comprehensive Review," *IEEE Transactions on Robotics*, vol. 36, no. 2, pp. 313–327, Apr. 2020. DOI: 10.1109/TRO.2019.2956869.

[46] Y. Hao, S. Biswas, E. W. Hawkes, *et al.*, "A Multimodal, Enveloping Soft Gripper: Shape Conformation, Bioinspired Adhesion, and Expansion-Driven Suction," *IEEE Transactions on Robotics*, vol. 37, no. 2, pp. 350–362, Apr. 2021. DOI: 10.1109/TRO.2020.3021427.

[47] H. Zeng, N. Pesika, Y. Tian, *et al.*, "Frictional Adhesion of Patterned Surfaces and Implications for Gecko and Biomimetic Systems," *Langmuir*, vol. 25, no. 13, pp. 7486–7495, Jul. 2009. DOI: 10.1021/la900877h.

[48] I. Kao, K. Lynch, and J. W. Burdick, "Contact Modeling and Manipulation," in *Springer Handbook of Robotics*, B. Siciliano and O. Khatib, Eds., Berlin, Heidelberg: Springer, 2008, pp. 647–669. DOI: 10.1007/978-3-540-30301-5_28.

[49] E. Gnecco and E. Meyer, "Stick-slip," in *Elements of Friction Theory and Nanotribology*, 1st ed., Cambridge University Press, Mar. 2015, pp. 140–152. DOI: 10.1017/CBO9780511795039.

[50] T. Baumberger and C. Caroli, "Solid friction from stick–slip down to pinning and aging," *Advances in Physics*, vol. 55, no. 3-4, pp. 279–348, May 2006. DOI: 10.1080/00018730600732186.

[51] M. J. Baum, L. Heepe, and S. N. Gorb, "Friction behavior of a microstructured polymer surface inspired by snake skin," *Beilstein Journal of Nanotechnology*, vol. 5, no. 1, pp. 83–97, Jan. 2014. DOI: 10.3762/bjnano.5.8.

[52] K. Xu, P. Zi, and X. Ding, "Learning from biological attachment devices: Applications of bioinspired reversible adhesive methods in robotics," *Frontiers of Mechanical Engineering*, vol. 17, no. 3, p. 43, Nov. 2022. DOI: 10.1007/s11465-022-0699-x.

[53] E. Arzt, H. Quan, R. M. McMeeking, and R. Hensel, "Functional surface microstructures inspired by nature – From adhesion and wetting principles to sustainable new devices," *Progress in Materials Science*, vol. 120, p. 100 823, Jul. 2021. DOI: 10.1016/j.pmatsci.2021.100823.

[54] P.-C. Lin, S. Vajpayee, A. Jagota, C.-Y. Hui, and S. Yang, "Mechanically tunable dry adhesive from wrinkled elastomers," *Soft Matter*, vol. 4, no. 9, p. 1830, 2008. DOI: 10.1039/b802848f.

[55] K. P. Becker, N. W. Bartlett, M. J. D. Malley, P. M. Kjeer, and R. J. Wood, "Tunable friction through constrained inflation of an elastomeric membrane," in *2017 IEEE International Conference on Robotics and Automation (ICRA)*, May 2017, pp. 4352–4357. DOI: 10.1109/ICRA.2017.7989502.

[56] R. Hensel, K. Moh, and E. Arzt, "Engineering Micropatterned Dry Adhesives: From Contact Theory to Handling Applications," *Advanced Functional Materials*, vol. 28, no. 28, p. 1 800 865, 2018. DOI: 10.1002/adfm.201800865.

[57] "Advanced Contact Mechanics," in *Elements of Friction Theory and Nanotribology*, E. Gnecco and E. Meyer, Eds., Cambridge: Cambridge University Press, 2015, pp. 75–108.

[58] A. B. Croll, N. Hosseini, and M. D. Bartlett, "Switchable Adhesives for Multifunctional Interfaces," *Advanced Materials Technologies*, vol. 4, no. 8, p. 1 900 193, 2019. DOI: 10.1002/admt.201900193.

[59] J. Thiemecke and R. Hensel, "Contact Aging Enhances Adhesion of Micropatterned Silicone Adhesives to Glass Substrates," *Advanced Functional Materials*, vol. 30, no. 50, p. 2 005 826, 2020. DOI: 10.1002/adfm.202005826.

[60] L. Pastewka and M. O. Robbins, "Contact between rough surfaces and a criterion for macroscopic adhesion," *Proceedings of the National Academy of Sciences*, vol. 111, no. 9, pp. 3298–3303, Mar. 2014. DOI: 10.1073/pnas.1320846111.

[61] Y. Song, Z. Dai, Z. Wang, A. Ji, and S. N. Gorb, "The synergy between the insect-inspired claws and adhesive pads increases the attachment ability on various rough surfaces," *Scientific Reports*, vol. 6, no. 1, p. 26 219, May 2016. DOI: 10.1038/srep26219.

[62] W. Federle and D. Labonte, "Dynamic biological adhesion: Mechanisms for controlling attachment during locomotion," *Philosophical Transactions of the Royal Society B: Biological Sciences*, vol. 374, no. 1784, p. 20 190 199, Oct. 2019. DOI: 10.1098/rstb.2019.0199.

[63] W. R. T. Roderick, M. R. Cutkosky, and D. Lentink, "Bird-inspired dynamic grasping and perching in arboreal environments," *Science Robotics*, vol. 6, no. 61, eabj7562, Dec. 2021. DOI: 10.1126/scirobotics.abj7562.

[64] P. Zi, K. Xu, Y. Tian, and X. Ding, "A mechanical adhesive gripper inspired by beetle claw for a rock climbing robot," *Mechanism and Machine Theory*, vol. 181, p. 105 168, Mar. 2023. DOI: 10.1016/j.mechmachtheory.2022.105168.

[65] J. G. Pattrick, D. Labonte, and W. Federle, "Scaling of claw sharpness: Mechanical constraints reduce attachment performance in larger insects," *Journal of Experimental Biology*, vol. 221, no. 24, jeb188391, Dec. 2018. DOI: 10.1242/jeb.188391.

[66] L. M. van den Boogaart, J. K. A. Langowski, and G. J. Amador, "Studying Stickiness: Methods, Trade-Offs, and Perspectives in Measuring Reversible Biological Adhesion and Friction," *Biomimetics*, vol. 7, no. 3, p. 134, Sep. 2022. DOI: `10.3390/biomimetics7030134`.

[67] L. F. Boesel, C. Greiner, E. Arzt, and A. del Campo, "Gecko-Inspired Surfaces: A Path to Strong and Reversible Dry Adhesives," *Advanced Materials*, vol. 22, no. 19, pp. 2125–2137, 2010. DOI: `10.1002/adma.200903200`.

[68] B. N. J. Persson, "On the mechanism of adhesion in biological systems," *The Journal of Chemical Physics*, vol. 118, no. 16, p. 7614, 2003. DOI: `10.1063/1.1562192`.

[69] W. Duan, Z. Yu, W. Cui, Z. Zhang, W. Zhang, and Y. Tian, "Bio-inspired switchable soft adhesion for the boost of adhesive surfaces and robotics applications: A brief review," *Advances in Colloid and Interface Science*, vol. 313, p. 102 862, Mar. 2023. DOI: `10.1016/j.cis.2023.102862`.

[70] H. Fan and J. P. Gong, "Bioinspired Underwater Adhesives," *Advanced Materials*, vol. 33, no. 44, p. 2 102 983, 2021. DOI: `10.1002/adma.202102983`.

[71] Y. Chen, J. Meng, Z. Gu, X. Wan, L. Jiang, and S. Wang, "Bioinspired Multiscale Wet Adhesive Surfaces: Structures and Controlled Adhesion," *Advanced Functional Materials*, vol. 30, no. 5, p. 1 905 287, 2020. DOI: `10.1002/adfm.201905287`.

[72] G.-Z. Yang, J. Bellingham, P. E. Dupont, *et al.*, "The grand challenges of Science Robotics," *Science Robotics*, vol. 3, no. 14, eaar7650, Jan. 2018. DOI: `10.1126/scirobotics.aar7650`.

[73] M. Li, A. Mao, Q. Guan, and E. Saiz, "Nature-inspired adhesive systems," *Chemical Society Reviews*, 2024. DOI: `10.1039/D3CS00764B`.

[74] J. Zhao, N. Xia, and L. Zhang, "A review of bioinspired dry adhesives: From achieving strong adhesion to realizing switchable adhesion," *Bioinspiration & Biomimetics*, vol. 19, no. 5, p. 051 003, Jul. 2024. DOI: `10.1088/1748-3190/ad62cf`.

[75] A. del Campo, C. Greiner, I. Álvarez, and E. Arzt, "Patterned Surfaces with Pillars with Controlled 3D Tip Geometry Mimicking Bioattachment Devices," *Advanced Materials*, vol. 19, no. 15, pp. 1973–1977, 2007. DOI: `10.1002/adma.200602476`.

[76] H. Hu, D. Wang, H. Tian, *et al.*, "Bioinspired Hierarchical Structures for Contact-Sensible Adhesives," *Advanced Functional Materials*, vol. 32, no. 8, p. 2 109 076, 2022. DOI: `10.1002/adfm.202109076`.

[77] J. Ahn, H. Han, J.-H. Ha, *et al.*, "Micro-/Nanohierarchical Structures Physically Engineered on Surfaces: Analysis and Perspective," *Advanced Materials*, vol. 36, no. 2, p. 2 300 871, 2024. DOI: `10.1002/adma.202300871`.

[78] A. P. Malshe, S. Bapat, K. P. Rajurkar, and H. Haitjema, "Bio-inspired textures for functional applications," *CIRP Annals*, vol. 67, no. 2, pp. 627–650, Jan. 2018. DOI: `10.1016/j.cirp.2018.05.001`.

[79] P. H. Niewiarowski, A. Y. Stark, and A. Dhinojwala, "Sticking to the story: Outstanding challenges in gecko-inspired adhesives," *The Journal of Experimental Biology*, vol. 219, no. Pt 7, pp. 912–919, Apr. 2016. DOI: `10.1242/jeb.080085`.

[80] D. Brodoceanu, C. T. Bauer, E. Kroner, E. Arzt, and T. Kraus, "Hierarchical bioinspired adhesive surfaces—a review," *Bioinspiration & Biomimetics*, vol. 11, no. 5, p. 051 001, Aug. 2016. DOI: 10.1088/1748-3190/11/5/051001.

[81] S. H. Lee, H. Yi, C. W. Park, H. E. Jeong, and M. Kwak, "Continuous Tip Widening Technique for Roll-to-Roll Fabrication of Dry Adhesives," *Coatings*, vol. 8, no. 10, p. 349, Oct. 2018. DOI: 10.3390/coatings8100349.

[82] A. Patmonoaji, M. A. Mahardika, M. Nasir, *et al.*, "Stereolithography 3D Printer for Micromodel Fabrications with Comprehensive Accuracy Evaluation by Using Microtomography," *Geosciences*, vol. 12, no. 5, p. 183, May 2022. DOI: 10.3390/geosciences12050183.

[83] J. Ou, C.-Y. Cheng, L. Zhou, G. Dublon, and H. Ishii, "Methods of 3D Printing Micro-pillar Structures on Surfaces," in *Adjunct Proceedings of the 28th Annual ACM Symposium on User Interface Software & Technology*, ser. UIST '15 Adjunct, New York, NY, USA: Association for Computing Machinery, Nov. 2015, pp. 59–60. DOI: 10.1145/2815585.2817812.

[84] H. T. M. Hassani and A. Baji, "Recent Progress on the Use of Stimulus-Responsive Materials for Dry Adhesive Applications," *ACS applied bio materials*, vol. 6, no. 10, pp. 4002–4019, Oct. 2023. DOI: 10.1021/acsabm.3c00504.

[85] P. van Assenbergh, M. Fokker, J. Langowski, J. van Esch, M. Kamperman, and D. Dodou, "Pull-off and friction forces of micropatterned elastomers on soft substrates: The effects of pattern length scale and stiffness," *Beilstein Journal of Nanotechnology*, vol. 10, no. 1, pp. 79–94, Jan. 2019. DOI: 10.3762/bjnano.10.8.

[86] N. Moyle, Z. He, H. Wu, C.-Y. Hui, and A. Jagota, "Indentation versus Rolling: Dependence of Adhesion on Contact Geometry for Biomimetic Structures," *Langmuir*, vol. 34, no. 13, pp. 3827–3837, Apr. 2018. DOI: 10.1021/acs.langmuir.8b00084.

[87] S.-H. Lee, T.-W. Kim, and H.-J. Kim, "Tribological characteristics of a microtextured polymer fabricated via an additive manufacturing process," *Journal of Mechanical Science and Technology*, vol. 36, no. 8, pp. 4161–4170, Aug. 2022. DOI: 10.1007/s12206-022-0734-1.

[88] R. Guarino, G. Costagliola, F. Bosia, and N. M. Pugno, "Evidence of friction reduction in laterally graded materials," *Beilstein Journal of Nanotechnology*, vol. 9, no. 1, pp. 2443–2456, Sep. 2018. DOI: 10.3762/bjnano.9.229.

[89] W. Yuan, Y. Yao, L. Keer, *et al.*, "3D-printed biomimetic surface structures with abnormal friction properties," *Extreme Mechanics Letters*, vol. 26, pp. 46–52, Jan. 2019. DOI: 10.1016/j.eml.2018.12.003.

[90] M. D. Bartlett, A. B. Croll, and A. J. Crosby, "Designing Bio-Inspired Adhesives for Shear Loading: From Simple Structures to Complex Patterns," *Advanced Functional Materials*, vol. 22, no. 23, pp. 4985–4992, 2012. DOI: 10.1002/adfm.201201344.

[91] J. Yu, S. Chary, S. Das, *et al.*, "Gecko-Inspired Dry Adhesive for Robotic Applications," *Advanced Functional Materials*, vol. 21, no. 16, pp. 3010–3018, 2011. DOI: 10.1002/adfm.201100493.

[92] P. Day, E. V. Eason, N. Esparza, D. Christensen, and M. Cutkosky, "Microwedge Machining for the Manufacture of Directional Dry Adhesives," *Journal of Micro and Nano-Manufacturing*, vol. 1, no. 011001, Mar. 2013. DOI: 10.1115/1.4023161.

[93] Y. Cho, H. K. Minsky, Y. Jiang, K. Yin, K. T. Turner, and S. Yang, "Shear Adhesion of Tapered Nanopillar Arrays," *ACS Applied Materials & Interfaces*, vol. 10, no. 13, pp. 11 391–11 397, Apr. 2018. DOI: `10.1021/acsami.8b02303`.

[94] M. P. Murphy, B. Aksak, and M. Sitti, "Adhesion and anisotropic friction enhancements of angled heterogeneous micro-fiber arrays with spherical and spatula tips," *Journal of Adhesion Science and Technology*, vol. 21, no. 12-13, pp. 1281–1296, Jan. 2007. DOI: `10.1163/156856107782328380`.

[95] M. J. Baum, A. E. Kovalev, J. Michels, and S. N. Gorb, "Anisotropic Friction of the Ventral Scales in the Snake Lampropeltis getula californiae," *Tribology Letters*, vol. 54, no. 2, pp. 139–150, May 2014. DOI: `10.1007/s11249-014-0319-y`.

[96] Y. Wang, H. Tian, J. Shao, *et al.*, "Switchable Dry Adhesion with Step-like Micropillars and Controllable Interfacial Contact," *ACS Applied Materials & Interfaces*, vol. 8, no. 15, pp. 10 029–10 037, Apr. 2016. DOI: `10.1021/acsami.6b01434`.

[97] W. B. Khaled and D. Sameoto, "Anisotropic dry adhesive via cap defects," *Bioinspiration & Biomimetics*, vol. 8, no. 4, p. 044 002, Oct. 2013. DOI: `10.1088/1748-3182/8/4/044002`.

[98] C. Zhang, L. Zhao, R. Chen, *et al.*, "Multibioinspired Soft Grasping Actuators with Laser-Induced Multiscale Microstructures," *Advanced Intelligent Systems*, vol. 4, no. 11, p. 2 200 103, 2022. DOI: `10.1002/aisy.202200103`.

[99] J.-K. Kim and M. Varenberg, "Contact splitting in dry adhesion and friction: Reducing the influence of roughness," *Beilstein Journal of Nanotechnology*, vol. 10, no. 1, pp. 1–8, Jan. 2019. DOI: `10.3762/bjnano.10.1`.

[100] Y. Liu, L. Wang, F. Niu, P. Li, Y. Li, and T. Mei, "A Track-type Inverted Climbing Robot with Bio-inspired Spiny Grippers," *Journal of Bionic Engineering*, vol. 17, no. 5, pp. 920–931, Sep. 2020. DOI: `10.1007/s42235-020-0093-5`.

[101] M. Su, Y. Guan, D. Huang, and H. Zhu, "Modeling and analysis of a passively adaptive soft gripper with the bio-inspired compliant mechanism," *Bioinspiration & Biomimetics*, vol. 16, no. 5, p. 055 001, Jul. 2021. DOI: `10.1088/1748-3190/ac07f7`.

[102] A. T. Asbeck, S. Kim, M. R. Cutkosky, W. R. Provancher, and M. Lanzetta, "Scaling Hard Vertical Surfaces with Compliant Microspine Arrays," *The International Journal of Robotics Research*, vol. 25, no. 12, pp. 1165–1179, Dec. 2006. DOI: `10.1177/0278364906072511`.

[103] K. Uno, N. Takada, T. Okawara, *et al.*, "HubRobo: A Lightweight Multi-Limbed Climbing Robot for Exploration in Challenging Terrain," in *2020 IEEE-RAS 20th International Conference on Humanoid Robots (Humanoids)*, Jul. 2021, pp. 209–215. DOI: `10.1109/HUMANOIDS47582.2021.9555799`.

[104] F. Xu, F. Meng, Q. Jiang, and G. Peng, "Grappling claws for a robot to climb rough wall surfaces: Mechanical design, grasping algorithm, and experiments," *Robotics and Autonomous Systems*, vol. 128, p. 103 501, Jun. 2020. DOI: `10.1016/j.robot.2020.103501`.

[105] X. Yang, R. Tan, H. Lu, and Y. Shen, "Starfish Inspired Milli Soft Robot With Omnidirectional Adaptive Locomotion Ability," *IEEE Robotics and Automation Letters*, vol. 6, no. 2, pp. 3325–3332, Apr. 2021. DOI: `10.1109/LRA.2021.3062823`.

[106] C. Kute, M. P. Murphy, Y. Mengüç, and M. Sitti, "Adhesion recovery and passive peeling in a wall climbing robot using adhesives," in *2010 IEEE International Conference on Robotics and Automation*, May 2010, pp. 2797–2802. DOI: 10.1109/ROBOT.2010.5509142.

[107] B. Wang, X. Xiong, J. Duan, Z. Wang, and Z. Dai, "Compliant Detachment of Wall-Climbing Robot Unaffected by Adhesion State," *Applied Sciences*, vol. 11, no. 13, p. 5860, Jan. 2021. DOI: 10.3390/app11135860.

[108] S. Kim, M. Spenko, S. Trujillo, B. Heyneman, D. Santos, and M. Cutkosky, "Smooth Vertical Surface Climbing With Directional Adhesion," *IEEE Transactions on Robotics*, vol. 24, no. 1, pp. 65–74, 2008. DOI: 10.1109/TRO.2007.909786.

[109] Y. Mengüç, S. Y. Yang, S. Kim, J. A. Rogers, and M. Sitti, "Gecko-Inspired Controllable Adhesive Structures Applied to Micromanipulation," *Advanced Functional Materials*, vol. 22, no. 6, pp. 1246–1254, 2012. DOI: 10.1002/adfm.201101783.

[110] E. W. Hawkes, H. Jiang, D. L. Christensen, A. K. Han, and M. R. Cutkosky, "Grasping Without Squeezing: Design and Modeling of Shear-Activated Grippers," *IEEE Transactions on Robotics*, vol. 34, no. 2, pp. 303–316, Apr. 2018. DOI: 10.1109/TRO.2017.2776312.

[111] A. Cauligi, T. G. Chen, S. A. Suresh, *et al.*, "Design and development of a gecko-adhesive gripper for the Astrobee free-flying robot," p. 8, 2020.

[112] S. Nagahama, A. Nakao, and S. Sugano, "Development of a Conveyor-Type Object Release Mechanism for a Parallel Gripper with a Mushroom-Shaped Gecko-Inspired Surface," in *2022 IEEE/RSJ International Conference on Intelligent Robots and Systems (IROS)*, Oct. 2022, pp. 5787–5793. DOI: 10.1109/IROS47612.2022.9981232.

[113] S. K. Sharma and H. S. Grewal, "Tribological Behavior of Bioinspired Surfaces," *Biomimetics*, vol. 8, no. 1, p. 62, Mar. 2023. DOI: 10.3390/biomimetics8010062.

[114] H. Marvi, J. P. Cook, J. L. Streator, and D. L. Hu, "Snakes move their scales to increase friction," *Biotribology*, vol. 5, pp. 52–60, Mar. 2016. DOI: 10.1016/j.biotri.2015.11.001.

[115] H. T. Tramsen, L. Heepe, J. Homchanthanakul, F. Wörgötter, S. N. Gorb, and P. Manoonpong, "Getting grip in changing environments: The effect of friction anisotropy inversion on robot locomotion," *Applied Physics A*, vol. 127, no. 5, p. 389, Apr. 2021. DOI: 10.1007/s00339-021-04443-7.

[116] P. Manoonpong, D. Petersen, A. Kovalev, *et al.*, "Enhanced Locomotion Efficiency of a Bio-inspired Walking Robot using Contact Surfaces with Frictional Anisotropy," *Scientific Reports*, vol. 6, no. 1, p. 39 455, Dec. 2016. DOI: 10.1038/srep39455.

[117] N. Asawalertsak, S. N. Gorb, A. Kovalev, J. Jørgensen, and P. Manoonpong, "Exploiting Friction Anisotropy for Soft Robot Locomotion," in *Robotics in Natural Settings*, J. M. Cascalho, M. O. Tokhi, M. F. Silva, A. Mendes, K. Goher, and M. Funk, Eds., Cham: Springer International Publishing, 2023, pp. 75–79. DOI: 10.1007/978-3-031-15226-9_10.

[118] H. Chitikena, A. Mohammadi, F. Sanfilippo, and M. Poursina, "Anisotropic Friction Skin for Holonomic Snake Robot Mobility*," in *2024 IEEE International Conference on Advanced Robotics and Its Social Impacts (ARSO)*, May 2024, pp. 222–227. DOI: 10.1109/ARSO60199.2024.10557914.

[119] Q. Ze, S. Wu, J. Nishikawa, *et al.*, "Soft robotic origami crawler," *Science Advances*, vol. 8, no. 13, eabm7834, Mar. 2022. DOI: 10.1126/sciadv.abm7834.

[120] D. Mei, X. Yu, G. Tang, *et al.*, "A Soft Crawling Robot with Multi-Modal Locomotion Inspired by the Movement Mechanism of Snake Scales," *IEEE Robotics and Automation Letters*, vol. 9, no. 9, pp. 7589–7596, Sep. 2024. DOI: 10.1109/LRA.2024.3426371.

[121] A. Rafsanjani, Y. Zhang, B. Liu, S. M. Rubinstein, and K. Bertoldi, "Kirigami skins make a simple soft actuator crawl," *Science Robotics*, vol. 3, no. 15, eaar7555, Feb. 2018. DOI: 10.1126/scirobotics.aar7555.

[122] C. Branyan, R. L. Hatton, and Y. Mengüç, "Snake-Inspired Kirigami Skin for Lateral Undulation of a Soft Snake Robot," *IEEE Robotics and Automation Letters*, vol. 5, no. 2, pp. 1728–1733, Apr. 2020. DOI: 10.1109/LRA.2020.2969949.

[123] B. Seyidoğlu and A. Rafsanjani, "A textile origami snake robot for rectilinear locomotion," *Device*, vol. 2, no. 2, 2024. DOI: 10.1016/j.device.2023.100226.

[124] H. Liu, H. Yuan, G. Dong, *et al.*, "Tunable Friction Properties of Periodic Wrinkled BaTiO3 Membranes," *Advanced Materials Interfaces*, vol. 9, no. 13, p. 2 102 316, 2022. DOI: 10.1002/admi.202102316.

[125] K. Suzuki, Y. Hirai, and T. Ohzono, "Oscillating Friction on Shape-Tunable Wrinkles," *ACS Applied Materials & Interfaces*, vol. 6, no. 13, pp. 10 121–10 131, Jul. 2014. DOI: 10.1021/am5010738.

[126] K. Suzuki, Y. Hirai, M. Shimomura, and T. Ohzono, "Tunable Friction Through Microwrinkle Formation on a Reinforced Rubber Surface," *Tribology Letters*, vol. 60, no. 2, p. 24, Nov. 2015. DOI: 10.1007/s11249-015-0600-8.

[127] T. Ohzono and K. Teraoka, "A two-step method for fabricating large-area textile-embedded elastomers for tunable friction," *Royal Society Open Science*, vol. 5, no. 10, p. 181 169, Oct. 2018. DOI: 10.1098/rsos.181169.

[128] A. J. Spiers, B. Calli, and A. M. Dollar, "Variable-Friction Finger Surfaces to Enable Within-Hand Manipulation via Gripping and Sliding," *IEEE Robotics and Automation Letters*, vol. 3, no. 4, pp. 4116–4123, Oct. 2018. DOI: 10.1109/LRA.2018.2856398.

[129] J. Li, W. Chang, and Q. Li, "Soft robot with a novel variable friction design actuated by SMA and electromagnet," *Smart Materials and Structures*, vol. 27, no. 11, p. 115 020, Oct. 2018. DOI: 10.1088/1361-665X/aae412.

[130] N. Chavan-Dafle, K. Lee, and A. Rodriguez, "Pneumatic shape-shifting fingers to reorient and grasp," in *2018 IEEE 14th International Conference on Automation Science and Engineering (CASE)*, Aug. 2018, pp. 988–993. DOI: 10.1109/COASE.2018.8560472.

[131] H. X. Trinh, V. A. Ho, and K. Shibuya, "Theoretical Foundation for Design of Friction-Tunable Soft Finger With Wrinkle's Morphology," *IEEE Robotics and Automation Letters*, vol. 4, no. 4, pp. 4027–4034, Oct. 2019. DOI: 10.1109/LRA.2019.2926960.

[132] A. Luo, S. S. Pande, and K. T. Turner, "Versatile Adhesion-Based Gripping via an Unstructured Variable Stiffness Membrane," *Soft Robotics*, Jul. 2022. DOI: 10.1089/soro.2021.0065.

[133] R. Coulson, C. J. Stabile, K. T. Turner, and C. Majidi, "Versatile Soft Robot Gripper Enabled by Stiffness and Adhesion Tuning via Thermoplastic Composite," *Soft Robotics*, Jan. 2021. DOI: 10.1089/soro.2020.0088.

[134] Y.-F. Zhang, N. Zhang, H. Hingorani, *et al.*, "Fast-Response, Stiffness-Tunable Soft Actuator by Hybrid Multimaterial 3D Printing," *Advanced Functional Materials*, vol. 29, no. 15, p. 1 806 698, 2019. DOI: 10.1002/adfm.201806698.

[135] L. Li, F. Xie, T. Wang, *et al.*, "Stiffness-Tunable Soft Gripper with Soft-Rigid Hybrid Actuation for Versatile Manipulations," *Soft Robotics*, vol. 9, no. 6, pp. 1108–1119, Dec. 2022. DOI: 10.1089/soro.2021.0025.

[136] Y. Yang, Y. Chen, Y. Li, M. Z. Q. Chen, and Y. Wei, "Bioinspired Robotic Fingers Based on Pneumatic Actuator and 3D Printing of Smart Material," *Soft Robotics*, vol. 4, no. 2, pp. 147–162, Jun. 2017. DOI: 10.1089/soro.2016.0034.

[137] T. Hou, X. Yang, Y. Aiyama, *et al.*, "Design and experiment of a universal two-fingered hand with soft fingertips based on jamming effect," *Mechanism and Machine Theory*, vol. 133, pp. 706–719, Mar. 2019. DOI: 10.1016/j.mechmachtheory.2018.12.013.

[138] J.-Y. Lee, Y.-S. Seo, C. Park, *et al.*, "Shape-Adaptive Universal Soft Parallel Gripper for Delicate Grasping Using a Stiffness-Variable Composite Structure," *IEEE Transactions on Industrial Electronics*, vol. 68, no. 12, pp. 12 441–12 451, Dec. 2021. DOI: 10.1109/TIE.2020.3044811.

[139] W. M. A. Jayawardana, T. Elder, T. Twohig, and A. B. Croll, "Switchable origami adhesives," *Soft Matter*, vol. 20, no. 18, pp. 3814–3822, 2024. DOI: 10.1039/D4SM00082J.

[140] S. P. Murali Babu, R. Das, B. Mazzolai, and A. Rafsanjani, "Programmable inflatable origami," in *2023 IEEE International Conference on Soft Robotics (RoboSoft)*, Apr. 2023, pp. 1–6. DOI: 10.1109/RoboSoft55895.2023.10122007.

[141] R. Deimel and A. Kugi, "An Inflatable Eversible Finger Pad for Variable-Stiffness Grasping with Parallel-Jaw Grippers," in *2023 IEEE/RSJ International Conference on Intelligent Robots and Systems (IROS)*, Oct. 2023, pp. 4533–4539. DOI: 10.1109/IROS55552.2023.10341676.

[142] A. Carlson, S. Wang, P. Elvikis, P. M. Ferreira, Y. Huang, and J. A. Rogers, "Active, Programmable Elastomeric Surfaces with Tunable Adhesion for Deterministic Assembly by Transfer Printing," *Advanced Functional Materials*, vol. 22, no. 21, pp. 4476–4484, 2012. DOI: 10.1002/adfm.201201023.

[143] V. Subramaniam, S. Jain, J. Agarwal, and P. Valdivia y Alvarado, "Design and characterization of a hybrid soft gripper with active palm pose control," *The International Journal of Robotics Research*, vol. 39, no. 14, pp. 1668–1685, Dec. 2020. DOI: 10.1177/0278364920918918.

[144] M. Keely, Y. Kim, S. A. Mehta, *et al.*, *Combining and Decoupling Rigid and Soft Grippers to Enhance Robotic Manipulation*, Apr. 2024. DOI: 10.48550/arXiv.2404.13755. arXiv: 2404.13755 [cs].

[145] H. Choi and M. Koç, "Design and feasibility tests of a flexible gripper based on inflatable rubber pockets," *International Journal of Machine Tools and Manufacture*, vol. 46, no. 12, pp. 1350–1361, Oct. 2006. DOI: 10.1016/j.ijmachtools.2005.10.009.

[146] M. D. Swift, C. B. Haverkamp, C. J. Stabile, *et al.*, "Active Membranes on Rigidity Tunable Foundations for Programmable, Rapidly Switchable Adhesion," *Advanced Materials Technologies*, vol. 5, no. 11, p. 2 000 676, 2020. DOI: 10.1002/admt.202000676.

[147] J. M. Krahn, F. Fabbro, and C. Menon, "A Soft-Touch Gripper for Grasping Delicate Objects," *IEEE/ASME Transactions on Mechatronics*, vol. 22, no. 3, pp. 1276–1286, Jun. 2017. DOI: 10.1109/TMECH.2017.2663322.

[148] H. X. Trinh, H.-H. Nguyen, T.-D. Pham, and C. A. My, "A novel rigid-soft gripper for safe and reliable object handling," *Journal of the Brazilian Society of Mechanical Sciences and Engineering*, vol. 46, no. 4, p. 176, Mar. 2024. DOI: 10.1007/s40430-024-04757-6.

[149] N. Kuppuswamy, A. Alspach, A. Uttamchandani, S. Creasey, T. Ikeda, and R. Tedrake, "Soft-bubble grippers for robust and perceptive manipulation," in *2020 IEEE/RSJ International Conference on Intelligent Robots and Systems (IROS)*, Oct. 2020, pp. 9917–9924. DOI: 10.1109/IROS45743.2020.9341534.

[150] M. Pozzi, L. Franco, Z. Iqbal, M. Malvezzi, D. Prattichizzo, and G. Salvietti, "Soft Pneumatic Pads Enable New Sensing and Actuation Capabilities in Soft-Rigid Grippers," in *2024 IEEE 7th International Conference on Soft Robotics (RoboSoft)*, Apr. 2024, pp. 485–491. DOI: 10.1109/RoboSoft60065.2024.10522022.

[151] L. He, Q. Lu, S.-A. Abad, N. Rojas, and T. Nanayakkara, "Soft Fingertips With Tactile Sensing and Active Deformation for Robust Grasping of Delicate Objects," *IEEE Robotics and Automation Letters*, vol. 5, no. 2, pp. 2714–2721, Apr. 2020. DOI: 10.1109/LRA.2020.2972851.

[152] C. Gaudeni, M. Pozzi, Z. Iqbal, M. Malvezzi, and D. Prattichizzo, "Grasping With the Soft-Pad, a Soft Sensorized Surface for Exploiting Environmental Constraints With Rigid Grippers," *IEEE Robotics and Automation Letters*, vol. 5, no. 3, pp. 3884–3891, Jul. 2020. DOI: 10.1109/LRA.2020.2983675.

[153] Y. Wang, X. Yang, Y. Chen, *et al.*, "A biorobotic adhesive disc for underwater hitchhiking inspired by the remora suckerfish," *Science Robotics*, vol. 2, no. 10, eaan8072, Sep. 2017. DOI: 10.1126/scirobotics.aan8072.

[154] E. W. Hawkes, D. L. Christensen, A. K. Han, H. Jiang, and M. R. Cutkosky, "Grasping without squeezing: Shear adhesion gripper with fibrillar thin film," in *2015 IEEE International Conference on Robotics and Automation (ICRA)*, May 2015, pp. 2305–2312. DOI: 10.1109/ICRA.2015.7139505.

[155] E. W. Hawkes, H. Jiang, and M. R. Cutkosky, "Three-dimensional dynamic surface grasping with dry adhesion," *The International Journal of Robotics Research*, vol. 35, no. 8, pp. 943–958, Jul. 2016. DOI: 10.1177/0278364915584645.

[156] J. Xu, L. Xu, J. Liu, X. Li, and X. Wu, "Survey on Bioinspired Adhesive Methods and Design and Implementation of A Multi-Mode Biomimetic Wall-Climbing Robot," in *2018 IEEE/ASME International Conference on Advanced Intelligent Mechatronics (AIM)*, Jul. 2018, pp. 688–693. DOI: 10.1109/AIM.2018.8452318.

[157] V. Alizadehyazdi, M. Bonthron, and M. Spenko, "An Electrostatic/Gecko-Inspired Adhesives Soft Robotic Gripper," *IEEE Robotics and Automation Letters*, vol. 5, no. 3, pp. 4679–4686, Jul. 2020. DOI: 10.1109/LRA.2020.3003773.

[158] S. Li, H. Tian, J. Shao, H. Liu, D. Wang, and W. Zhang, "Switchable Adhesion for Nonflat Surfaces Mimicking Geckos' Adhesive Structures and Toe Muscles," *ACS Applied Materials & Interfaces*, vol. 12, no. 35, pp. 39 745–39 755, Sep. 2020. DOI: 10.1021/acsami.0c08686.

[159] T. Sun, W. Chen, J. Li, *et al.*, "A versatile and high-load soft gripper enabled by vacuum-assisted bio-inspired interfacial adhesion," *Smart Materials and Structures*, vol. 33, no. 1, p. 015 034, Dec. 2023. DOI: 10.1088/1361-665X/ad1427.

[160] S. Song, C. Majidi, and M. Sitti, "GeckoGripper: A soft, inflatable robotic gripper using gecko-inspired elastomer micro-fiber adhesives," in *2014 IEEE/RSJ International Conference on Intelligent Robots and Systems*, Sep. 2014, pp. 4624–4629. DOI: 10.1109/IROS.2014.6943218.

[161] G. Chen, J. Wu, Z. Zhang, B. Zhang, Z. Chu, and J. Cui, "A Soft Robotic Gripper With a Belt Loop Actuated Adhesion Design for Gentle Handling of Fragile Object," *IEEE Robotics and Automation Letters*, vol. 9, no. 8, pp. 6784–6791, Aug. 2024. DOI: 10.1109/LRA.2024.3414248.

[162] D. Hirano, N. Tanishima, A. Bylard, and T. G. Chen, "Underactuated Gecko Adhesive Gripper for Simple and Versatile Grasp," in *2020 IEEE International Conference on Robotics and Automation (ICRA)*, May 2020, pp. 8964–8969. DOI: 10.1109/ICRA40945.2020.9196806.

[163] R. Chen, L. Wu, Y. Sun, J.-Q. Chen, and J.-L. Guo, "Variable stiffness soft pneumatic grippers augmented with active vacuum adhesion," *Smart Materials and Structures*, vol. 29, no. 10, p. 105 028, Sep. 2020. DOI: 10.1088/1361-665X/aba848.

[164] S. Song and M. Sitti, "Soft Grippers Using Micro-fibrillar Adhesives for Transfer Printing," *Advanced Materials*, vol. 26, no. 28, pp. 4901–4906, 2014. DOI: 10.1002/adma.201400630.

[165] S. Song, D.-M. Drotlef, C. Majidi, and M. Sitti, "Controllable load sharing for soft adhesive interfaces on three-dimensional surfaces," *Proceedings of the National Academy of Sciences*, vol. 114, no. 22, E4344–E4353, May 2017. DOI: 10.1073/pnas.1620344114.

[166] S. Song, D.-M. Drotlef, J. Paik, C. Majidi, and M. Sitti, "Mechanics of a pressure-controlled adhesive membrane for soft robotic gripping on curved surfaces," *Extreme Mechanics Letters*, vol. 30, p. 100 485, Jul. 2019. DOI: 10.1016/j.eml.2019.100485.

[167] Y. Shao, H. Dou, P. Tao, *et al.*, "Precise Controlling of Friction and Adhesion on Reprogrammable Shape Memory Micropillars," *ACS Applied Materials & Interfaces*, vol. 14, no. 15, pp. 17 995–18 003, Apr. 2022. DOI: 10.1021/acsami.2c03589.

[168] H. Tian, X. Li, J. Shao, *et al.*, "Gecko-Effect Inspired Soft Gripper with High and Switchable Adhesion for Rough Surfaces," *Advanced Materials Interfaces*, vol. 6, no. 18, p. 1 900 875, 2019. DOI: 10.1002/admi.201900875.

[169] A. del Campo, C. Greiner, and E. Arzt, "Contact Shape Controls Adhesion of Bioinspired Fibrillar Surfaces," *Langmuir*, vol. 23, no. 20, pp. 10 235–10 243, Sep. 2007. DOI: 10.1021/la7010502.

[170]   C. Linghu, Z. Du, Y. Sun, W. Chen, and K. J. Hsia, "On shear adhesion of adhesive fibrils," *Extreme Mechanics Letters*, vol. 64, p. 102 092, Nov. 2023. DOI: `10.1016/j.eml.2023.102092`.

[171]   T. Calais and P. V. y Alvarado, "Advanced functional materials for soft robotics: Tuning physicochemical properties beyond rigidity control," *Multifunctional Materials*, vol. 2, no. 4, p. 042 001, Dec. 2019. DOI: `10.1088/2399-7532/ab4f9d`.

[172]   F. Ahmed, M. Waqas, B. Jawed, *et al.*, "Decade of bio-inspired soft robots: A review," *Smart Materials and Structures*, vol. 31, no. 7, p. 073 002, Jun. 2022. DOI: `10.1088/1361-665X/ac6e15`.

[173]   J. Liu, Y. Yao, S. Chen, X. Li, and Z. Zhang, "A strong and reversible adhesive fibrillar surface based on an advanced composite with high strength and strong adhesion," *International Journal of Smart and Nano Materials*, vol. 14, no. 1, pp. 103–121, Jan. 2023. DOI: `10.1080/19475411.2023.2168783`.

[174]   K. Laqua, "Dynamic Microtopography Arrays for Hybrid and Adaptive Switchable Adhesion," Thesis, University of Toronto, Toronto, Nov. 2019.

[175]   *Robotiq 2F-85 & 2F-140 for e-Series Universal Robots*, Instruction Manual, 2018.